

**Radiation
from Directional Seismic Sources
in Laterally Stratified Media
with Application to Arctic Ice Cracking Noise**

by

Jea Soo Kim

B. S. Naval Architecture, Seoul National University (1981)
M. S. Oceanographic Engineering, University of Florida (1984)

**Submitted in Partial Fulfillment
of the Requirements for the Degree of**

Doctor of Philosophy

at the

**Massachusetts Institute of Technology
May 1989**

© Jea Soo Kim, 1989

The author hereby grants to MIT permission to reproduce and
to distribute copies of this thesis in whole or in part.

Signature of Author _____
Department of Ocean Engineering
May 6, 1989

Certified by _____
Professor Henrik Schmidt
Thesis Supervisor

Accepted by _____
Professor A. Douglas Carmichael
Chairman, Departmental Graduate Committee



ARCHIVES

| Report Documentation Page | | Form Approved OMB No. 0704-0188 |
|---|----------------------|---|
| Public reporting burden for the collection of information is estimated to average 1 hour per response, including the time for reviewing instructions, searching existing data sources, gathering and maintaining the data needed, and completing and reviewing the collection of information. Send comments regarding this burden estimate or any other aspect of this collection of information, including suggestions for reducing this burden, to Washington Headquarters Services, Directorate for Information Operations and Reports, 1215 Jefferson Davis Highway, Suite 1204, Arlington VA 22202-4302. Respondents should be aware that notwithstanding any other provision of law, no person shall be subject to a penalty for failing to comply with a collection of information if it does not display a currently valid OMB control number. | | |
| 1. REPORT DATE MAY 1989 | 2. REPORT TYPE | 3. DATES COVERED 00-00-1989 to 00-00-1989 |
| 4. TITLE AND SUBTITLE Radiation from Directional Seismic Sources in Laterally Stratified Media with Application to Arctic Ice Cracking Noise | | 5a. CONTRACT NUMBER |
| | | 5b. GRANT NUMBER |
| | | 5c. PROGRAM ELEMENT NUMBER |
| 6. AUTHOR(S) | 5d. PROJECT NUMBER | |
| | 5e. TASK NUMBER | |
| | 5f. WORK UNIT NUMBER | |
| 7. PERFORMING ORGANIZATION NAME(S) AND ADDRESS(ES) Massachusetts Institute of Technology, 77 Massachusetts Avenue, Cambridge, MA, 02139 | | 8. PERFORMING ORGANIZATION REPORT NUMBER |
| 9. SPONSORING/MONITORING AGENCY NAME(S) AND ADDRESS(ES) | | 10. SPONSOR/MONITOR'S ACRONYM(S) |
| | | 11. SPONSOR/MONITOR'S REPORT NUMBER(S) |
| 12. DISTRIBUTION/AVAILABILITY STATEMENT Approved for public release; distribution unlimited | | |
| 13. SUPPLEMENTARY NOTES | | |
| 14. ABSTRACT <p>The formation of cracks in elastic media such as sea ice generates elastic waves in a radiation pattern being dependent on the actual fracture process and the stratification of the medium. In the case of horizontal stratification this phenomenon can be idealized and mathematically modeled describing the directionality of the acoustic emission produced by compact cracks in such an environment. The thrust of the present research has been to develop an analytical and numerical model of the elastic wave field in range independent elastic environments for various seismic source mechanisms. The source types being considered are explosive sources, point forces, shear cracks, and tensile cracks. First, the compact source representations with fault surface in an arbitrary direction will be derived, and incorporated in a numerical model for propagation in stratified elastic media to yield the basic Green's function solution. This solution is then applied to derive the seismo-acoustic field produced by more complete cracking mechanisms, like non-compact and moving cracks. Finally, the effect of anisotropy on the acoustic emission, e.g. in sea ice and periodically fine layered sediments, will be considered. The developed model is applied to the ice cracking noise radiation in the central Arctic environment, and the characteristics of the field produced by different source and environmental parameters are discussed. The developed model can be applied to the source inversion problem, i.e. the characterization of the cracking mechanism from its acoustic emission with the purpose of obtaining a better understanding of the general ambient noise in the central Arctic. Another expected application is the development of remote sensing techniques suitable for the study of mechanical properties of ice.</p> | | |
| 15. SUBJECT TERMS | | |

| | | | | | |
|----------------------------------|------------------------------------|-------------------------------------|--|--------------------------------------|------------------------------------|
| 16. SECURITY CLASSIFICATION OF: | | | 17. LIMITATION OF ABSTRACT Same as Report (SAR) | 18. NUMBER OF PAGES 171 | 19a. NAME OF RESPONSIBLE PERSON |
| a. REPORT unclassified | b. ABSTRACT unclassified | c. THIS PAGE unclassified | | | |

Radiation from Directional Seismic Sources
in Laterally Stratified Media
with Application to Arctic Ice Cracking Noise

Jea Soo Kim

Submitted in partial fulfillment of the requirements
for the degree of Doctor of Philosophy
May 22, 1989

Abstract

The formation of cracks in elastic media such as sea ice generates elastic waves in a radiation pattern being dependent on the actual fracture process and the stratification of the medium. In the case of horizontal stratification, this phenomenon can be idealized and mathematically modeled describing the directionality of the acoustic emission produced by compact cracks in such an environment.

The thrust of the present research has been to develop an analytical and numerical model of the elastic wave field in range independent elastic environments for various seismic source mechanisms. The source types being considered are explosive sources, point forces, shear cracks, and tensile cracks. First, the compact source representations with fault surface in an arbitrary direction will be derived, and incorporated in a numerical model for propagation in stratified elastic media to yield the basic Green's function solution. This solution is then applied to derive the seismo-acoustic field produced by more complete cracking mechanisms, like non-compact and moving cracks. Finally, the effect of anisotropy on the acoustic emission, e.g. in sea ice and periodically fine layered sediments, will be considered.

The developed model is applied to the ice cracking noise radiation in the central Arctic environment, and the characteristics of the field produced by different source and environmental parameters are discussed. The developed model can be applied to the source inversion problem, i.e. the characterization of the cracking mechanism from its acoustic emission with the purpose of obtaining a better understanding of the general ambient noise in the central Arctic. Another expected application is the development of remote sensing techniques suitable for the study of mechanical properties of ice.

Thesis supervisor : Dr. Henrik Schmidt
Associate Professor of Ocean Engineering

Acknowledgements

This thesis reflects five years of hard work including many nightshifts. I appreciate the opportunity to work among the dynamic individuals of the Arctic acoustics group as well as my other colleagues in Rm. 5-007. There are so many people who made available their time and effort to make this thesis possible, I can not mention all of them. Among them, I would like to thank Prof. Ira Dyer for introducing me to Arctic acoustics, Ms. Marilyn Staruch for her friendly help in administration, Dr. Greg Duckworth for sharing his valuable time with me on the class project during the spring 1987 which eventually led to this thesis topic, Eddie Sheer for teaching me and maintaining the computer facilities at Woods Hole Oceanographic Institute while I was working on FRAM II and IV data, Dr. Mitchele for giving a seminar about source representation at ERL which made my research get going during the fall 1987, Dr. Mandal at ERL for the discussions about the transversely isotropic medium, Dr. Glattetre for providing the prototype 3-D code, Dr. Tango for the comments on my thesis proposal and for providing key references, and the people with whom I shared the same office, the up-and-down times and many discussions about the research, life, and the world we are living in, Dr. Chil Sung Park, Dr. Tae Young Chung, Hee Chun Song, Chifang Chen, Nick Makris, Hyun Yup Lee, Woojae Seong, and Dr. Peter Dahl.

My most sincere and special thanks go to my advisor, Professor Henrik Schmidt, for his encouragement and support on the topic, for his insightful advice on the problems, for all the program packages he provided, and for his insights into the real world. It has been a most enjoyable and rewarding experience to have opportunity to work with him. After all, this work would not have been possible without him.

Also, I would like to extend my thanks to the thesis committee members, Professors Ira Dyer, Nafi Toksoz, and Dale Karr, for their valuable suggestions and encouragement.

My dearest love and joy go to my mother and father, whose abundant love made me free and responsible and, simply, guided me through the years abroad, and to my wife, Gyung Lim, who is also my best friend and has been there always when I needed it the most, and who has almost never complained about those nightshifts and after-midnight snacks that she made for years, and, finally, to my angel daughter, Hyun Min, who kept me busier and, certainly, happier than ever during the last year of my graduate school days at M.I.T., but gave my family the deepest sorrow on earth finding the eternal peace in God's land, so is this thesis dedicated to my family.

Sponsored in part by :

Office of Naval Research
800 N. Quincy St.
Arlington, VA 22217
Contract No : N00014-77-C-0266
Technical Monitor : Mr. R. Obrochta

Contents

| | |
|--|-----------|
| Abstract | 2 |
| Acknowledgements | 3 |
| Glossary | 13 |
| 1 Introduction | 17 |
| 1.1 Background | 17 |
| 1.2 Objective | 21 |
| 1.3 Approach | 21 |
| 1.4 Overview of the Thesis | 25 |
| 2 Representation of Seismic Sources | 29 |
| 2.1 Representation Theorem and Body Force Equivalents for Seismic Sources | 30 |
| 2.2 Radiation from Body Forces in a Homogeneous Isotropic Medium | 33 |
| 2.3 Single Couples | 38 |
| 2.4 Double Couples | 42 |
| 2.5 Summary of Equivalent Body Forces for Seismic Sources | 43 |
| 3 Field Representation in a Laterally Stratified Medium | 46 |

| | | |
|----------|--|-----------|
| 3.1 | Homogeneous Solution to Wave Equation in Cylindrical Coordinates | 47 |
| 3.2 | Seismic Source Green's Function in Cylindrical Coordinates . . . | 50 |
| 3.2.1 | strike-slip | 51 |
| 3.2.2 | Dip-slip | 54 |
| 3.2.3 | Tensile Crack | 55 |
| 3.3 | Global Matrix Approach | 58 |
| 3.4 | Field Representation in a Laterally Stratified medium | 63 |
| 3.4.1 | Complete Solution | 63 |
| 3.4.2 | Numerical Consideration | 64 |
| 3.5 | Numerical Examples | 65 |
| 4 | Radiation from Propagating Cracks | 73 |
| 4.1 | Analytic Solution to a Canonical Crack Radiation Problem . . . | 74 |
| 4.2 | Numerical Model for Propagating Cracks in an Stratified Medium | 77 |
| 4.3 | Numerical Examples | 82 |
| 5 | Transversely Isotropic Medium | 87 |
| 5.1 | Equation of Motion | 88 |
| 5.2 | Stress-Strain Relation | 88 |
| 5.3 | Equivalent Transversely Isotropic Elastic Constants for Periodically Fine Layered Medium | 89 |
| 5.4 | Decoupled Equations for SH and P-SV Waves | 90 |
| 5.5 | Formulation of Boundary Conditions Compatible with Global Matrix Method | 94 |
| 5.6 | Numerical Examples | 95 |
| 6 | Application to Ice Crack Radiation in the Central Arctic Envi- | |

| | |
|---|------------|
| Environment | 103 |
| 6.1 The Central Arctic Environment | 106 |
| 6.2 Radiation from Three Modes of Compact Cracks | 107 |
| 6.3 Most probable source types and corresponding source strength . | 118 |
| 6.4 Radiation from Propagating Cracks | 124 |
| 6.5 Parametric Study of Crack Radiation | 130 |
| 6.6 Anisotropy of Ice | 132 |
| 6.7 Proposed Crack Radiation Experiment | 138 |
| 6.7.1 Laboratory Experiment | 140 |
| 6.7.2 Field Experiment | 146 |
| 6.8 Conclusion | 147 |
| 7 Conclusions | 150 |
| 7.1 Summary | 150 |
| 7.2 Discussions and Suggestions for Future Studies | 152 |
| Appendix | 155 |
| A Potentials, Displacements and Stresses of Various Sources with an Arbitrary Direction in Cylindrical Coordinates | 155 |
| A.1 Point Force in an Arbitrary Direction | 156 |
| A.2 Dip-slip | 159 |
| A.3 Strike-slip | 161 |
| A.4 Tensile Crack | 163 |
| A.5 Explosive Source | 166 |
| Bibliography | 168 |

List of Figures

| | | |
|-----|---|----|
| 1.1 | The research issue applied to the seismic study of ice and the ambient noise generation mechanism due to ice cracking noise . . | 20 |
| 1.2 | The solution technique | 22 |
| 1.3 | Overview of the thesis | 25 |
| 2.1 | Fault motion. | 31 |
| 2.2 | Body force equivalents for derivatives of Green's function. | 32 |
| 2.3 | Decomposition of single couple into two body forces. | 38 |
| 2.4 | Nine single couples. | 40 |
| 2.5 | Decomposition of a double couple into two single couples. | 42 |
| 2.6 | Strike-slip with dip angle $\delta = 0$ (a) fault surface and slip motion (b) equivalent body forces. | 43 |
| 2.7 | Dip-slip with dip angle $\delta = 0$ (a) fault surface and slip motion (b) equivalent body forces. | 44 |
| 2.8 | Tensile crack with dip angle $\delta = 0$ (a) fault surface and motion (b) equivalent body forces. | 45 |
| 3.1 | Fault motion with dip angle δ , (a) Tensile crack, (b) dip-slip, (c) strike-slip. | 51 |
| 3.2 | Definition of fault orientation parameters. | 55 |

| | | |
|------|--|----|
| 3.3 | Single couples used to represent tensile crack with dip angle δ and strike angle $\phi_s = 0$, (a) (1,1) with $M_0 = 1$, (b) (2,2) with $M_0 = 1$, (c) (3,3) with $M_0 = \frac{\lambda+2\mu}{\lambda}$ | 56 |
| 3.4 | Mapping between local and global systems of equations (after Schmidt and Jensen, 1985). | 62 |
| 3.5 | Source function (a) time series, (b) spectral shape. | 66 |
| 3.6 | Sketch of coordinate system with source and receiver positions. . | 67 |
| 3.7 | Radiation pattern of tensile crack with dip angle $\delta = 90^\circ$ for single frequency $f = 100$ Hz in a homogeneous elastic medium. | 69 |
| 3.8 | Seismogram for tensile crack with dip angle $\delta = 90^\circ$, receivers at $z = 0$ m, $r = 300$ m at every 30° in a homogeneous elastic medium. | 69 |
| 3.9 | Radiation pattern of dip-slip with dip angle $\delta = 90^\circ$ for single frequency $f = 100$ Hz in a homogeneous elastic medium. | 70 |
| 3.10 | Seismogram for dip-slip with dip angle $\delta = 90^\circ$, receivers at $z = 0$ m, $r = 300$ m at every 30° in a homogeneous elastic medium. . | 70 |
| 3.11 | Radiation pattern of strike-slip with dip angle $\delta = 90^\circ$ for single frequency $f = 100$ Hz in a homogeneous elastic medium. | 71 |
| 3.12 | Seismogram for strike-slip with dip angle $\delta = 90^\circ$, receivers at $z = 0$ m, $r = 300$ m at every 30° in a homogeneous elastic medium. . | 71 |
| 4.1 | Discretized source distributed over the line crack and coordinate system. | 74 |
| 4.2 | Fourier transform pair, (a) rectangular source strength distribution function along the crack, (b) Fourier transform of $\frac{1}{2}\text{rect}(r_a)$. . | 78 |
| 4.3 | Sketch of moving crack. | 79 |
| 4.4 | Receiver-source position transformation (a) source distribution over fault surface, (b) reduced numerical model. | 80 |

| | | |
|-----|--|-----|
| 4.5 | Two dimensional crack surface and source distribution. | 82 |
| 4.6 | Radiation pattern for an array of explosive sources for a single frequency $f = 100$ Hz in a homogeneous acoustic medium. | 84 |
| 4.7 | Seismogram for an array of explosive sources with receivers at $z = 60$ m, $r = 300$ m at every 30° in a homogeneous acoustic medium. | 84 |
| 4.8 | Radiation pattern for an array of explosive sources for a single frequency $f = 100$ Hz in a homogeneous elastic medium. | 85 |
| 4.9 | Seismogram for an array of explosive sources with receivers at $z = 60$ m, $r = 300$ m at every 30° in a homogeneous elastic medium. | 85 |
| 5.1 | Sketch of a periodically finely layered medium. | 89 |
| 5.2 | A single force as a source. | 95 |
| 5.3 | Slowness surface of P (solid line), SV (dotted line), and SH (dashed line) waves for case 1. | 96 |
| 5.4 | Synthetic time series in an unbounded homogeneous, transversely isotropic medium, (a) vertical velocity, (b) x-direction velocity. . | 98 |
| 5.5 | Synthetic time series in an unbounded homogeneous isotropic medium, (a) vertical velocity, (b) x-direction velocity. | 99 |
| 5.6 | Modulus of the inverse Hankel transform integrand for the isotropic medium (solid line), and transversely isotropic medium (broken line), (a) and (b) show the vertical displacements for Fourier or- ders zero-th and $\cos \theta$ orders, respectively, (c) and (d) for the x-direction velocity, and (e) and (f) for the y-direction velocity. . | 100 |
| 6.1 | Geometry for central Arctic environment. | 105 |
| 6.2 | Seismic moment (a) source function, (b) spectrum | 108 |

| | | |
|------|--|-----|
| 6.3 | (a) Radiation pattern for $f = 100$ Hz, (b) synthetic time series for tensile crack with dip angle $\delta = 90^\circ$ in the central Arctic environment. | 109 |
| 6.4 | Synthetic time series for tensile crack with dip angle $\delta = 90^\circ$, receivers at $z = 5$ m, $r = 300$ m at every 30° in a central Arctic environment. | 110 |
| 6.5 | Dispersion curve for the first antisymmetric mode of the ice plate, the upper line is for the group velocity and the lower line for the phase speed. | 111 |
| 6.6 | Modulus of inverse Hankel transform integrand for Fourier (a) zeroth and (b) second, $\cos 2\theta$, orders and frequency $f = 100$ Hz, at $z = 5$ m and $z = 60$ m. | 112 |
| 6.7 | (a) Radiation pattern for $f = 100$ Hz, (b) synthetic time series for dip-slip with dip angle $\delta = 90^\circ$ in a central Arctic environment | 113 |
| 6.8 | (a) Radiation pattern for $f = 100$ Hz, (b) synthetic time series for strike-slip with dip angle $\delta = 90^\circ$ in a central Arctic environment. | 114 |
| 6.9 | Transfer functions for each mode of cracks | 117 |
| 6.10 | Ratio of the amplitude of the radiation from the longitudinal wave in the ice plate(A_l) to the amplitude of acoustic mode(A_a), i.e. $\frac{A_l}{A_a}$, for three types of cracks with varying dip angle | 119 |
| 6.11 | Synthetic time series in the horizontal direction 30° at range $r = 300$ m and at depth of $z = 60$ m for dip-slip with dip angle $\delta = 0^\circ$ | 121 |
| 6.12 | Field pressure variation depending on the horizontal angle and range for 200 Hz., source strength is $4\pi N \cdot m$ | 122 |
| 6.13 | Synthetic time series in the horizontal direction 30° at range $r = 300$ m and at depth of $z = 60$ m for tensile crack with dip angle $\delta = 0^\circ$ | 123 |

| | |
|--|-----|
| 6.14 (a) Radiation pattern at $f = 200$ Hz, (b) synthetic time series for dip-slip with dip angle $\delta = 90^\circ$ in a central Arctic environment. . | 126 |
| 6.15 (a) Synthetic time series, and (b) spectrum, in the horizontal angle $\theta = 30^\circ$ for moving dip-slip | 127 |
| 6.16 (a) Synthetic time series, and (b) spectrum, in the horizontal angle $\theta = 90^\circ$ for moving dip-slip | 128 |
| 6.17 (a) Synthetic time series, and (b) spectrum, in the horizontal angle $\theta = 150^\circ$ for moving dip-slip | 129 |
| 6.18 Synthetic time series in an isotropic ice plate in the central Arctic environment, (a) vertical displacement, (b) x-direction displacement. | 134 |
| 6.19 Synthetic time series in a transversely isotropic ice plate in the central Arctic environment, (a) vertical displacement, (b) x-direction displacement. | 135 |
| 6.20 Slowness surface of P (solid line), SV (dotted line), and SH (dashed line) waves. | 136 |
| 6.21 Modulus of Hankel transform integrand for isotropic medium (solid line), and transversely isotropic medium (dotted line), (a) and (b) show the vertical displacements for Fourier orders zero-th and $\cos 2\theta$ orders, respectively, (c) and (d) for the x -direction velocity, and (e) and (f) for the y -direction velocity. | 137 |
| 6.22 Top view of an array of accelerometers in the ice. | 144 |
| 6.23 (a) Top view of hydrophone array and (b) Cross section along x -axis. | 145 |
| 6.24 Tri-axial accelerometers placed along the prescribed crack surface to measure the displacement along and across the crack surface. | 146 |

Glossary

$*$: convolution.

$\langle \rangle$: thickness-weighted average.

A : fault area.

\mathbf{A}_n : coefficient matrix for n -th layer.

\mathbf{B}_n^m : unknown variables matrix for n -th layer and m -th Fourier order.

C_{ij} : elastic constants for a transversely isotropic medium (refer to Eq 5.2).

c_P : phase speed of the P wave in the transversely isotropic medium.

c_{SV} : phase speed of the SV wave in the transversely isotropic medium.

c_{SH} : phase speed of the SH wave in the transversely isotropic medium.

c_c : compressional wave velocity.

c_s : shear wave velocity.

$\mathbf{e}_1, \mathbf{e}_2, \mathbf{e}_3$: unit vectors in (x_1, x_2, x_3) rectangular coordinate system.

$\mathbf{e}_x, \mathbf{e}_y, \mathbf{e}_z$: unit vectors in (x, y, z) rectangular coordinate system.

$\mathbf{F}^m(r, z)$: field parameter matrix for particular solution used for boundary condition when $z = 0, z_n$, and for solution at receiver depth when $z = z_r$.

$\mathbf{F}^m(s, z)$: Hankel transform of $\mathbf{F}^m(r, z)$.

\mathbf{f} : vector body force used in the representation theorem.

f_n : force in n -direction.

\mathbf{F} : vector body force as a source term in the equation of motion, $\mathbf{F} = F_x \mathbf{e}_x + F_y \mathbf{e}_y + F_z \mathbf{e}_z$.

F, G, H : displacement potential in Cartesian coordinates.

G_{np} : Green's function for displacement in n -direction due to a body force in p -direction.

$G_{np,q}$: derivative of G_{np} in q -direction.

$\mathbf{H}^m(r, z)$: Inverse Hankel transform of $\mathbf{H}^m(s, z)$, and m -th order field parameter matrix.

$\mathbf{H}^m(s, z)$: Hankel integrand modulus matrix for a set of field parameters used for boundary condition. $z = 0, z_n$ for boundary condition, and $z = z_r$ for solution at receiver depth.

h : compressional wavenumber.

k : shear wavenumber.

L, M, N : force potentials in Cartesian coordinates.

$M_0(t)$: seismic moment source function.

\mathbf{n} : normal vector (usually to the crack surface).

n_i : component of normal vector in i -direction.

$\mathbf{R}^m(r, z)$: Inverse Hankel transform of $\mathbf{R}^m(s, z)$, i.e. m -th order field parameter matrix due to source.

$\mathbf{R}^m(s, z)$: matrix for a set of field parameters used for boundary condition due to source. $z = 0, z_n$ for boundary condition, and $z = z_r$ for particular solution at receiver depth.

\mathbf{r} : position vector.

r : range in rectangular coordinates.

s : horizontal wave number.

$[\mathbf{T}]$: traction discontinuity.

$[\mathbf{u}]$: vector displacement discontinuity on the crack surface.

\mathbf{u} : vector displacement.

u : r -direction displacement at horizontal interface in cylindrical coordinates.

u_n : displacement in n direction.

$\bar{u}(t)$: average slip in fault source.

v : θ -direction displacement at horizontal interface in cylindrical coordinates.

w : z -direction displacement at horizontal interface in cylindrical coordinates.

$X_0(t)$: force source function.

X, Y, Z : three components of force \mathbf{F} as a source term in the equation of motion.

z_n : thickness of n -th layer.

z_r : receiver depth.

z_s : source depth.

α : vertical wavenumber parameters for compressional waves.

β : vertical wavenumber parameters for shear waves.

δ : dip angle, refer to Fig 3.2.

ϵ : strain.

λ : rake angle, refer to Fig 3.2.

λ, μ : Lamé constants.

ρ : density.

σ : stress.

σ_{zz} : normal stress in z -direction at horizontal interface.

σ_{rz} : shear stress in r -direction at horizontal interface.

$\sigma_{\theta z}$: shear stress in θ -direction at horizontal interface.

ϕ_s : strike angle, refer to Fig 3.2.

$\phi, \psi_1, \psi_2, \psi_3$: potentials in (x_1, x_2, x_3) Cartesian coordinate system used in Chapter 2 and 3, of which relation to displacement are defined in Eq 2.28.

$\phi, \psi_x, \psi_y, \psi_z$: potentials in (x, y, z) Cartesian coordinate system used in Chapter 3.

$\phi, \psi_r, \psi_\theta, \psi_z$: potentials in (r, θ, z) cylindrical coordinate system, of which relation to displacement are defined in Eq 3.11.

ϕ, Λ, ψ : scalar potentials in (r, θ, z) cylindrical coordinate system, of which relation to displacement are defined in Eq 3.1.

ζ : parameter defined as

$$\zeta = \text{sign}(z - z_s) = \begin{cases} 1 & , \quad z - z_s \geq 0 \\ -1 & , \quad z - z_s < 0. \end{cases}$$

Chapter 1

Introduction

1.1 Background

The formation of cracks in elastic media such as sea ice generates elastic waves in a radiation pattern being dependent on the actual fracture process and the stratification of the medium. In the case of horizontal stratification, this phenomenon can be idealized and mathematically modeled as a compact but directional source radiating in a stratified elastic medium, yielding the Green's function solution. Further, the basic Green's function solution, by integration in time and space, can lead to synthesis of the wave field produced by more complete cracking mechanisms, like non-compact and moving cracks. A mathematical description of this phenomenon is essential to the inverse problem of determining the source mechanism from experimental data, provided that the medium is known on the basis of geological and geophysical data, and the forward problem of predicting, with accumulated data, the field parameters of interest at specific positions. Further, such a mathematical model is instrumental to the medium inverse problem of seismo-acoustic exploration, where, for various types of excitation, the observed data are used to probe the geological

composition. On this background, the research described in this thesis is centered around the development of an efficient mathematical/numerical model of the acoustic emission produced by compact and propagating cracks in realistic stratified environments.

To illustrate how the present research can be instrumental in understanding an important physical problem, an application to the central Arctic ambient will be discussed. The main source of the central Arctic ambient noise has been known to originate from the elastic motion of the ice plate caused by environmental stresses. When the stress in the ice plate is locally greater than the strength of the ice causing fracture, the stored energy is released in the form of elastic motion of the ice. This energy radiates into the water, forming ambient noise when the events are aggregated. In order to better understand the Arctic ambient noise generating mechanism, two levels of approaches are being pursued [9]. One approach is to correlate the spectral and temporal characteristics of ambient noise to gross environmental parameters such as thermal changes, current and wind stresses [33]. The other level of approach is to look into the individual ice cracking events, and treat them as a noise generating source element, which forms the average ambient noise when aggregated. The latter approach is based on the assumption that the central Arctic ambient noise is dominated by the radiation due to mechanical processes in the ice cover, so that the ambient noise is aggregate of individual events [9] [34]. Therefore, it is obvious that the models that represent probable source mechanisms of a single event need to be developed to understand the central Arctic ambient noise characteristics as an aggregate of events.

In order to be more specific about the issue investigated in this study in relation to the central Arctic ambient noise, the processes involved in the generation of the Arctic ambient noise can be categorized as (Fig 1.2)

- (1) Development of environmental stresses,
- (2) Ice plate motion induced by fracture due to the environmental stresses,
- (3) Radiation from the ice plate into water.

The first phenomenon has been extensively studied and associated with the observed ambient noise [31] [33]. The radiation mechanism from the ice plate to water is also studied by some authors [10] [42] [24] [23] [22]. However, previous publications are mostly speculative, and assume certain simple source types in the ice plate. Also, it is not clearly understood yet how the environmental stresses are released as a major source of induced ice motion. The possible candidates are the three dominant types of crack [18]. Since the field observation of such cracks does not seem to be feasible, modeling of radiation from different types of crack is comparative to infer the source mechanism from the observed signal of the ice event. The fracture processes are expected to be different depending on the material properties as well as the stress distribution, of which corresponding radiation patterns can be characterized by a set of source parameters, such as fracture type, fault orientation and dimension, and propagation speed. The waveguide nature of the laterally stratified medium affects the radiated field as well. The observed signal, therefore, contains informations characterizing such source and environmental parameters. The result of this study applied to source inversion, by which the relationship between the observed acoustic signal and the physical process of sound generation, will lead to better understanding of source mechanisms, and, consequently, of the central Arctic ambient noise as an aggregate of the individual event. Another expected application can be found in the development of remote sensing techniques suitable for the study of ice behaviour and properties.

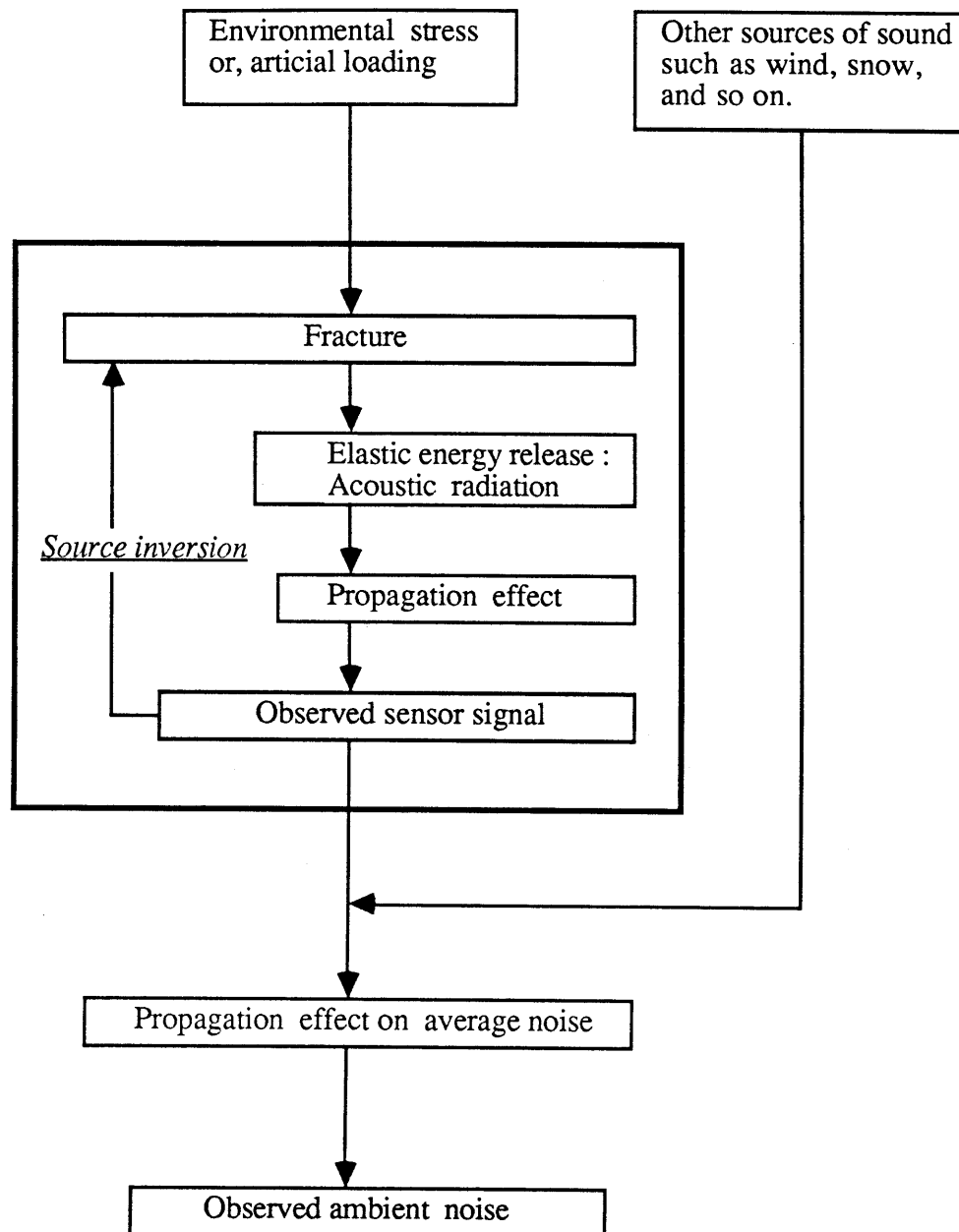


Figure 1.1: The research issue applied to the seismic study of ice and the ambient noise generation mechanism due to ice cracking noise

1.2 Objective

The thrust of the present research is, therefore, to develop a model of the elastic wave field in stratified environments for the various seismic source mechanisms. The research effort in this thesis is focused on the modeling of the physical processes of radiation from given types of source and propagation in a range-independent environment, as described in the box in Fig 1.1, i.e. simulation of the radiation patterns and time series for various given types of sources. The source types to be considered are explosive sources, point forces, shear cracks, and tensile cracks. Further the effect of transverse isotropy will be considered, which is important in sea and lake ice, and finely layered sediments.

1.3 Approach

The approach taken in modeling the radiation and propagation in a laterally stratified medium is divided into two part, the development of a mathematical representation of seismic sources and numerical solution technique for laterally stratified elastic media.

The representation of seismic sources utilizes the formulation by Keilis-Borok(1950), reviewed by Sato[36], which introduces the displacement and force potentials following the Love-Stoke formalism[25]. The formulation is compact, and can be easily transformed to cylindrical coordinates, which is more convenient for the stratified media due to the geometric nature of horizontal wave guide.

The methods available for treating the acoustic propagation problems can be categorized based on the geometry of the environmental model and the solution technique. Confining our interest to the seismic and acoustic radiation and propagation in ocean environments, the classification, based on the geometry of envi-

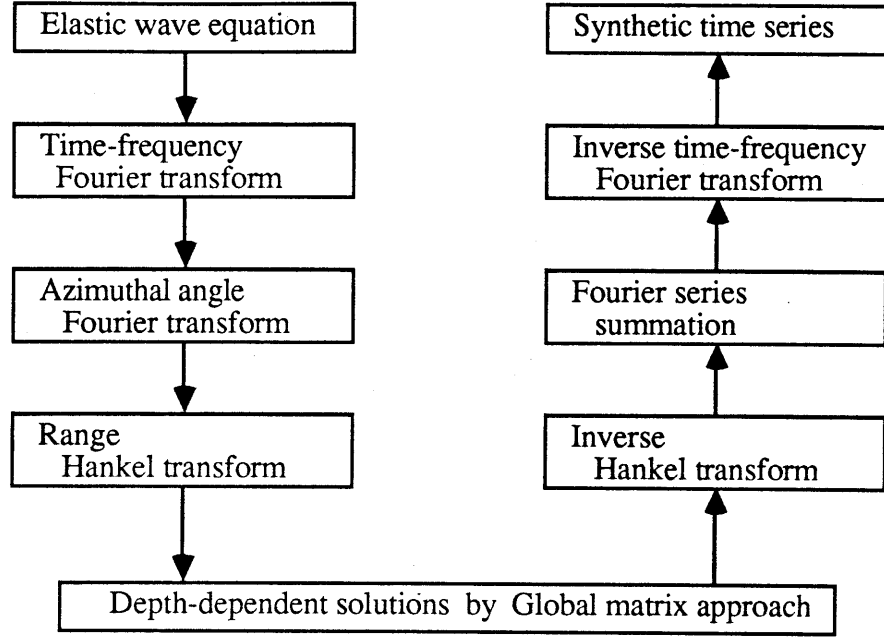


Figure 1.2: The solution technique

ronmental model, is by tradition divided into two categories, range-independent and range-dependent media. A range-independent medium is also referred to a laterally homogeneous, laterally stratified, or vertically varying medium.

Since range-dependent model allows more accurate modeling, a great amount of effort is being invested. However, the solution techniques for a range-dependent medium are certainly more complicated and computationally expensive due to the more complex of the geometry. The available methods for the range-dependent problems have certain drawbacks. For example, ray theory is a high frequency approximation with singularities such as caustics, shadow zone, and head waves, which need special treatment [7]. Modal approaches such as adiabatic and coupled modes for the range-dependent environment are available, however they do not describe the near field properly. Also, the available codes

are for acoustic media only. The parabolic equation approach is applicable to weakly range-dependent acoustic media only. Numerically intensive methods, such as finite difference method and finite element method, are available, but they are not suitable for studying the long range propagation for computational reasons.

Fortunately, for many cases, range-independent models can be applied efficiently for many ocean-sediment environments as well as the ice covered ocean found in the central Arctic, except when it is necessary to consider specific features such scattering due to ice ridges. This class of models can be modified to treat certain small imperfections such as roughness. Therefore, the solution techniques available for range-independent seem to be more suitable for our present research interest.

The most complete solution technique for range-independent environments is the integral transform methods. By means of temporal and spatial integral transforms, the partial differential equation of motion is reduced to an ordinary differential equation in the vertical space coordinate z (Fig 1.2. The inverse transforms can be evaluated analytically by means of asymptotic approximations, such as steepest descent, or stationary phase. However, to described total fields, the inverse transformation must be evaluated numerically. The transform method can be classified as three well known methods. First, matrix method uses the time-frequency Fourier transform in order to formulate the equation of motion in frequency domain. After reducing the partial differential equation to an ordinary differential equation, a linear system of equations can be obtained for each discretized horizontal wave numbers to evaluate the wave number inverse transform. Second, in modal method, the difference to matrix approach is that the integral transform is replaced modal sum, which is equivalent to neglecting the near field effects. Also, although the theory is being developed to

solve for elastic media, modal method is mostly limited to an acoustic medium. In generalized ray theory, the time-frequency inverse transform is applied first, then the inverse wave number integration is evaluated [6]. Although ray theory and modal method can be extended to laterally inhomogeneous medium, the matrix approach proves to be the most widely used method for laterally homogeneous medium. Especially, the global matrix approach applied here give full wave solution for all layers solving the azimuthal Fourier orders simultaneously.

The solution technique in a laterally stratified medium uses cylindrical coordinates. The advantage of using cylindrical coordinates in range-independent environment is that only one integral transform in variable r is necessary since the azimuthal angle is in the form of Fourier summation, while, in rectangular coordinates, two integral transformations in x and y are involved resulting in the numerical inefficiency when evaluating the inverse transforms. In cylindrical coordinates, the equation of motion is depth-separated by Fourier transform in the azimuthal angle and Hankel transform in range. The remaining ordinary differential equation in the depth coordinate z with proper boundary conditions for horizontal interfaces yields a set of linear system of equation for each interface. The local matrix is properly combined to yield the global matrix, giving a full wave solution simultaneously for each azimuthal Fourier orders, and for all layers. Once the depth-dependent solutions are found for each layers, the inverse Hankel transform is performed for each azimuthal Fourier order. Now, the frequency domain solution is found by summing the Fourier orders. Finally, the time domain solution is found by frequency-time inverse Fourier transform (Fig 1.2).

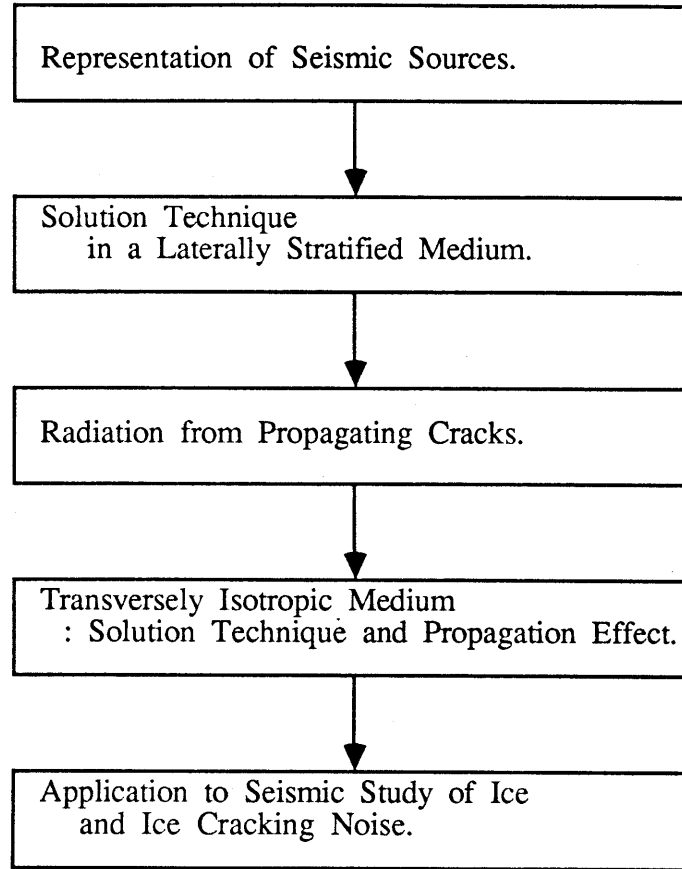


Figure 1.3: Overview of the thesis

1.4 Overview of the Thesis

This section is intended as an introductory overview of the thesis. The topics treated in each chapters are shown in Fig 1.3. The methodology is discussed in somewhat detail, and the results are briefly presented.

In Chapter 2, the compact representation of seismic sources in a homogeneous, unbounded medium is discussed. First, the radiation due to a single body force with arbitrary direction in a homogeneous medium is derived. Introducing the Keilis-Borok's compact formulation of arbitrary source time function,

and again considering harmonic source function, the formulation in frequency domain, which is relevant to present approach, is found. Then, the modeling of seismic sources in a homogeneous medium is considered through the representation theorem and Burridge and Knopoff [5], by which displacement discontinuities are replaced with equivalent body forces. Accordingly, the higher order sources, such as shear crack and tensile crack sources, are represented as superpositions of force couples in certain directions. In order to construct the force couples to form higher order sources, a unified approach to represent all compact sources by force potentials, following the Love-Stoke formalism, is discussed and presented.

In Chapter 3, in order to incorporate these source terms into a propagation model determining the full solution in a laterally stratified medium, the depth-dependent Green's functions in cylindrical coordinates are derived for each type of source in Section 2. The homogeneous solutions in a laterally stratified medium in cylindrical coordinates are assumed, by which the equation of motion is separated into wave equations for each potentials by azimuthal angle Fourier transform and Hankel transform in range. The remaining ordinary differential equation with respect to z with a proper set of boundary conditions for horizontal interfaces yields a set of linear system of equation for each interfaces. The local matrices are properly combined to yield the global matrix, giving a full wave solution simultaneously for all layers. Once the depth-dependent solutions are found for each layers, the inverse Hankel transform is performed for each azimuthal Fourier orders. The frequency domain solution is found by summing the Fourier orders. Time domain solution is found by frequency-time inverse Fourier transform. In this research, the prototype of three dimensional version of a Fast Field Program (FFP), so called Seismo-Acoustic Fast field Algorithm in Range Independent environment (SAFARI), which has been developed by

Schmidt and Glattetre[38] is further developed to take seismic source terms, and to solve the propagation in a stratified medium. This particular solution technique is chosen due to the efficient simultaneous treatment of the several azimuthal Fourier orders of the field.

In Chapter 4, a model for radiation from the non-compact, or propagating crack is formulated, first for an unbounded homogeneous medium and then, for a stratified medium. The field caused by the moving crack is basically found by integrating the proper source Green's function over the fault surface, where the source needs to be placed off the z -axis. The mathematical treatment of the source off the z -axis involves the calculation of higher order Bessel function [38], which causes the numerical inefficiency and convergence problems. Therefore, a simple transform of the source and receiver position is used in this study so that the source is always on the z -axis. Some simple examples are discussed for which the analytical solution exists. The distinct characteristics of the radiation pattern shows the directivity pattern dependent on the ratio of wave length to crack dimension. When this ratio is large, the source can be treated as a compact source. When the ratio is small, the field is highly directional. The synthetic time series show the characteristics of the convolved source signal with the dimension of the crack surface, such as the stopping phase, and poor correlation between channels, and signal duration depending on the observation positions.

Next, in Chapter 5, the propagation in a transversely isotropic medium, which is characterized by 5 elastic constants, is considered. The equation of motion is no longer reduced to the wave equation. However, the intermediate functions can be defined to decouple the equation of motion for SH and $SV - P$ waves in cylindrical coordinates. The decoupled equations give 6 eigenvalues and eigenvectors for up-going and down-going components of SH , SV , and P

waves, respectively. Those intermediate functions are combined to formulate a set of boundary conditions compatible with the Global Matrix method. An example in a homogeneous unbounded medium shows the expected separation of SH and SV waves when propagating in horizontal direction, which results from the different shear modulus for vertical and horizontal directions. The slowness surfaces are given and discussed for the example.

Chapter 6 discusses the crack radiation from the 3 modes of crack in a floating ice plate. The discussion is focused on the characterization of each source in terms of radiation and temporal characteristics. The radiation from propagating cracks is also included for a typical set of source parameters. The variation of the field due to source parameter changes are briefly discussed, including the effect of the environmental parameters such as the anisotropy of the sea ice. For source inversion from the data, more importantly to test the developed model, an experiment is proposed. The objectives of this experiment include studying the relationship between the observed acoustic signal and the physical process of fracture mechanism, and further the mechanical behavior and properties of ice under different loading conditions.

Finally, Chapter 7 summarizes the results and the discussions encountered through the research, along with suggestions for further studies.

Chapter 2

Representation of Seismic Sources

In this chapter, the representation of seismic sources in an unbounded homogeneous, and isotropic medium is considered in terms of equivalent body forces.

First, the representation theorem [1] [4] is introduced to represent the fault motion by the body force equivalents, which are the double couples [5]. In order to formulate the double couples in a compact form using Keilis-Borok's results, the radiation from a single force is discussed in detail. The force and displacement potentials are consistently used for ease and well defined mathematical manipulation, which is only possible for an isotropic medium¹. The single couples are shown to be obtained from the force by taking proper derivatives depending on the direction, and the double couples are found from the linear combination of single couples. Finally, the body force equivalents for seismic sources such as strike-slip, dip-slip, and tensile crack with certain dip angle are summarized. These results will be, in Chapter 3, transformed into

¹The formulation of homogeneous solution in a transversely isotropic medium is discussed in Chapter 5

cylindrical coordinates in order to allow an arbitrary dip angle, yielding a depth dependent source functions.

2.1 Representation Theorem and Body Force Equivalents for Seismic Sources

The mathematical description of seismic sources has been pursued along two different lines[1] : First, in terms of body forces ; second, in terms of discontinuities in displacement or strain across a rupturing fault surface or across the surface of a volume source. When the representation theorem is used, it can be shown that the discontinuity of displacement and stress can be expressed in terms of body force equivalent. Consequently, the representation theorem was used by Burridge and Knopoff [5] to show that the body force equivalents for fault motion are double couples. The details will be given in the followings.

The displacement due to body force \mathbf{f} , displacement discontinuity $[\mathbf{u}]$, and the traction $[\mathbf{T}(\mathbf{u}, \mathbf{n})]$ is, from the representation theorem, expressed as

$$\begin{aligned} u_n(\mathbf{x}, t) = & \int_{-\infty}^{\infty} d\tau \iiint_V \underbrace{f_p(\boldsymbol{\eta}, \tau) G_{np}(\mathbf{x}, t - \tau; \boldsymbol{\eta}, 0)}_{\text{I}} dV(\boldsymbol{\eta}) \\ & + \int_{-\infty}^{\infty} d\tau \iint_{\Sigma} \underbrace{\{[u_i(\boldsymbol{\xi}, \tau)] c_{ijpq} n_j G_{np,q}(\mathbf{x}, t - \tau, \boldsymbol{\xi}, 0)\}}_{\text{II}} \\ & \underbrace{-[T_p(\mathbf{u}(\boldsymbol{\xi}, \tau), \mathbf{n})] G_{np}(\mathbf{x}, t - \tau; \boldsymbol{\xi}, 0)\}_{}}_{\text{III}} d\Sigma(\boldsymbol{\xi}) . \end{aligned} \quad (2.1)$$

The first term represents the body force contribution, while II and III are due to the displacement and traction discontinuity contributions, respectively. Now, neglecting the presence of body force and traction, only the second term remains. And, using the relation

$$\frac{\partial}{\partial \xi_q} G_{np}(\mathbf{x}, t - \tau; \boldsymbol{\xi}, 0) = - \iiint_V \frac{\partial}{\partial \eta_q} \delta(\boldsymbol{\eta} - \boldsymbol{\xi}) G_{np}(\mathbf{x}, t - \tau; \boldsymbol{\eta}, 0) dV(\boldsymbol{\eta}) , \quad (2.2)$$

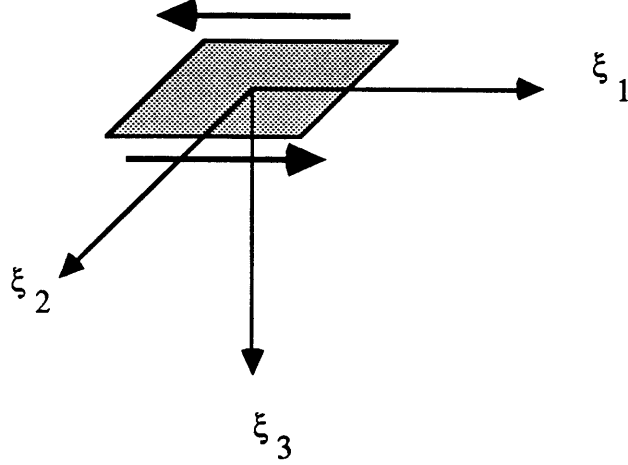


Figure 2.1: Fault motion.

the second term in Eq 2.1 due to displacement discontinuity reduces to

$$u_n(x, t) = \int_{-\infty}^{\infty} d\tau \iiint_V f_p^{[u]}(\eta, \tau) G_{np}(\mathbf{x}, t - \tau; \eta, 0) dV(\eta) , \quad (2.3)$$

where the equivalent body force for the displacement discontinuity $[u]$ is

$$f_p^{[u]}(\eta, \tau) = - \iint_{\Sigma} [u_i(\xi, \tau)] c_{ijpq} n_j \frac{\partial}{\partial \eta_q} \delta(\eta - \xi) d\Sigma . \quad (2.4)$$

Note that the surface integral for displacement discontinuity in the second term in Eq 2.1 has been expressed in terms of body force equivalent in Eq 2.4, of which form is found in the first term I in Eq 2.1.

As an example of a buried fault as shown in Fig 2.1, the equivalent body forces can be derived from Eq 2.4,

$$\begin{aligned} f_1(\eta, \tau) &= -M_0 \delta(\eta_1) \delta(\eta_2) \frac{\partial}{\partial \eta_3} \delta(\eta_3) X_0(\tau) , \\ f_2(\eta, \tau) &= 0 , \\ f_3(\eta, \tau) &= -M_0 \frac{\partial}{\partial \eta_1} \delta(\eta_1) \delta(\eta_2) \delta(\eta_3) X_0(\tau) , \end{aligned} \quad (2.5)$$

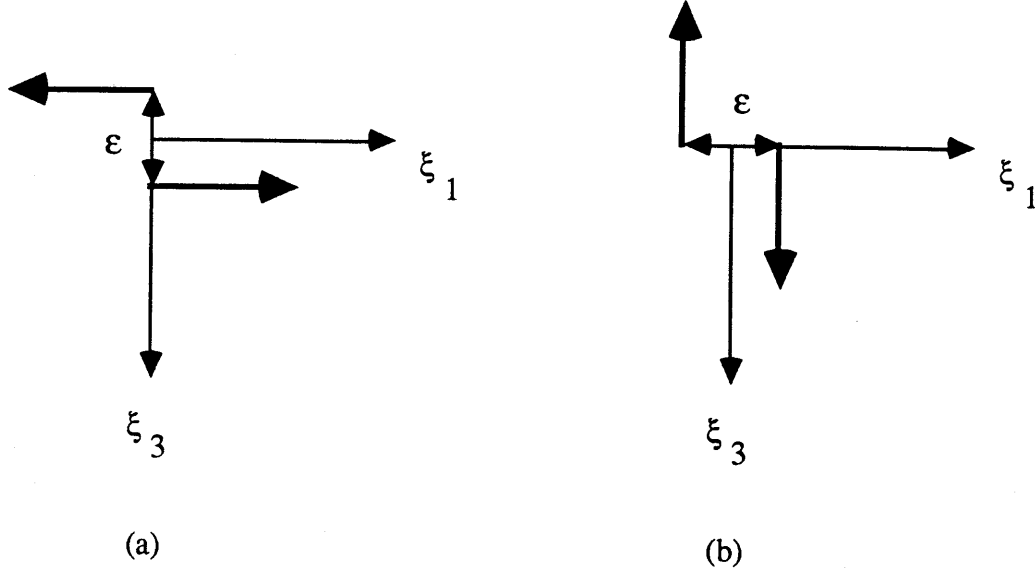


Figure 2.2: Body force equivalents for derivatives of Green's function.

where the seismic moment M_0 in an isotropic medium is defined as

$$M_0 = \mu \bar{u} A = \mu \times \text{average slip} \times \text{fault area} . \quad (2.6)$$

The corresponding displacement, from Eq 2.3 using Eq 2.2, is expressed as

$$u_n(x, t) = \int_{-\infty}^{\infty} d\tau \iint_{\Sigma} \mu [u_1] \left\{ \frac{\partial G_{n1}}{\partial \xi_3} + \frac{\partial G_{n3}}{\partial \xi_1} \right\} d\Sigma. \quad (2.7)$$

In fact, the first and second terms in the curly bracket in Eq 2.7 represent single couples in Fig 2.2. Since the two forces are combined in such a way that the magnitude of moment remains constant while ϵ goes to zero, i.e. $\lim_{\epsilon \rightarrow 0} \epsilon X_0 = M_0$, the single couples appear to be derivatives of a single body force.

In the following sections, the more compact form of seismic source representation using displacement and force potentials is derived based on the Love-Stokes formalism, following Sato [36].

2.2 Radiation from Body Forces in a Homogeneous Isotropic Medium

As a basic ingredient in the representation of the various sources, the radiation field due to a single body force is derived in detail.

The displacement equation of motion for a homogeneous isotropic medium is

$$\mu \nabla^2 \mathbf{u} + (\lambda + \mu) \nabla (\nabla \cdot \mathbf{u}) + \rho \mathbf{F} = \rho \frac{\partial^2 \mathbf{u}}{\partial t^2}, \quad (2.8)$$

where μ and λ are Lamé constants and \mathbf{u} is displacement, ρ is density, and \mathbf{F} is a body force. Or, equivalently

$$(\lambda + 2\mu) \nabla (\nabla \cdot \mathbf{u}) - \mu \nabla \times \nabla \times \mathbf{u} + \rho \mathbf{F} = \rho \frac{\partial^2 \mathbf{u}}{\partial t^2}. \quad (2.9)$$

Taking the divergence and curl of Eq 2.9, we obtain

$$c_c^2 \nabla^2 \nabla \cdot \mathbf{u} + \nabla \cdot \mathbf{F} = \frac{\partial^2 \nabla \cdot \mathbf{u}}{\partial t^2}, \quad (2.10)$$

and

$$c_s^2 \nabla^2 \nabla \times \mathbf{u} + \nabla \times \mathbf{F} = \frac{\partial^2 \nabla \times \mathbf{u}}{\partial t^2} \quad (2.11)$$

with

$$c_c = \left(\frac{\lambda + 2\mu}{\rho} \right)^{1/2}, \quad c_s = \left(\frac{\mu}{\rho} \right)^{1/2}. \quad (2.12)$$

being the compressional and shear velocities, respectively.

Introducing body force potentials and displacement potentials,

$$\mathbf{F} = (X, Y, Z) = \nabla \Phi + \nabla \times (L, M, N), \quad (2.13)$$

$$\mathbf{u} = (u, v, w) = \nabla \phi + \nabla \times (F, G, H), \quad (2.14)$$

Eqs 2.10 and 2.11 become

$$c_c^2 \nabla^2 \phi + \Phi = \frac{\partial^2 \phi}{\partial t^2}$$

$$\begin{aligned}
c_s^2 \nabla^2 F + L &= \frac{\partial^2 F}{\partial t^2} \\
c_s^2 \nabla^2 G + M &= \frac{\partial^2 G}{\partial t^2} \\
c_s^2 \nabla^2 H + N &= \frac{\partial^2 H}{\partial t^2}
\end{aligned} \tag{2.15}$$

Now, the particular solution of Eq 2.15 can be expressed in the forms.

$$\begin{aligned}
\phi &= \frac{1}{4\pi c_s^2} \iiint \frac{1}{r} \Phi' \left(t - \frac{r}{c_s} \right) dx'_1 dx'_2 dx'_3 \\
F &= \frac{1}{4\pi c_s^2} \iiint \frac{1}{r} L' \left(t - \frac{r}{c_s} \right) dx'_1 dx'_2 dx'_3 \\
G &= \frac{1}{4\pi c_s^2} \iiint \frac{1}{r} M' \left(t - \frac{r}{c_s} \right) dx'_1 dx'_2 dx'_3 \\
H &= \frac{1}{4\pi c_s^2} \iiint \frac{1}{r} N' \left(t - \frac{r}{c_s} \right) dx'_1 dx'_2 dx'_3
\end{aligned} \tag{2.16}$$

where Φ, L, M and N are found from

$$\begin{aligned}
\Phi &= -\frac{1}{4\pi} \iiint \left(X' \frac{\partial r^{-1}}{\partial x_1} + Y' \frac{\partial r^{-1}}{\partial x_2} + Z' \frac{\partial r^{-1}}{\partial x_3} \right) dx'_1 dx'_2 dx'_3 \\
L &= \frac{1}{4\pi} \iiint \left(Z' \frac{\partial r^{-1}}{\partial x_2} - Y' \frac{\partial r^{-1}}{\partial x_3} \right) dx'_1 dx'_2 dx'_3 \\
M &= \frac{1}{4\pi} \iiint \left(X' \frac{\partial r^{-1}}{\partial x_3} - Z' \frac{\partial r^{-1}}{\partial x_1} \right) dx'_1 dx'_2 dx'_3 \\
N &= \frac{1}{4\pi} \iiint \left(Y' \frac{\partial r^{-1}}{\partial x_1} - X' \frac{\partial r^{-1}}{\partial x_2} \right) dx'_1 dx'_2 dx'_3
\end{aligned} \tag{2.17}$$

where t is the time and $r = \sqrt{(x_1 - x'_1)^2 + (x_2 - x'_2)^2 + (x_3 - x'_3)^2}$. The proof of Eq 2.16 for displacement potentials is drawn basically from the Poisson equation solution in an unbounded medium [25, pp.304] [1, pp.64–67] [35, §276]. Eq 2.17 for force potentials is also proved utilizing the solution for vector Poisson equation² [25, pp.184] [1, pp.69]. In the above expressions, the unit of vector quantity

²Since the proof is elegant and educational, it is given. Force is defined through force potentials, $\mathbf{F} = (X, Y, Z) = \nabla\Phi + \nabla \times (L, M, N)$. A vector Poisson equation for \mathbf{W} can be constructed with \mathbf{F} as source term, $\mathbf{F} = \nabla^2 \mathbf{W}$, which can be rewritten as $\mathbf{F} = \nabla(\nabla \cdot \mathbf{W}) - \nabla \times (\nabla \times \mathbf{W})$.

X' is *acceleration*, i.e. m/sec^2 , and the scalar quantity $X_0(t - r/c_c)$ is source time function and has the unit of *force*. Finally, substitution of Eq 2.17 into Eq 2.16 yields the displacement potentials. The volume integral for displacement potentials can be evaluated for an arbitrary source function by conversion into a surface integral ; details are given by Aki[1, pp. 71].

The general formulation of particular solution to the wave equation with a body force source in an unbounded medium has been derived, where the source function can be completely arbitrary. An example for a horizontal force with harmonic time dependence will be derived following the steps presented previously. Later in Chapter 2.5, when the body force equivalents for seismic sources are formulated in the form of force potentials, the results will be used to find displacement field due to corresponding force potentials. The usage of harmonic source function has been chosen, because the time domain solution for an arbitrary source function can be found by time-frequency Fourier synthesis.

Example : Radiation from a single force in x -direction

For the case of horizontal force in x_1 -direction with harmonic time dependence i.e. $\mathbf{F} = X_0\delta(\mathbf{x})\mathbf{e}_1$, Eq 2.17 is simplified as follows,

$$\begin{aligned}\Phi &= -\frac{1}{4\pi} \iiint \left(X' \frac{\partial r^{-1}}{\partial x_1} \right) dx'_1 dx'_2 dx'_3 \\ L &= 0 \\ M &= \frac{1}{4\pi} \iiint \left(X' \frac{\partial r^{-1}}{\partial x_3} \right) dx'_1 dx'_2 dx'_3\end{aligned}\tag{2.19}$$

It is noted that the force potentials are now expressed in terms of \mathbf{W} as, $\Phi = \nabla \cdot \mathbf{W}$, and $(L, M, N) = \nabla \times \mathbf{W}$. The solution \mathbf{W} for the vector Poisson equation is

$$\mathbf{W} = - \iiint \frac{\mathbf{F}(\xi)}{4\pi|\mathbf{x} - \xi|} dV(\xi)\tag{2.18}$$

When the above equation 2.18 is substituted into the expressions for force potentials, $\Phi = \nabla \cdot \mathbf{W}$ and $(L, M, N) = \nabla \times \mathbf{W}$, Eq 2.17 is proved.

$$N = \frac{1}{4\pi} \iiint \left(X' \frac{\partial r^{-1}}{\partial x_2} \right) dx'_1 dx'_2 dx'_3$$

The volume integrals in Eq 2.19 can be found using relation

$$\rho \iiint X' dx'_1 dx'_2 dx'_3 = X_0(t), \quad (2.20)$$

where \mathbf{e}_1 is an unit vector in x_1 -direction, and $X' = X_0\delta(\mathbf{x}')$, and the scalar quantity $X_0(t)$ is a source time function. Then, the force potential reduces to

$$\Phi = -\frac{X_0}{4\pi\rho} \frac{\partial r^{-1}}{\partial x_1}, \quad L = 0, \quad M = \frac{X_0}{4\pi\rho} \frac{\partial r^{-1}}{\partial x_3}, \quad M = -\frac{X_0}{4\pi\rho} \frac{\partial r^{-1}}{\partial x_2}. \quad (2.21)$$

Substituting Eq 2.49 into Eq 2.16, the displacement potentials are found to be

$$\begin{aligned} \phi(\mathbf{r}, t) &= -\frac{1}{(4\pi c_c)^2 \rho} \iiint \frac{1}{r} X'_0 \left(t - \frac{r}{c_c} \right) \frac{\partial r^{-1}}{\partial x_1} dx'_1 dx'_2 dx'_3 \\ F(\mathbf{r}, t) &= 0 \\ G(\mathbf{r}, t) &= \frac{1}{(4\pi c_s)^2 \rho} \iiint \frac{1}{r} X'_0 \left(t - \frac{r}{c_s} \right) \frac{\partial r^{-1}}{\partial x_1} dx'_1 dx'_2 dx'_3 \\ H(\mathbf{r}, t) &= -\frac{1}{(4\pi c_s)^2 \rho} \iiint \frac{1}{r} X'_0 \left(t - \frac{r}{c_s} \right) \frac{\partial r^{-1}}{\partial x_1} dx'_1 dx'_2 dx'_3 \end{aligned} \quad (2.22)$$

The volume integral for displacement potentials can be evaluated for an arbitrary source function by conversion into a surface integral ;

$$\begin{aligned} \phi &= -\frac{1}{4\pi\rho} \frac{\partial}{\partial x_1} \frac{1}{r} \int_0^{\frac{r}{c_c}} \tau X_0(t - \tau) d\tau \\ F &= 0 \\ G &= \frac{1}{4\pi\rho} \frac{\partial}{\partial x_3} \frac{1}{r} \int_0^{\frac{r}{c_s}} \tau X_0(t - \tau) d\tau \\ H &= -\frac{1}{4\pi\rho} \frac{\partial}{\partial x_2} \frac{1}{r} \int_0^{\frac{r}{c_s}} \tau X_0(t - \tau) d\tau \end{aligned} \quad (2.23)$$

details are given by Aki[1, pp. 71].

Evaluation of the volume integral in Eq 2.22 given by Keilis-Borok (1950), reviewed in Sato [36], gives a compact result, replacing the volume integrations, by introducing the intermediate functions defined as

$$\phi_0 = \frac{1}{r} F\left(t - \frac{r}{c_c}\right), \quad \psi_0 = \frac{1}{r} F\left(t - \frac{r}{c_s}\right) \quad (2.24)$$

$$F(t) = \int_0^t ds' \int_0^{s'} X_0(s) ds \quad (2.25)$$

where $X_0(t)$ is a source function. For a harmonic time dependence of source function, i.e. $X_0(t) = X_0 e^{i\omega t}$, the Keilis-Borok's intermediate functions ϕ_0 and ψ_0 are

$$\phi_0(t) = -\frac{X_0}{\omega^2 r} e^{i\omega(t-r/c_e)} \quad , \quad \psi_0(t) = -\frac{X_0}{\omega^2 r} e^{i\omega(t-r/c_e)} \quad (2.26)$$

Using this notation, the volume integrations for displacement potentials in Eq 2.22 reduce to

$$\phi = \frac{1}{4\pi\rho} \frac{\partial \phi_0}{\partial x_1}, \quad F = 0, \quad G = -\frac{1}{4\pi\rho} \frac{\partial \psi_0}{\partial x_3}, \quad H = \frac{1}{4\pi\rho} \frac{\partial \psi_0}{\partial x_2} \quad (2.27)$$

It is pointed out that Eq 2.27 is equivalent to the result by surface integration in Eq 2.23. Using the relation given in Eq 2.14 for the displacement components, we obtain

$$\begin{aligned} \mathbf{u} &= \nabla \phi + \nabla \times (F, G, H) \\ &= \nabla \phi + \nabla \times \nabla \times (\psi_1, \psi_2, \psi_3) \end{aligned} \quad (2.28)$$

where

$$\phi = \frac{1}{4\pi\rho} \phi_0, \quad \psi_1 = -\frac{1}{4\pi\rho} \psi_0, \quad \psi_2 = 0, \quad \psi_3 = 0 \quad (2.29)$$

Similar expression may be found easily when the forces are applied in x_2 and x_3 -directions. The radiation field due to a force in an arbitrary direction also can be found by superposition of the decomposed force components in the x_1, x_2 , and x_3 -directions.

The above results are remarkably simple, and will be used subsequently to formulate the field expressions for higher order sources.

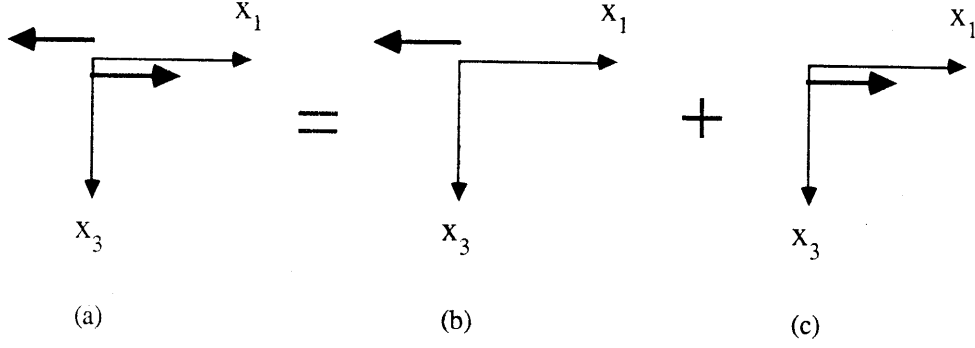


Figure 2.3: Decomposition of single couple into two body forces.

2.3 Single Couples

Potentials for single couples can be found by combining the single forces previously formulated. Instead of the force source function $X_0(t)$, the seismic moment $M_0(t)$ is used hereafter for representation of higher order sources, so that the definitions of ϕ_0 and ψ_0 are

$$\phi_0 = \frac{1}{r} F\left(t - \frac{r}{c_c}\right) \quad , \quad \psi_0 = \frac{1}{r} F\left(t - \frac{r}{c_s}\right) \quad (2.30)$$

$$F(t) = \int_0^t ds' \int_0^{s'} M_0(s) ds \quad (2.31)$$

where $M_0(t)$ is a moment source function.

The first single couple in the Fig 2.5, for example, can be generated by combining two x_1 -direction single body forces, of which formulations are given previously. The displacement potentials for the single couple in the Fig 2.3 are

easily found to be

$$\begin{aligned}
\phi &= -\frac{1}{4\pi\rho} \frac{\partial^2 \phi_0}{\partial x_3 \partial x_1} \\
F &= 0 \\
G &= -\frac{1}{4\pi\rho} \frac{\partial^2 \psi_0}{\partial x_3^2} \\
L &= \frac{1}{4\pi\rho} \frac{\partial^2 \psi_0}{\partial x_2 \partial x_3}
\end{aligned} \tag{2.32}$$

The displacement can now be written in compact form as

$$\mathbf{u} = \nabla\phi + \nabla \times \nabla \times (\psi_1, 0, 0) \quad , \tag{2.33}$$

where the potentials are

$$\phi = -\frac{1}{4\pi\rho} \frac{\partial^2 \phi_0}{\partial x_3 \partial x_1} \quad , \quad \psi_1 = \frac{1}{4\pi\rho} \frac{\partial \psi_0}{\partial x_3} \quad . \tag{2.34}$$

For the second single couple in Fig 2.5 with forces parallel to the x_3 -axis, the potentials are

$$\begin{aligned}
\phi &= -\frac{1}{4\pi\rho} \frac{\partial^2 \phi_0}{\partial x_1 \partial x_3} \\
F &= -\frac{1}{4\pi\rho} \frac{\partial^2 \psi_0}{\partial x_2 \partial x_1} \\
G &= \frac{1}{4\pi\rho} \frac{\partial^2 \psi_0}{\partial x_1^2} \\
L &= 0 \quad .
\end{aligned} \tag{2.35}$$

Again using a compact form, the displacement is

$$\mathbf{u} = \nabla\phi + \nabla \times \nabla \times (0, 0, \psi_3) \tag{2.36}$$

where the potentials are

$$\phi = -\frac{1}{4\pi\rho} \frac{\partial^2 \phi_0}{\partial x_1 \partial x_3} \quad , \quad \psi_3 = \frac{1}{4\pi\rho} \frac{\partial \psi_0}{\partial x_1} \quad . \tag{2.37}$$

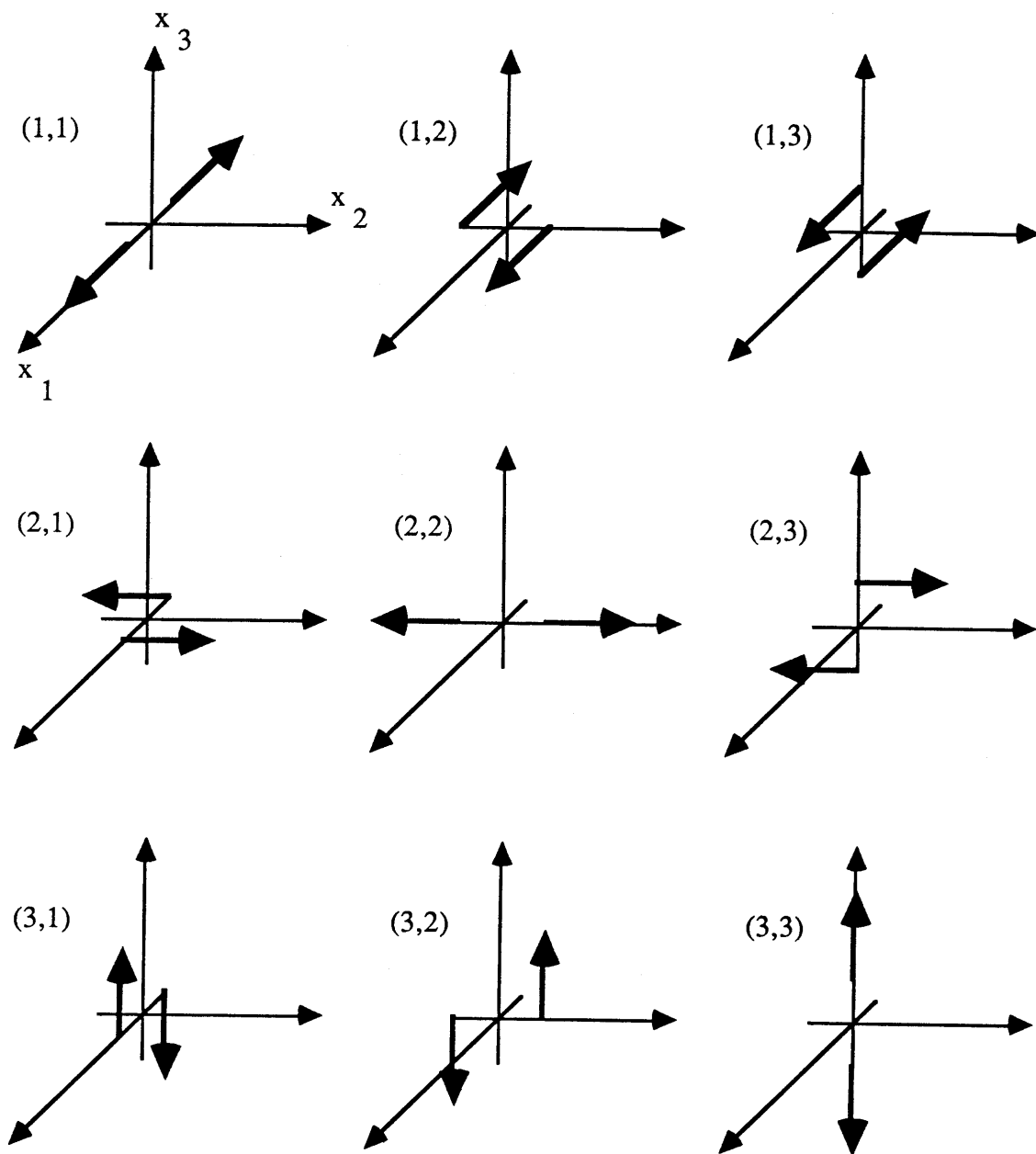


Figure 2.4: Nine single couples.

These single couples are exactly same as the example (Fig 2.2) discussed in Chapter 2.1 with different notations. The single couples in Eq 2.34 and Eq 2.37 correspond to the first and second terms in the curly bracket in Eq 2.7.

Potentials for the nine single couples (Fig 2.4) that are required to obtain equivalent body forces for a generally oriented displacement discontinuity are summarized below.

$$(1,1) \quad \phi = -\frac{1}{4\pi\rho} \frac{\partial^2 \phi_0}{\partial x_1^2}, \quad \psi_1 = \frac{1}{4\pi\rho} \frac{\partial \psi_0}{\partial x_1}, \quad \psi_2 = 0, \quad \psi_3 = 0 \quad (2.38)$$

$$(1,2) \quad \phi = -\frac{1}{4\pi\rho} \frac{\partial^2 \phi_0}{\partial x_2 \partial x_1}, \quad \psi_1 = \frac{1}{4\pi\rho} \frac{\partial \psi_0}{\partial x_2}, \quad \psi_2 = 0, \quad \psi_3 = 0 \quad (2.39)$$

$$(1,3) \quad \phi = -\frac{1}{4\pi\rho} \frac{\partial^2 \phi_0}{\partial x_3 \partial x_1}, \quad \psi_1 = \frac{1}{4\pi\rho} \frac{\partial \psi_0}{\partial x_3}, \quad \psi_2 = 0, \quad \psi_3 = 0 \quad (2.40)$$

$$(2,1) \quad \phi = -\frac{1}{4\pi\rho} \frac{\partial^2 \phi_0}{\partial x_1 \partial x_2}, \quad \psi_1 = 0, \quad \psi_2 = \frac{1}{4\pi\rho} \frac{\partial \psi_0}{\partial x_1}, \quad \psi_3 = 0 \quad (2.41)$$

$$(2,2) \quad \phi = -\frac{1}{4\pi\rho} \frac{\partial^2 \phi_0}{\partial x_2^2}, \quad \psi_1 = 0, \quad \psi_2 = \frac{1}{4\pi\rho} \frac{\partial \psi_0}{\partial x_2}, \quad \psi_3 = 0 \quad (2.42)$$

$$(2,3) \quad \phi = -\frac{1}{4\pi\rho} \frac{\partial^2 \phi_0}{\partial x_3 \partial x_2}, \quad \psi_1 = 0, \quad \psi_2 = \frac{1}{4\pi\rho} \frac{\partial \psi_0}{\partial x_3}, \quad \psi_3 = 0 \quad (2.43)$$

$$(3,1) \quad \phi = -\frac{1}{4\pi\rho} \frac{\partial^2 \phi_0}{\partial x_1 \partial x_3}, \quad \psi_1 = 0, \quad \psi_2 = 0, \quad \psi_3 = \frac{1}{4\pi\rho} \frac{\partial \psi_0}{\partial x_1} \quad (2.44)$$

$$(3,2) \quad \phi = -\frac{1}{4\pi\rho} \frac{\partial^2 \phi_0}{\partial x_2 \partial x_3}, \quad \psi_1 = 0, \quad \psi_2 = 0, \quad \psi_3 = \frac{1}{4\pi\rho} \frac{\partial \psi_0}{\partial x_2} \quad (2.45)$$

$$(3,3) \quad \phi = -\frac{1}{4\pi\rho} \frac{\partial^2 \phi_0}{\partial x_3^2}, \quad \psi_1 = 0, \quad \psi_2 = 0, \quad \psi_3 = \frac{1}{4\pi\rho} \frac{\partial \psi_0}{\partial x_3} \quad (2.46)$$

Using the single couples, the expression for a *moment* are found. For example, the x -component for a *moment* is a superposition of (3,2) and negative of (2,3). As expected, the compressional part vanishes, while only the shear potentials remain.

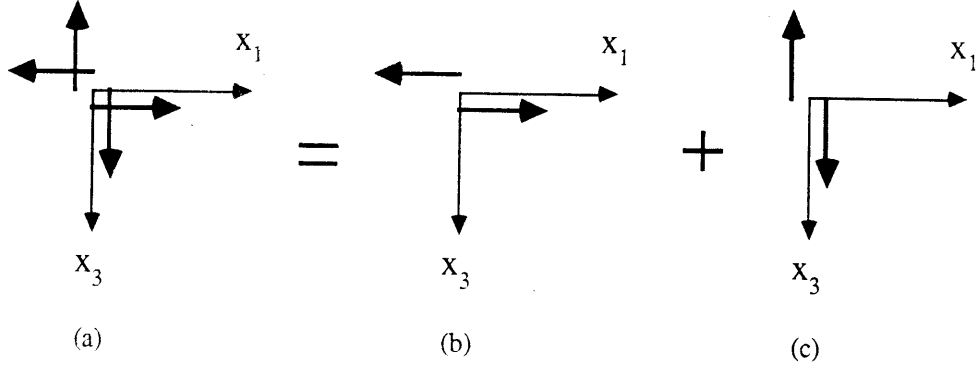


Figure 2.5: Decomposition of a double couple into two single couples.

2.4 Double Couples

The displacement for the double couple in Fig 2.5, which is a equivalent body force for strike-slip with dip angle $\delta = 0$, is simply a superposition of two single couples derived in previous section,

$$\mathbf{u} = \nabla\phi + \nabla \times \nabla \times (\psi_1, 0, \psi_3) \quad , \quad (2.47)$$

where the potentials are

$$\phi = -\frac{1}{2\pi\rho} \frac{\partial^2 \phi_0}{\partial x_1 \partial x_3} \quad , \quad \psi_1 = \frac{1}{4\pi\rho} \frac{\partial \psi_0}{\partial x_3} \quad , \quad \psi_3 = \frac{1}{4\pi\rho} \frac{\partial \psi_0}{\partial x_1} \quad . \quad (2.48)$$

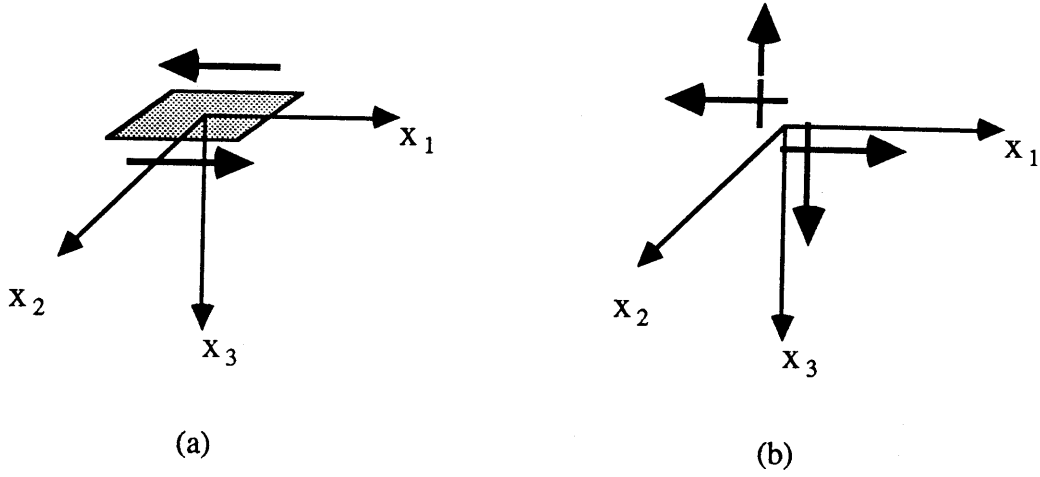


Figure 2.6: Strike-slip with dip angle $\delta = 0$ (a) fault surface and slip motion (b) equivalent body forces.

2.5 Summary of Equivalent Body Forces for Seismic Sources

Strike-slip

The double couple, which is an equivalent body force for strike-slip with dip angle $\delta = 0$ (Fig 2.6), is simply a superposition of two single couples (1,3) and (3,1), giving the following displacement potentials,

$$\phi = -\frac{1}{2\pi\rho} \frac{\partial^2 \phi_0}{\partial x_1 \partial x_3} , \quad \psi_1 = \frac{1}{4\pi\rho} \frac{\partial \psi_0}{\partial x_3} , \quad \psi_2 = 0 , \quad \psi_3 = \frac{1}{4\pi\rho} \frac{\partial \psi_0}{\partial x_1} . \quad (2.49)$$

Dip-slip

The displacement potentials for dip-slip (Fig 2.7) with dip angle $\delta = 0$, is a superposition of two negative single couples (2,3) and (3,2) in Fig 2.4, where

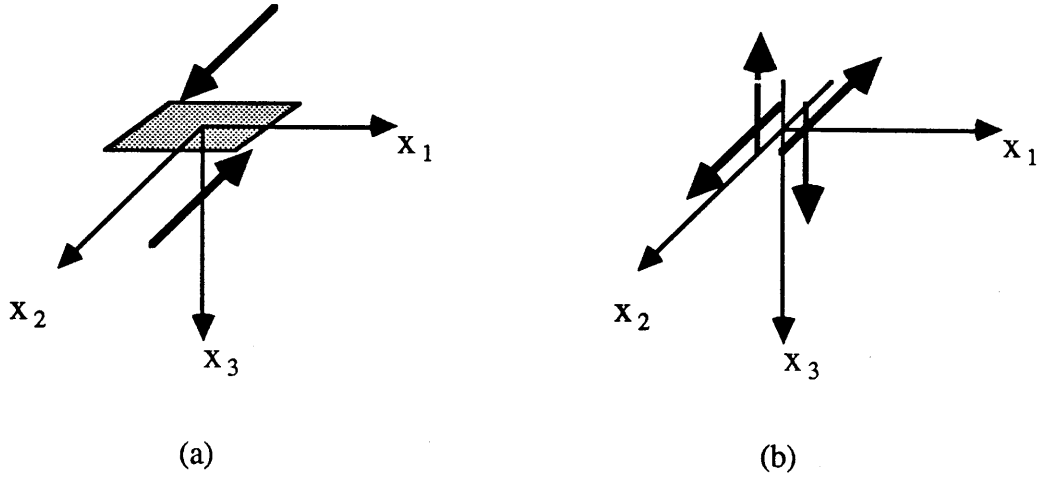


Figure 2.7: Dip-slip with dip angle $\delta = 0$ (a) fault surface and slip motion (b) equivalent body forces.

the potentials are

$$\phi = \frac{1}{2\pi\rho} \frac{\partial^2 \phi_0}{\partial x_2 \partial x_3}, \quad \psi_1 = 0, \quad \psi_2 = -\frac{1}{4\pi\rho} \frac{\partial \psi_0}{\partial x_3}, \quad \psi_3 = -\frac{1}{4\pi\rho} \frac{\partial \psi_0}{\partial x_2}. \quad (2.50)$$

The representation of shear seismic sources in rectangular coordinate system has been reviewed for certain direction of fault surfaces using Keilis-Borok's compact results. The more complete formulations, using the nine single couples, in rectangular coordinates for general shear fault surfaces with fault orientation parameters (Fig 3.2) such as dip angle(δ), rake angle(λ), and strike(ϕ_s), are found in Aki [1, pp 117-118]. The corresponding representation in cylindrical coordinates will be given in Chapter 3.2.

Tensile crack

The equivalent body force for a tensile crack can be obtained by superposing three single couples without moment, i.e. (1, 1), (2, 2), and (3, 3) in Fig 2.4, but

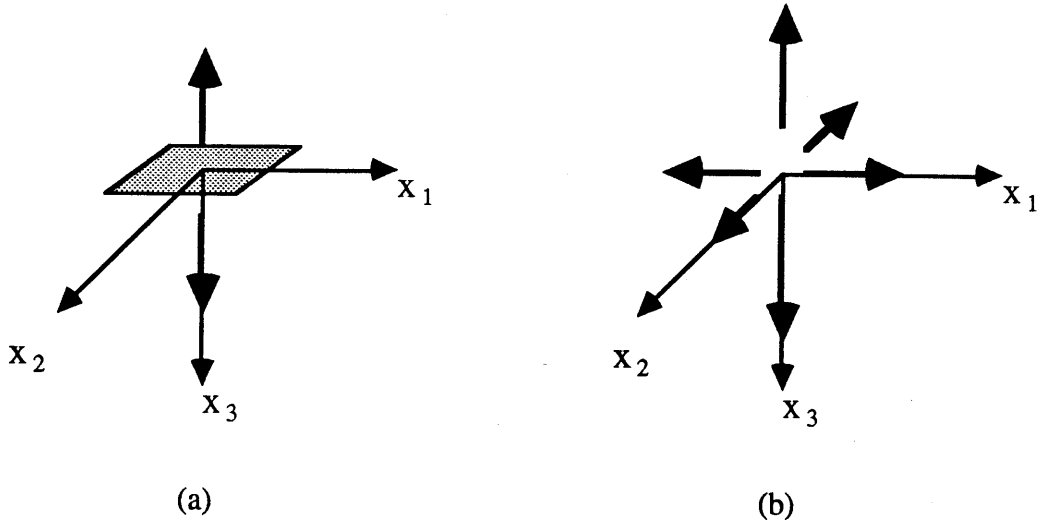


Figure 2.8: Tensile crack with dip angle $\delta = 0$ (a) fault surface and motion (b) equivalent body forces.

with different magnitude of seismic moment. Considering the fault surface with dip angle $\delta = 0$ (Fig 2.8), the direction of fault motion is in z -direction, so that the magnitude of the single couple (3,3) will be $\frac{\lambda+2\mu}{\lambda}M_0$, while the other two components are M_0 . The potentials for tensile crack shown in Fig 2.8 are then

$$\begin{aligned}
 \phi &= -\frac{1}{4\pi\rho} \frac{\partial^2 \phi_0}{\partial x_1^2} \Big|_{M=M_0} - \frac{1}{4\pi\rho} \frac{\partial^2 \phi_0}{\partial x_2^2} \Big|_{M=M_0} - \frac{1}{4\pi\rho} \frac{\partial^2 \phi_0}{\partial x_3^2} \Big|_{M=\frac{\lambda+2\mu}{\lambda}M_0}, \\
 \psi_1 &= \frac{1}{4\pi\rho} \frac{\partial \psi_0}{\partial x_1} \Big|_{M=M_0}, \\
 \psi_2 &= \frac{1}{4\pi\rho} \frac{\partial \psi_0}{\partial x_2} \Big|_{M=M_0}, \\
 \psi_3 &= \frac{1}{4\pi\rho} \frac{\partial \psi_0}{\partial x_3} \Big|_{M=\frac{\lambda+2\mu}{\lambda}M_0}.
 \end{aligned} \tag{2.51}$$

The potentials for explosive source can be found by taking same magnitude in 3 single couples without moment, yielding only compressional potentials.

Chapter 3

Field Representation in a Laterally Stratified Medium

Previously, in Chapter 2, the displacement field in a homogeneous isotropic medium excited by various kind of sources, such as forces, single couples, moments, double couples which corresponds to shear fault motion, and body force equivalents to tensile crack opening, has been discussed in Cartesian coordinates. In this Chapter, the field representation in a laterally stratified medium is considered based on global matrix method. First, the homogeneous solution in cylindrical coordinates is presented in Section 3.1, since, in a range-independent medium, two integral transforms in x and y in rectangular coordinates are reduced to a single integral transform in r in cylindrical coordinates. Then, in Section 3.2, the displacement potentials in the previous section will be transformed to represent the dislocation sources with arbitrary dip angle $\delta = 0$. These potentials are, again, transformed into cylindrical coordinates. In cylindrical coordinates, strike angle (ϕ , in Fig 3.2) can be accounted for by rotation in azimuthal angle. Since the homogeneous and source terms are in the same form of representation via Fourier decomposition in azimuthal angle θ , Hankel inte-

gral transformation in r , and finally the depth-dependent exponential form with unknown coefficients, a set of linear equations can be established by matching boundary condition at interfaces, for each discretized horizontal wave number of Hankel integral representation and, for each Fourier order of θ , which is treated in Section 3.3. In Section 3.4, the solution field parameters of interest such as stresses and displacements are found by inverse Hankel transform and then, adding all the Fourier components. Also, the numerical aspects, concerning the inverse Hankel transform are discussed. Finally, some numerical examples are given in Section 3.5.

3.1 Homogeneous Solution to Wave Equation in Cylindrical Coordinates

The homogeneous solutions to wave equations in cylindrical coordinates are represented in terms of three scalar potentials, which are related to the displacement in the following way[38],

$$\mathbf{u} = \nabla\phi + \nabla \times \nabla \times (0, 0, \Lambda) + \nabla \times (0, 0, \psi) \quad (3.1)$$

The scalar potentials satisfy the following homogeneous wave equations,

$$(\nabla^2 + h^2) \phi = 0 \quad (3.2)$$

$$(\nabla^2 + k^2) (\Lambda, \psi) = 0 \quad (3.3)$$

The potentials are expanded in Fourier series in the azimuthal angle θ , as

$$\begin{aligned} \phi(r, \theta, z) &= \sum_{m=0}^{\infty} \phi^m(r, z) \begin{bmatrix} \cos m\theta \\ \sin m\theta \end{bmatrix} \\ \Lambda(r, \theta, z) &= \sum_{m=0}^{\infty} \Lambda^m(r, z) \begin{bmatrix} \cos m\theta \\ \sin m\theta \end{bmatrix} \end{aligned} \quad (3.4)$$

$$\psi(r, \theta, z) = \sum_{m=0}^{\infty} \psi^m(r, z) \begin{bmatrix} \sin m\theta \\ -\cos m\theta \end{bmatrix}$$

By insertion of Eq 3.4 to Eq 3.1, it can be shown that the displacement components are similarly expanded as

$$\begin{aligned} w(r, \theta, z) &= \sum_{m=0}^{\infty} w^m(r, z) \begin{bmatrix} \cos m\theta \\ \sin m\theta \end{bmatrix} \\ u(r, \theta, z) &= \sum_{m=0}^{\infty} u^m(r, z) \begin{bmatrix} \cos m\theta \\ \sin m\theta \end{bmatrix} \\ v(r, \theta, z) &= \sum_{m=0}^{\infty} v^m(r, z) \begin{bmatrix} \sin m\theta \\ -\cos m\theta \end{bmatrix} \end{aligned} \quad (3.5)$$

Substitution of Eq 3.4 into the wave equations 3.2 and 3.3 results in ordinary differential equations for the expansion coefficients in Eq 3.4 after Hankel transform in range [38]. The ordinary differential equation with respect to z is solved to give the exponential form in the square bracket in the following equation 3.6, which represent the up-going and down-going waves, with the following integral representations for m -th order potentials.

$$\begin{aligned} \phi^m(r, z) &= \int_0^{\infty} [a_1^m(s)e^{-z\alpha(s)} + a_2^m(s)e^{z\alpha(s)}] sJ_m(rs)ds \\ \Lambda^m(r, z) &= \int_0^{\infty} [b_1^m(s)e^{-z\beta(s)} + b_2^m(s)e^{z\beta(s)}] J_m(rs)ds \\ \psi^m(r, z) &= \int_0^{\infty} [c_1^m(s)e^{-z\beta(s)} + c_2^m(s)e^{z\beta(s)}] sJ_m(rs)ds \end{aligned} \quad (3.6)$$

In order to match the boundary conditions at the interface, it is necessary to find the field parameters such as displacements and stresses. The constraints at

the horizontal interfaces between 2 solid media in welded contact involve :

- w : z -direction displacement
- u : r -direction displacement
- v : θ -direction displacement
- σ_{zz} : normal stress in z -direction
- σ_{rz} : shear stress in r -direction
- $\sigma_{\theta z}$: shear stress in θ -direction.

When one or two of the media joining at an interface are liquid or vacuum, some of the constraints will be no longer effective. These boundary conditions are used to determine the unknown constants which are functions of horizontal wave number s , such as $a_1(s)$, $a_2(s)$, $b_1(s)$, $b_2(s)$, $c_1(s)$ and $c_2(s)$.

Using Eq 3.6 and the relation between the displacement and displacement potentials, Eq 3.1, the field parameters given above can be shown to be [38]

$$\begin{aligned}
 w^m(r, z) &= \int_0^\infty \left[\begin{array}{l} -a_1^m(s)\alpha(s)e^{-z\alpha(s)} + a_2^m(s)\alpha(s)e^{z\alpha(s)} \\ + b_1^m(s)se^{-z\beta(s)} + b_2^m(s)se^{z\beta(s)} \end{array} \right] sJ_m(rs)ds \\
 u^m(r, z) \pm v^m(r, z) &= \int_0^\infty \left[\begin{array}{l} \mp a_1^m(s)se^{-z\alpha(s)} \mp a_2^m(s)se^{z\alpha(s)} \\ \pm b_1^m(s)\beta(s)e^{-z\beta(s)} \mp b_2^m(s)\beta(s)e^{z\beta(s)} \\ + c_1^m(s)se^{-z\beta(s)} + c_2^m(s)se^{z\beta(s)} \end{array} \right] sJ_{m\pm 1}(rs)ds
 \end{aligned}$$

$$\begin{aligned}
 \sigma_{zz}^m(r, z) &= \lambda \nabla^2 \phi^m(r, z) + 2\mu \frac{\partial}{\partial z} w^m(r, z) \\
 &= \mu \int_0^\infty \left[\begin{array}{l} a_1^m(s)(2s^2 - k^2)e^{-z\alpha(s)} + a_2^m(s)(2s^2 - k^2)e^{z\alpha(s)} \\ - b_1^m(s)2s\beta(s)e^{-z\beta(s)} + b_2^m(s)2s\beta(s)e^{z\beta(s)} \end{array} \right] sJ_m(rs)ds
 \end{aligned} \tag{3.7}$$

$$\sigma_{rz}^m(r, z) \pm \sigma_{\theta z}^m(r, z) = \mu \left[\frac{\partial}{\partial z} [u^m(r, z) \pm v^m(r, z)] + \left(\frac{\partial}{\partial r} \mp \frac{m}{r} \right) w^m(r, z) \right]$$

$$= \mu \int_0^\infty \left[\begin{array}{l} \pm a_1^m(s) 2s\alpha(s) e^{-z\alpha(s)} \mp a_2^m(s) 2s\alpha(s) e^{z\alpha(s)} \\ \mp b_1^m(s) (2s^2 - k^2) e^{-z\beta(s)} \mp b_2^m(s) (2s^2 - k^2) e^{z\beta(s)} \\ - c_1^m(s) s\beta(s) e^{-z\beta(s)} + c_2^m(s) s\beta(s) e^{z\beta(s)} \end{array} \right] s J_{m\pm 1}(sr) ds$$

In the above equation 3.7, it is noted that the shear displacements and stresses are added and subtracted giving the Hankel transform for a single order of Bessel function, i.e J_{m+1} for addition and J_{m-1} for subtraction, respectively. Otherwise, the shear displacements and stresses in certain directions will involve Bessel functions of two different orders, which greatly complicates analysis using a linear system of equations. This is an essential manipulation in order to be able to apply global matrix approach. The homogeneous solutions to the wave equations, and corresponding displacements and stresses have been given. The coefficients are later found by matching the boundary conditions for a given excitation. In the following section, the source potentials are transformed into the cylindrical coordinate system to have same form of representation as homogeneous solutions found in Eq 3.6.

3.2 Seismic Source Green's Function in Cylindrical Coordinates

The displacement potentials for various sources given previously needs to be formulated in cylindrical coordinates with the same form of Fourier decomposition in θ -direction as applied to the homogeneous solutions in order to set up a global linear system of equations expressing the boundary conditions. For strike-slip, the derivations are given rather in detail, while only the results are given for the dip-slip and tensile crack.

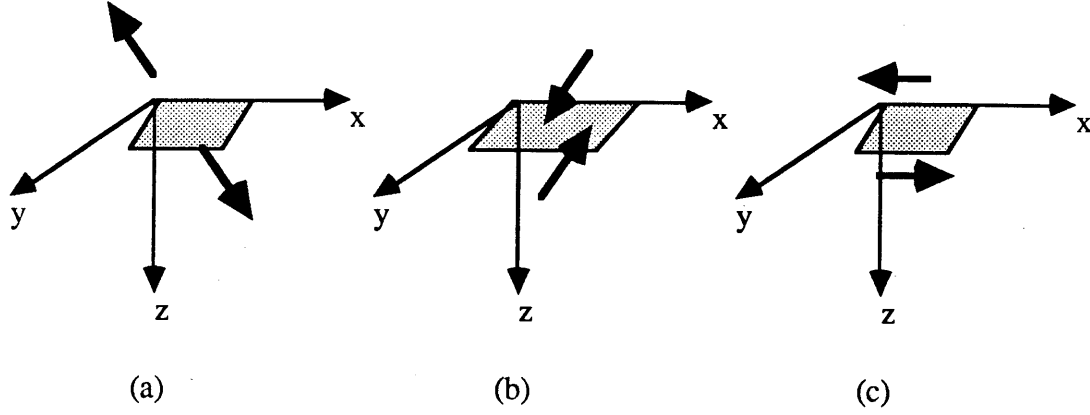


Figure 3.1: Fault motion with dip angle δ , (a) Tensile crack, (b) dip-slip, (c) strike-slip.

3.2.1 strike-slip

The displacements in terms of displacement potential given in Eq 2.49 will be first transformed into a strike-slip with dip angle δ .

Denoting the original coordinates system (x_1, x_2, x_3) and using a following transformation (Fig 3.1), the strike-slip has dip angle δ in the coordinate system (x, y, z) ,

$$\begin{aligned}
 \phi &= -\frac{1}{2\pi\rho} \frac{\partial}{\partial x} \left(-\sin \delta \frac{\partial}{\partial y} + \cos \delta \frac{\partial}{\partial z} \right) \phi_0 \\
 \psi_x &= \frac{1}{4\pi\rho} \left(-\sin \delta \frac{\partial}{\partial y} + \cos \delta \frac{\partial}{\partial z} \right) \psi_0 \\
 \psi_y &= -\frac{1}{4\pi\rho} \sin \delta \frac{\partial \psi_0}{\partial x} \\
 \psi_z &= \frac{1}{4\pi\rho} \cos \delta \frac{\partial \psi_0}{\partial x}.
 \end{aligned} \tag{3.8}$$

Again, the potentials in the rectangular coordinate system (x, y, z) needs to be transformed into cylindrical coordinate system (r, θ, z) . Note that the relations between the displacements in two coordinate systems, for example, are

$$\begin{aligned} u_x &= u_r \cos \theta - u_\theta \sin \theta \\ u_y &= u_r \sin \theta + u_\theta \cos \theta \\ u_z &= u_z \end{aligned} \quad (3.9)$$

The partial differential operators can be found using the chain rule,

$$\begin{aligned} \frac{\partial}{\partial x} &= \left(\cos \theta \frac{\partial}{\partial r} - \frac{\sin \theta}{r} \frac{\partial}{\partial \theta} \right) \\ \frac{\partial}{\partial y} &= \left(\sin \theta \frac{\partial}{\partial r} + \frac{\cos \theta}{r} \frac{\partial}{\partial \theta} \right) \\ \frac{\partial}{\partial z} &= \frac{\partial}{\partial z} \end{aligned} \quad (3.10)$$

Using the relations in Eq 3.9 and 3.10, the potentials are found as follows. The displacement expression equivalent to Eq 3.8 in cylindrical coordinates is

$$\mathbf{u} = \nabla \phi + \nabla \times \nabla \times (\psi_r, \psi_\theta, \psi_z) \quad , \quad (3.11)$$

where

$$\begin{aligned} \phi &= \frac{1}{4\pi\rho} \left[\sin \delta \sin 2\theta \left(\frac{\partial^2}{\partial r^2} - \frac{1}{r} \frac{\partial}{\partial r} \right) - 2 \cos \delta \cos \theta \frac{\partial^2}{\partial r \partial z} \right] \phi_0 \\ \psi_r &= \frac{1}{4\pi\rho} \left[-\sin \delta \sin 2\theta \frac{\partial}{\partial r} + \cos \delta \cos \theta \frac{\partial}{\partial z} \right] \psi_0 \\ \psi_\theta &= -\frac{1}{4\pi\rho} \left[\sin \delta \cos 2\theta + 2 \cos \delta \sin \theta \frac{\partial}{\partial z} \right] \psi_0 \\ \psi_z &= \frac{1}{4\pi\rho} \cos \delta \cos \theta \frac{\partial \psi_0}{\partial r} \quad . \end{aligned} \quad (3.12)$$

The potentials, ϕ_0 and ψ_0 , can now be expressed as

$$\phi_0 = -\frac{M_0}{\omega^2} \frac{1}{R} e^{i\omega(t-R/c_0)}$$

$$\begin{aligned}
&= -\frac{M_0}{\omega^2} e^{i\omega t} \int_0^\infty J_0(sr) e^{-\alpha|z-z_s|} \frac{s}{\alpha} ds \\
\psi_0 &= -\frac{M_0}{\omega^2} e^{i\omega t} \int_0^\infty J_0(sr) e^{-\beta|z-z_s|} \frac{s}{\beta} ds,
\end{aligned} \tag{3.13}$$

using the Sommerfeld-Weyl integral [45, pp. 13] ,

$$\frac{e^{-ihR}}{R} = \int_0^\infty J_0(sr) e^{-\alpha|z|} \frac{s}{\alpha} ds, \tag{3.14}$$

where $\alpha = (h^2 - s^2)^{1/2}$ for $s^2 > \text{Re}(h^2)$, and $j(h^2 - s^2)^{1/2}$ for $s^2 \leq \text{Re}(h^2)$, J_0 is zeroth order Bessel function, h is medium wave number, R is $\sqrt{r^2 + z^2}$, and s is horizontal wave number. It is noted that z in Eq 3.13 is replaced by $z - z_s$ to account for the source depth z_s , accordingly the definition of R is $R = \sqrt{r^2 + (z - z_s)^2}$.

Finally, substitution of the above Eq 3.13 into Eq 3.12 yields the potentials of strike-slip with an arbitrary dip angle δ of the same integral form as the homogeneous solution (note that ζ is defined as $\text{sign}(z - z_s)$ in the following expressions) :

$$\begin{aligned}
\phi &= -\frac{M_0}{4\pi\rho\omega^2} e^{i\omega t} \int_0^\infty \begin{bmatrix} \sin \delta \sin 2\theta s^2 J_2(sr) \\ -2 \cos \delta \cos \theta \zeta s \alpha J_1(sr) \end{bmatrix} e^{-\alpha|z-z_s|} \frac{s}{\alpha} ds \\
\psi_r &= -\frac{M_0}{4\pi\rho\omega^2} e^{i\omega t} \int_0^\infty \begin{bmatrix} \sin \delta \sin 2\theta s J_1(sr) \\ -\cos \delta \cos \theta \zeta \beta J_0(sr) \end{bmatrix} e^{-\beta|z-z_s|} \frac{s}{\beta} ds \\
\psi_\theta &= -\frac{M_0}{4\pi\rho\omega^2} e^{i\omega t} \int_0^\infty \begin{bmatrix} \sin \delta \cos 2\theta s J_1(sr) \\ +\cos \delta \sin \theta \zeta \beta J_0(sr) \end{bmatrix} e^{-\beta|z-z_s|} \frac{s}{\beta} ds \\
\psi_z &= \frac{M_0}{4\pi\rho\omega^2} e^{i\omega t} \int_0^\infty \cos \delta \cos \theta s J_1(sr) e^{-\beta|z-z_s|} \frac{s}{\beta} ds
\end{aligned} \tag{3.15}$$

Unlike the homogeneous solution, the potentials $\phi, \psi_r, \psi_\theta, \psi_z$ rather than ϕ, Λ, ψ are used in particular solution, since the particular solutions are found by transformation of the rectangular coordinate formulation to give, naturally, the coupled potential representation. while the uncoupled homogeneous solutions are

found from the separated, uncoupled wave equations. The expressions in the same form as the homogeneous solution, ϕ , Λ , and ψ , can be shown to be

$$\begin{aligned}
\phi &= -\frac{M_0}{4\pi\rho\omega^2}e^{i\omega t}\int_0^\infty \begin{bmatrix} \sin\delta\sin 2\theta s^2 J_2(sr) \\ -2\cos\delta\cos\theta\zeta s\alpha J_1(sr) \end{bmatrix} e^{-\alpha|z-z_*|\frac{s}{\alpha}}ds \\
\Lambda &= \frac{M_0}{4\pi\rho\omega^2}e^{i\omega t}\int_0^\infty \begin{bmatrix} \sin\delta\cos\theta s\frac{2s^2-k^2}{s}J_1(sr) \\ -\sin\delta\cos 2\theta\zeta\beta J_2(sr) \end{bmatrix} e^{-\beta|z-z_*|\frac{s}{\beta}}ds \\
\psi &= \frac{M_0}{4\pi\rho\omega^2}e^{i\omega t}\int_0^\infty \begin{bmatrix} \cos\delta\sin\theta\zeta\beta\frac{k^2}{s}J_1(sr) \\ +\sin\delta\cos 2\theta k^2 J_2(sr) \end{bmatrix} e^{-\beta|z-z_*|\frac{s}{\beta}}ds
\end{aligned} \tag{3.16}$$

For the purpose of formulating the boundary conditions at the interface, the displacements and stresses can be calculated from either of potentials in Eq 3.15 and 3.16.

3.2.2 Dip-slip

The potentials for dip-slip are similarly,

$$\begin{aligned}
\phi &= -\frac{M_0}{4\pi\rho\omega^2}e^{i\omega t}\int_0^\infty \begin{bmatrix} 0.5\sin 2\delta\{\cos 2\theta s^2 J_2(sr) \\ +(2\alpha^2 + s^2)J_0(sr)\} \\ +2\cos 2\delta\sin\theta\zeta s\alpha J_1(sr) \end{bmatrix} e^{-\alpha|z-z_*|\frac{s}{\alpha}}ds \\
\psi_r &= \frac{M_0}{4\pi\rho\omega^2}e^{i\omega t}\int_0^\infty \begin{bmatrix} \sin 2\delta\sin\theta s J_1(sr) \\ -\cos 2\delta\zeta\beta J_0(sr) \end{bmatrix} e^{-\beta|z-z_*|\frac{s}{\beta}}ds \\
\psi_\theta &= -\frac{M_0}{4\pi\rho\omega^2}e^{i\omega t}\int_0^\infty \begin{bmatrix} \sin 2\delta\sin\theta s J_1(sr) \\ -\cos 2\delta\zeta\beta J_0(sr) \end{bmatrix} e^{-\beta|z-z_*|\frac{s}{\beta}}ds \\
\psi_z &= \frac{M_0}{4\pi\rho\omega^2}e^{i\omega t}\int_0^\infty \begin{bmatrix} \cos 2\delta\sin\theta s J_1(sr) \\ +\sin 2\delta\zeta s J_1(sr) \end{bmatrix} e^{-\beta|z-z_*|\frac{s}{\beta}}ds
\end{aligned} \tag{3.17}$$

Referring to Fig 3.2 , strike-slip corresponds to the fault motion with the rake angle $\lambda = 0^\circ$, and dip-slip to $\lambda = 90^\circ$. Therefore, the fault motion with a rake

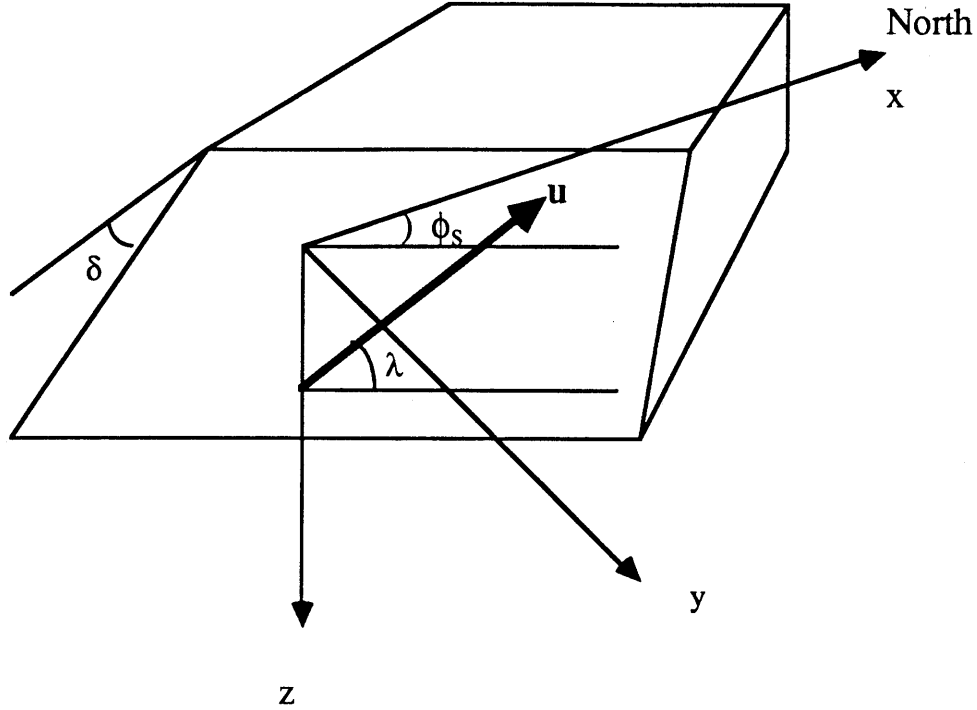


Figure 3.2: Definition of fault orientation parameters.

angle λ is a superposition of the potentials for strike-slip and dip-slip multiplied with $\cos \lambda$ and $\sin \lambda$, respectively. The strike angle can be incorporated easily in cylindrical coordinates by replacing the azimuthal angle θ by $\theta - \phi_s$.

It has been shown that the general shear fault motion in cylindrical coordinates can be formulated by simple coordinate transformation. Same procedure will be applied to tensile crack.

3.2.3 Tensile Crack

The tensile crack in Fig 3.1(a) is a superposition of three single couples. Since the cylindrical coordinates are used, the potential of a single couple in Fig 3.3(a) can be used to express the remaining two single couples by coordinate transfor-

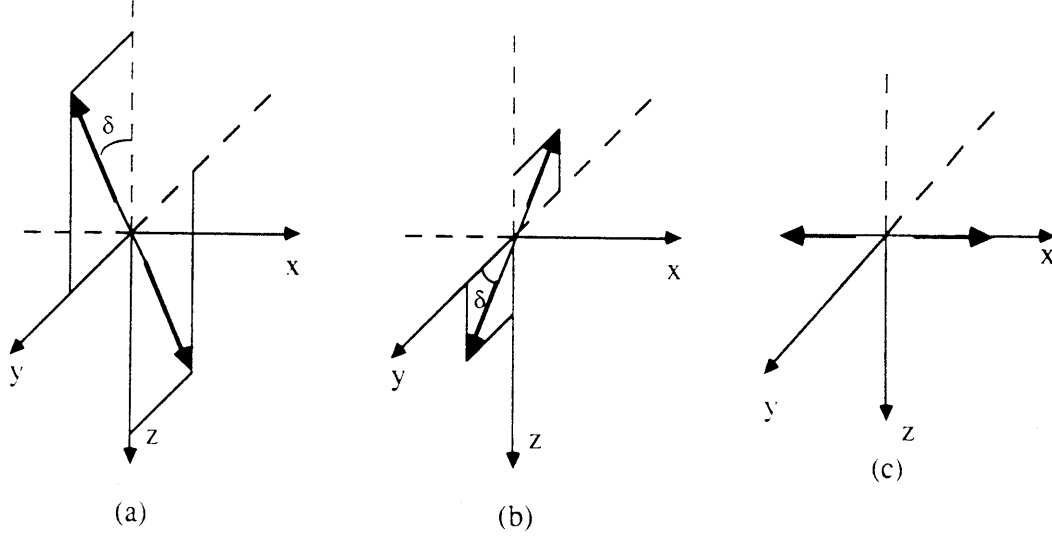


Figure 3.3: Single couples used to represent tensile crack with dip angle δ and strike angle $\phi_s = 0$, (a) (1,1) with $M_0 = 1$, (b) (2,2) with $M_0 = 1$, (c) (3,3) with $M_0 = \frac{\lambda+2\mu}{\lambda}$.

mation.

The potential of the second component is obtained by replacing δ in the potential of first single couple with $\delta + 90^\circ$. The third potential is obtained by rotating the first single couple in azimuthal angle 90° with $\delta = 90^\circ$. So that, the formulation of potential for tensile crack is

$$\begin{aligned}
 \phi &= \sum_{k=1}^3 \phi'(r, \theta_k, z; \delta_k, M_k) \\
 \psi_r &= \sum_{k=1}^3 \psi'_r(r, \theta_k, z; \delta_k, M_k) \\
 \psi_\theta &= \sum_{k=1}^3 \psi'_\theta(r, \theta_k, z; \delta_k, M_k) \\
 \psi_z &= \sum_{k=1}^3 \psi'_z(r, \theta_k, z; \delta_k, M_k) ,
 \end{aligned} \tag{3.18}$$

where the potentials for the first single couple (Fig 3.3(a) are

$$\begin{aligned}
\phi' &= -\frac{M_0 e^{i\omega t}}{4\pi\rho\omega^2} \int_0^\infty \begin{bmatrix} \{-0.25(s^2 - 2\alpha^2) \\ +0.25 \cos 2\delta (s^2 + 2\alpha^2)\} J_0(sr) \\ -\sin 2\delta \sin \theta \zeta \alpha s J_1(sr) \\ -0.25(1 - \cos 2\delta) \cos 2\theta s^2 J_2(sr) \end{bmatrix} e^{-\alpha|z-z_*|} \frac{s}{\alpha} ds \\
\psi'_r &= -\frac{M_0 e^{i\omega t}}{4\pi\rho\omega^2} \int_0^\infty \begin{bmatrix} -0.5 \sin 2\delta \sin \theta \zeta \beta J_0(sr) \\ +\{0.25(1 - \cos 2\delta s) \\ -0.25(1 - \cos 2\delta) \cos 2\theta s\} J_0(sr) \end{bmatrix} e^{-\beta|z-z_*|} \frac{s}{\beta} ds \\
\psi'_\theta &= -\frac{M_0 e^{i\omega t}}{4\pi\rho\omega^2} \int_0^\infty \begin{bmatrix} -0.5 \sin 2\delta \cos \theta \zeta \beta J_0(sr) \\ +0.25(1 - \cos 2\delta) \sin 2\theta s J_1(sr) \end{bmatrix} e^{-\beta|z-z_*|} \frac{s}{\beta} ds \\
\psi'_z &= \frac{M_0 e^{i\omega t}}{4\pi\rho\omega^2} e^{i\omega t} \int_0^\infty \begin{bmatrix} 0.5(1 + \cos 2\delta) \zeta \beta J_0(sr) \\ -0.5 \sin 2\delta \sin \theta s J_1(sr) \end{bmatrix} e^{-\beta|z-z_*|} \frac{s}{\beta} ds \quad (3.19)
\end{aligned}$$

and, the seismic moment $M_0 = \lambda A \bar{u}$, where A is the fault area and \bar{u} is the average normal displacement to the fault. The formulation for a tensile crack with an oblique strike angle is obtained by rotating the azimuthal angle by strike angle ϕ_s in the above equation. Since the particle displacement is normal to the fault surface in tensile crack, the rake angle can not be defined.

3.3 Global Matrix Approach

Next step is to find the unknown coefficients in Eq 3.6. Denoting the set of constraint variables for each Fourier order m as

$$\mathbf{F}^m(s, z) = \begin{Bmatrix} w^m(s, z) \\ u^m(s, z) + v^m(s, z) \\ u^m(s, z) - v^m(s, z) \\ \sigma_{zz}^m(s, z) \\ \sigma_{rz}^m(s, z) + \sigma_{\theta z}^m(s, z) \\ \sigma_{rz}^m(s, z) - \sigma_{\theta z}^m(s, z) \end{Bmatrix} \quad (3.20)$$

the boundary condition for welded contact at interface n separating layers n and $n + 1$ is

$$\mathbf{F}_n^m(s, z_n) + \tilde{\mathbf{F}}_n^m(s, z_n) - \mathbf{F}_{n+1}^m(s, 0) - \tilde{\mathbf{F}}_{n+1}^m(s, 0) = 0, \quad (3.21)$$

where subscript n denotes the layer number, z_n is the thickness of layer n , and the terms with tilde ‘ \sim ’ denotes source terms. Eq 3.21 gives a set of linear equations for each interface. These sets of equations for each interface, when combined, form a global matrix system, which is solved numerically. To be more specific, the boundary condition can be rewritten as

$$\mathbf{A}_{n,l} \mathbf{B}_n^m - \mathbf{A}_{n+1,u} \mathbf{B}_{n+1}^m = \mathbf{R}_{n+1,u}^m - \mathbf{R}_{n,l}^m, \quad (3.22)$$

where the coefficient matrix \mathbf{A} for upper interface is

$$\mathbf{A}_{n,u} = \begin{bmatrix} -\alpha & s & 0 & \alpha & s & 0 \\ -s & \beta & s & -s & -\beta & s \\ s & -\beta & s & s & \beta & s \\ (2s^2 - k^2)\mu & -2s\beta\mu & 0 & (2s^2 - k^2)\mu & 2s\beta\mu & 0 \\ 2s\alpha\mu & -(2s^2 - k^2)\mu & -s\beta\mu & -2s\alpha\mu & -(2s^2 - k^2)\mu & s\beta\mu \\ -2s\alpha\mu & (2s^2 - k^2)\mu & -s\beta\mu & 2s\alpha\mu & (2s^2 - k^2)\mu & s\beta\mu \end{bmatrix} \quad (3.23)$$

and the matrix for the lower interface is obtained by multiplying with the appropriate exponential matrix, i.e.

$$\mathbf{A}_{n,l}(s) = \mathbf{A}_{n,u}(s)\mathbf{I}_n(s) \quad (3.24)$$

where

$$\mathbf{I}_n(s) = \text{diag} \left\{ e^{-\alpha(s)z_n}, e^{-\beta(s)z_n}, e^{-\beta(s)z_n}, e^{\alpha(s)z_n}, e^{\beta(s)z_n}, e^{\beta(s)z_n} \right\}. \quad (3.25)$$

It is noted that the coefficient matrix is independent of Fourier order m , which is important for the efficiency of the numerical code since the multiple right hand side due to Fourier orders in global matrix can be solved simultaneously, as will be discussed in the next section 6.3. The unknown variables matrix in the potentials is

$$\mathbf{B}_n^m(s) = \left\{ a_{1,n}^m(s), b_{1,n}^m(s), c_{1,n}^m(s), a_{2,n}^m(s), b_{2,n}^m(s), c_{2,n}^m(s) \right\}^T. \quad (3.26)$$

The source matrices \mathbf{R}_n^m will be calculated from potentials using constitutive relations for displacements and stresses for different types of sources. The source matrix for tensile crack is given below and other source matrices are included in the appendix. The following source matrices are found from the potentials in Eq 3.18 using constitutive relations for displacements and stresses, which are found in Eq 3.11 and 3.7. For $\cos \theta$ and $\sin 2\theta$ Fourier orders, the source matrices

vanish. For order $m = 0$,

$$\mathbf{R}_n^0 = \sum_{k=1}^3 \frac{M_k}{4\pi\rho_n\omega^2} \left\{ \begin{array}{l} \{0.25\zeta(s^2 - 2\alpha^2) - 0.25\zeta \cos 2\delta_k(s^2 + 2\alpha^2)\} e^{-\alpha|z-z_*|} \\ + 0.25\zeta(1 + 3 \cos 2\delta_k s^2 e^{-\beta|z-z_*|} \\ 0.25 \frac{s}{\alpha} \{(s^2 - 2\alpha^2) - \cos 2\delta_k(s^2 + 2\alpha^2)\} e^{-\alpha|z-z_*|} \\ + 0.25(1 + 3 \cos 2\delta_k) \beta s e^{-\beta|z-z_*|} \\ - 0.25 \frac{s}{\alpha} \{(s^2 - 2\alpha^2) - \cos 2\delta_k(s^2 + 2\alpha^2)\} e^{-\alpha|z-z_*|} \\ - 0.25(1 + 3 \cos 2\delta_k) \beta s e^{-\beta|z-z_*|} \\ - 0.25 \mu \frac{s^2 + \beta^2}{s} \{(s^2 - 2\alpha^2) - \cos 2\delta_k(s^2 + \alpha^2)\} e^{-\alpha|z-z_*|} \\ - 0.5 \mu s^2 \beta (1 + 3 \cos 2\delta_k) e^{-\beta|z-z_*|} \\ - 0.5 \mu \zeta s \{(s^2 - 2\alpha^2) + \cos 2\delta_k(s^2 + 2\alpha^2)\} e^{-\alpha|z-z_*|} \\ - 0.25 \mu \zeta s (s^2 + \beta^2) (1 + 3 \cos 2\delta_k) e^{-\beta|z-z_*|} \\ + 0.5 \mu \zeta s \{(s^2 - 2\alpha^2) - \cos 2\delta_k(s^2 + 2\alpha^2)\} e^{-\alpha|z-z_*|} \\ + 0.25 \mu \zeta s (s^2 + \beta^2) (1 + 3 \cos 2\delta_k) e^{-\beta|z-z_*|} \end{array} \right\} \quad (3.27)$$

For $\sin \theta$ order,

$$\mathbf{R}_n^1 = \sum_{k=2}^3 \frac{M_k \sin 2\delta_k}{4\pi\rho_n\omega^2} \left\{ \begin{array}{l} \alpha s e^{-\alpha|z-z_*|} - 0.5(s^2 + \beta^2) \frac{s}{\beta} e^{-\beta|z-z_*|} \\ \zeta s^2 e^{-\alpha|z-z_*|} - \zeta s^2 e^{-\beta|z-z_*|} \\ - \zeta s^2 e^{-\alpha|z-z_*|} + \zeta \beta^2 e^{-\beta|z-z_*|} \\ - \mu \zeta s (s^2 + \beta^2) e^{-\alpha|z-z_*|} + \mu \zeta s (s^2 + \beta^2) e^{-\beta|z-z_*|} \\ - 2\mu \alpha s^2 e^{-\alpha|z-z_*|} + 0.5 \mu \frac{s^2}{\beta} (3\beta^2 + s^2) e^{-\beta|z-z_*|} \\ 2\mu \alpha s^2 e^{-\alpha|z-z_*|} - 0.5 \mu (\frac{s^4}{\beta} + s^2 \beta + 2\beta^3) e^{-\beta|z-z_*|} \end{array} \right\} \quad (3.28)$$

For $\cos 2\theta$ order,

$$\mathbf{R}_n^2 = \sum_{k=1}^3 \frac{M_k(1 - \cos 2\delta_k)}{4\pi\rho_n\omega^2} \left\{ \begin{array}{c} 0.25\zeta s^2 e^{-\alpha|z-z_*|} - 0.25\zeta s^2 e^{-\beta|z-z_*|} \\ 0.25\frac{s^3}{\alpha} e^{-\alpha|z-z_*|} - 0.25\frac{s^3}{\beta} e^{-\beta|z-z_*|} \\ -0.25\frac{s^3}{\alpha} e^{-\alpha|z-z_*|} - 0.25\frac{s^2-2\beta^2}{\beta} s e^{-\beta|z-z_*|} \\ -0.25\mu\frac{s^2}{\alpha}(s^2 + \beta^2)e^{-\alpha|z-z_*|} + 0.5\mu s^2\beta e^{-\beta|z-z_*|} \\ -0.5\mu\zeta s^3 e^{-\alpha|z-z_*|} + 0.5\mu\zeta s^3 e^{-\beta|z-z_*|} \\ 0.5\mu\zeta s^3 e^{-\alpha|z-z_*|} - 0.5\mu\zeta\beta^2 s e^{-\beta|z-z_*|} \end{array} \right\} \quad (3.29)$$

In the above matrices, M_k and δ_k are defined as

$$\begin{aligned} M_1 &= M_0, & \delta_1 &= 90^\circ, \\ M_2 &= M_0, & \delta_2 &= \delta + 90^\circ, \text{ and} \\ M_3 &= \frac{\lambda+2\mu}{\lambda} M_0, & \delta_3 &= \delta, \end{aligned}$$

except that $M_1 = -M_0$ when $m = 2$, $\cos 2\theta$ order. The by-product of the tensile crack formulation is an explosive source, where $M_k = M_0$, for $k = 1, 2, 3$. Consequently, only the zeroth Fourier order component is non-zero, yielding omnidirectional radiation.

The local matrix in Eq 3.21 for each interface has been formulated explicitly for the coefficient, unknown variables, and source matrices of tensile crack as an example. Since the boundary conditions should be satisfied at all the interfaces, the local matrices are combined to form a global matrix (Fig 3.4). Although the dimension of the global matrix is increased with the number of layers, it is noted that the maximum band width of the global matrix is limited to constant value 18 so that a special band matrix solver can be used to improve the numerical efficiency.

Once the unknown coefficients are found, the complete solution for each layer is found by performing inverse Hankel transform, summing over Fourier orders

Local system

$$A_{n,l}B_n^m - A_{n+1,u}B_{n+1}^m = R_{n+1,u}^m - R_{n,l}^m$$

Global system

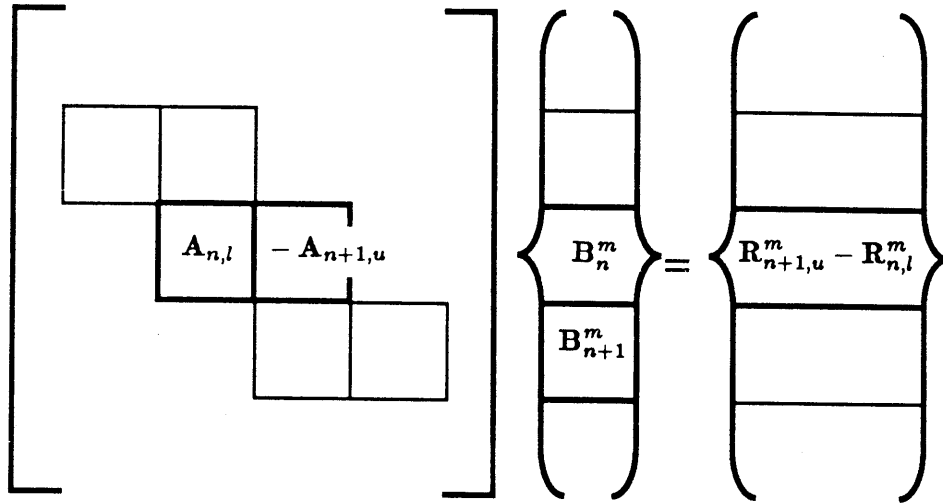


Figure 3.4: Mapping between local and global systems of equations (after Schmidt and Jensen, 1985).

for azimuthal angle, and Fourier synthesis in time domain, as will be discussed in the next section.

3.4 Field Representation in a Laterally Stratified medium

3.4.1 Complete Solution

From the global matrix solution, the complete solution in horizontal wave number domain combining homogeneous and particular solution is found for each discretized wave number. This complete solution in s -domain is called Hankel transform integrand for each m -th Fourier order, \mathbf{H}_n^m ,

$$\begin{aligned}\mathbf{H}_n^m(s, z_r) &= \mathbf{F}_n^m(s, z_r) + \tilde{\mathbf{F}}_n^m(s, z_r) \\ &= \mathbf{A}_n(s)\mathbf{B}_n^m(s, z_r) + \mathbf{R}_n^m(s, z_r) ,\end{aligned}\quad (3.30)$$

where the subscript n is the layer number in which the receiver at $z = z_r$ is located. Note that the integrand is not a function of r , but of the horizontal wave number s . In order to find the field parameters, inverse Hankel transform is performed on $\mathbf{H}_n^m(s, z_r)$,

$$\begin{aligned}\mathbf{H}_n^m(r, z_r) &= \int_0^\infty \mathbf{H}_n^m(s, z_r) s J_m(r, s) ds \\ &= \int_0^\infty \left\{ \underbrace{\mathbf{A}_n(s)\mathbf{B}_n^m(s, z_r)}_{\text{I}} + \underbrace{\mathbf{R}_n^m(s, z_r)}_{\text{II}} \right\} s J_m(r, s) ds .\end{aligned}\quad (3.31)$$

The first term I in Eq 3.31 is equivalent to the terms in the square bracket in Eq 3.7, while the second term II corresponds to Eq 3.27– 3.29 for tensile crack, except that they are now evaluated at the receiver depth $z = z_r$ instead of at the boundaries $z = z_n$. Once the field parameters of interest for Fourier order m in Eq 3.31 are found, the final solution is found from Eq 3.5 summing all the Fourier orders.

The procedure of obtaining the complete solution in real space ¹ has been explained in detail. Essentially, the solution technique is quite analytical, until the estimation of inverse Hankel transformation is introduced, which is done numerically. The numerical evaluation of the integrals is important to the efficiency of the developed code. Therefore, the aspects of numerical integration will be discussed in the next section.

3.4.2 Numerical Consideration

There are two numerical intensive steps in the solution technique, accompanied by numerical stability and efficiency problems. One is the numerical stability of the global matrix to be solved. This problem is treated in the previous publication [39], and the numerical stability is ensured unconditionally with proper scaling and arrangement of the coefficient matrix and partial pivoting when solving the global system of equation.

The other is the inverse Hankel transform, which is estimated numerically. The inverse Hankel transform can be basically estimated in two ways, FFT and direct numerical integration. The FFT method is an approximation to farfield with incident angle not so small, since the inverse Hankel transform is reduced to the form of Fourier transform for large argument of the Bessel function [12] [40]. The advantage of this method is the computational efficiency, since the reduced Fourier transform is computed through FFT so that the results are found at every range step simultaneously. The direct integration method, however, requires the calculation of Bessel function, and the integration scheme should be applied for each argument of the Bessel function. The advantage of integration method is the accurate estimation of the field including the near

¹to avoid confusion with the complete solution in horizontal wave number s -domain, i.e. before inverse Hankel transform.

field, although it is computationally extensive. Therefore, this method can be applied efficiently for the cases of a few receivers. While various techniques can be used to increase the efficiency of the numerical integration for special cases [2] [11] [19], the presently available methods in the code are FFT method and direct integration methods using Simpson rule or trapezoidal rule with Romberg scheme.

3.5 Numerical Examples

To demonstrate the solution technique, the radiation in a homogeneous unbounded medium from 3 different seismic sources are considered. These examples are chosen due to the simplicity, and the existence of the analytical solution available at least partially, for such as radiation pattern.

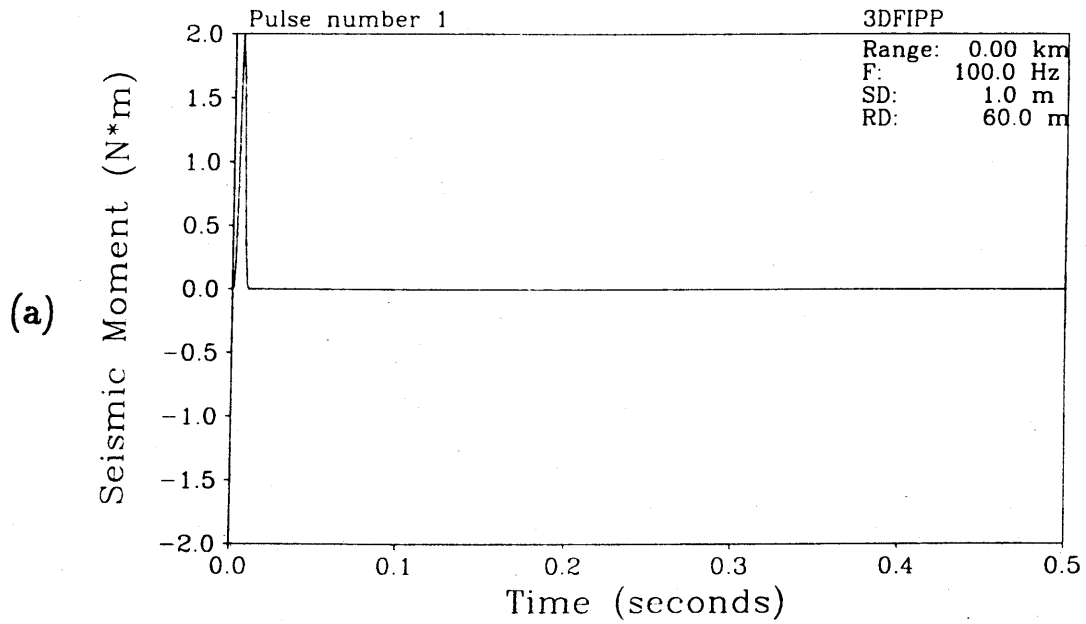
Case 3.1 *Tensile crack* : The tensile crack is compact and located at the origin with receivers at $z = 60 \text{ m}$ (Fig 3.6), giving the contour level of vertical displacement. The fault orientation parameters are $\delta = 90^\circ$ and $\phi_s = 0^\circ$. The source pulse to generate synthetic time series is given in Fig 3.5. Only the frequency components between 0 – 300 Hz are considered.

Case 3.2 *Dip-slip* : The source and environmental parameters are same as the case 3.2, except that the source is now dip-slip.

Case 3.3 *Strike-slip* : The source and environmental parameters are same as the case 3.2, except that the source is now strike-slip.

In order to characterize the radiation from different sources, two types of displays are used. One is the contour plot of a field parameter at certain depth,

SOURCE PULSE



SOURCE SPECTRUM

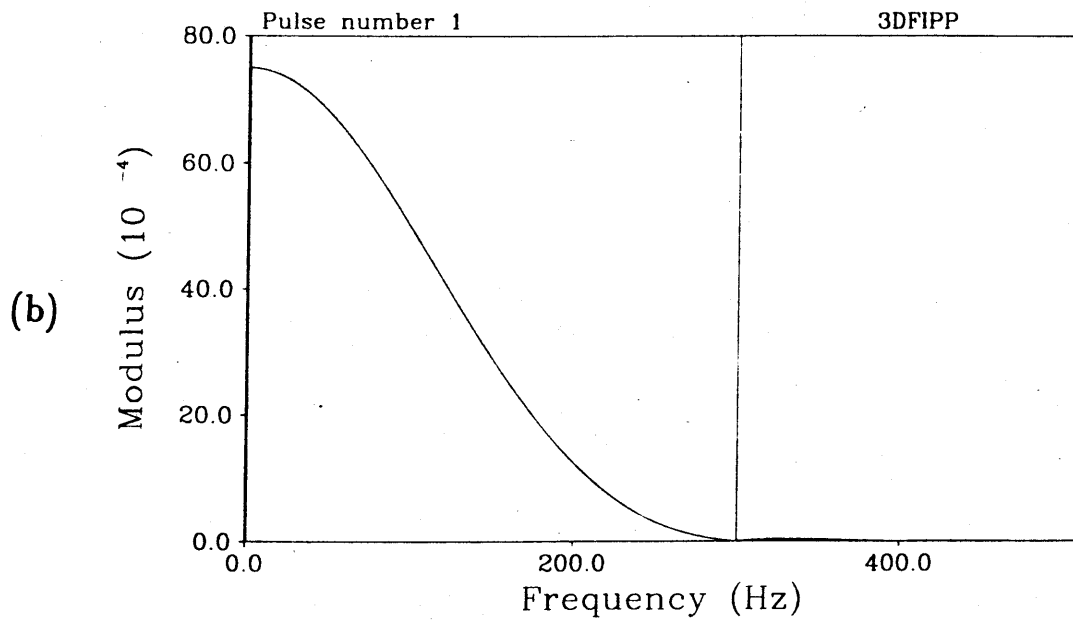


Figure 3.5: Source function (a) time series, (b) spectral shape.

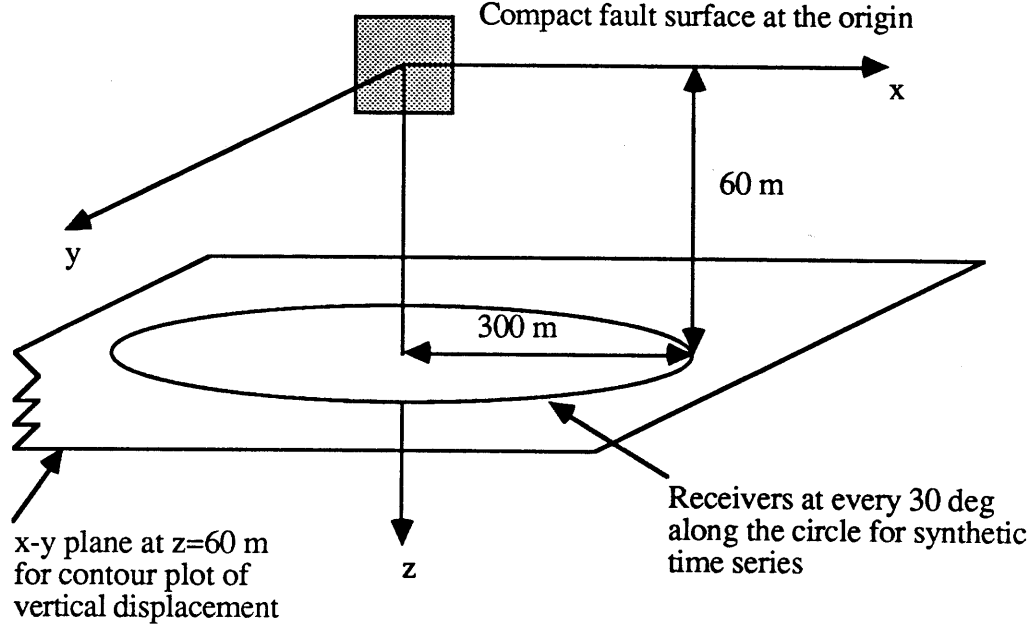


Figure 3.6: Sketch of coordinate system with source and receiver positions.

which shows the radiation pattern. The other is the synthesized time series for given source function. These are discussed subsequently.

The contour plot of vertical displacement at $z = 60 \text{ m}$ for frequency 100 Hz corresponding to tensile crack, dip-slip, and strike-slip sources at $z = 0 \text{ m}$ with dip angle $\delta = 90^\circ$ in a homogeneous elastic medium are given in Fig 3.7, 3.9, and 3.11, respectively. The contour level is taken to be

$$CL = 20 \log_{10} |w| \quad \text{re } 1 \text{ Pa} . \quad (3.32)$$

The source strength for the following examples is the unit seismic moment. As expected from the source matrices, the Fourier orders excited by a tensile crack are zeroth and second, $\cos 2\theta$ orders (Fig 3.7), while only first order is excited

to give dipolar radiation pattern in horizontal plane for dip-slip (Fig 3.9) and second order to give quadrupolar radiation pattern for strike-slip (Fig 3.11) . It is noted that the radiation patterns for different seismic sources are quite distinct for given receiver positions. However, the strike-slip can be obtained by rotating dip-slip in an homogeneous unbounded medium, which suggests the radiation pattern is obviously different depending on the receiver positions.

For the source time function in Fig 3.5, the synthetic seismograms for different types of sources are given in Fig 3.8, 3.10, and 3.12. The first arrival in Fig 3.8 for tensile crack is the compressional wave, and the second arrival is the shear wave. The amplitude of the compressional wave does vary slowly while the shear wave amplitude vanishes for horizontal angle 0 and π . This is due to the fact that the shear wave component of zeroth and second orders cancel each other at these directions. The seismogram in Fig 3.10 for dip-slip with dip angle $\delta = 90$ consists of only first Fourier order, as the radiation pattern (Fig 3.9) suggests. For this case, the shear component is dominant and the compressional component is barely seen. Also, it is noted that the phase between horizontal angle $0^\circ \leq \theta < 180^\circ$ are shifted by 180° giving negative phase. For strike-slip with dip angle $\delta = 90^\circ$ and strike angle $\phi_s = 0^\circ$, the second Fourier order is the only contribution as in Fig 3.11. Again phases are alternating every 90° . Therefore, it is argued that the temporal characteristics, as well as radiation patterns, of different sources can be used to identify the source parameters.

For above three cases in a homogeneous unbounded medium, the compressional and shear wave arrival times agree with simple calculation

$$t_c = \frac{\sqrt{r_r^2 + z_r^2}}{c_c} = 0.085 \text{ sec} \quad (3.33)$$

and

$$t_s = \frac{\sqrt{r_r^2 + z_r^2}}{c_s} = 0.170 \text{ sec}, \quad (3.34)$$

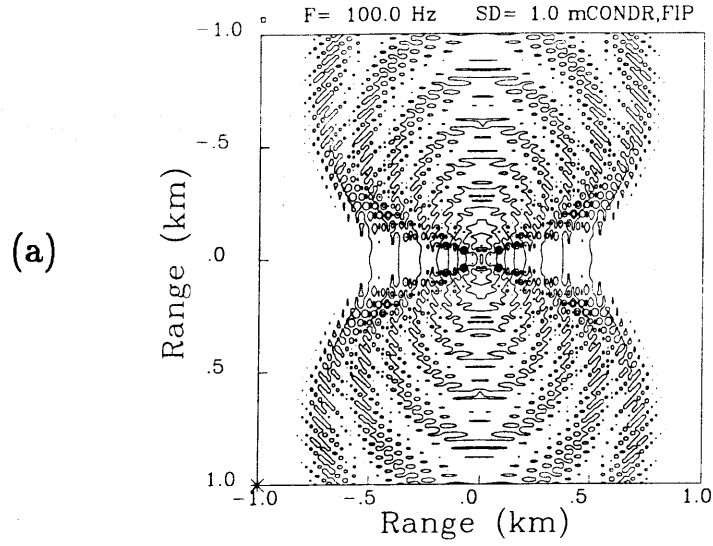


Figure 3.7: Radiation pattern of tensile crack with dip angle $\delta = 90^\circ$ for single frequency $f = 100$ Hz in a homogeneous elastic medium.

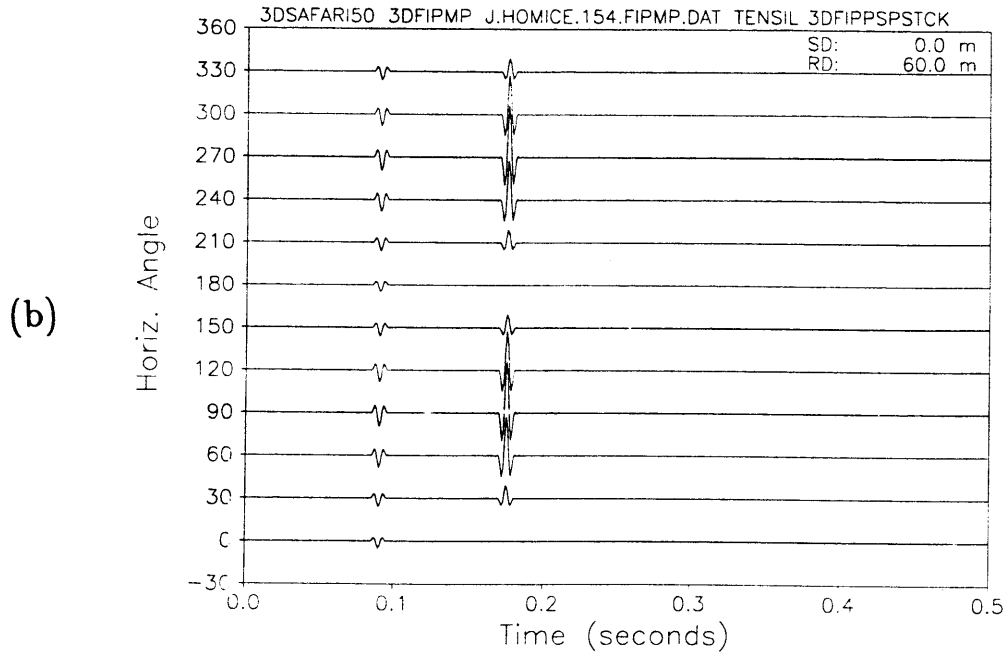


Figure 3.8: Seismogram for tensile crack with dip angle $\delta = 90^\circ$, receivers at $z = 0$ m, $r = 300$ m at every 30° in a homogeneous elastic medium.

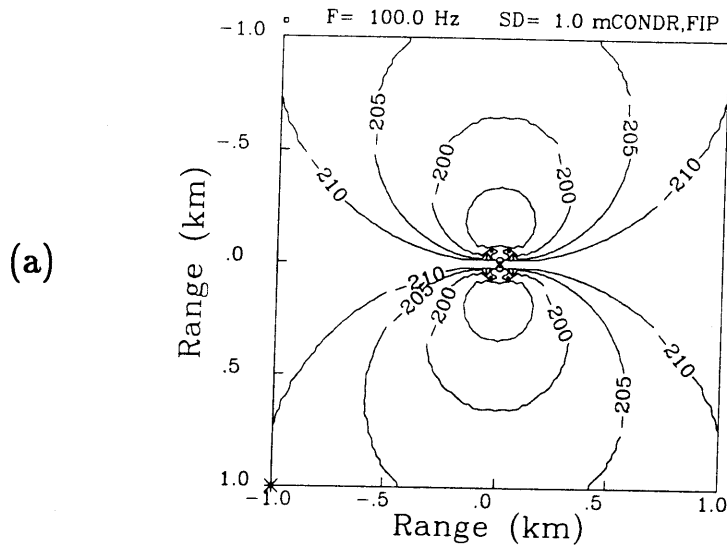


Figure 3.9: Radiation pattern of dip-slip with dip angle $\delta = 90^\circ$ for single frequency $f = 100$ Hz in a homogeneous elastic medium.

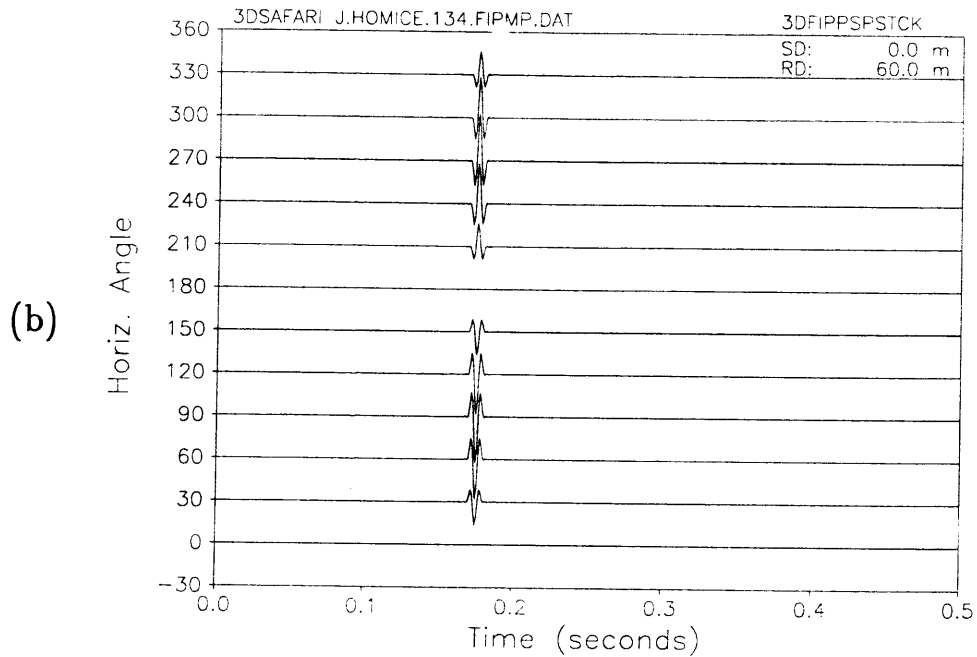


Figure 3.10: Seismogram for dip-slip with dip angle $\delta = 90^\circ$, receivers at $z = 0$ m, $r = 300$ m at every 30° in a homogeneous elastic medium.

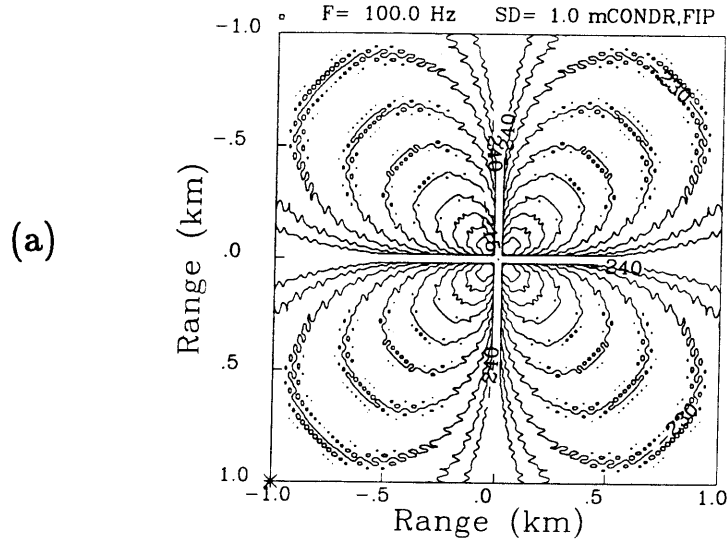


Figure 3.11: Radiation pattern of strike-slip with dip angle $\delta = 90^\circ$ for single frequency $f = 100$ Hz in a homogeneous elastic medium.

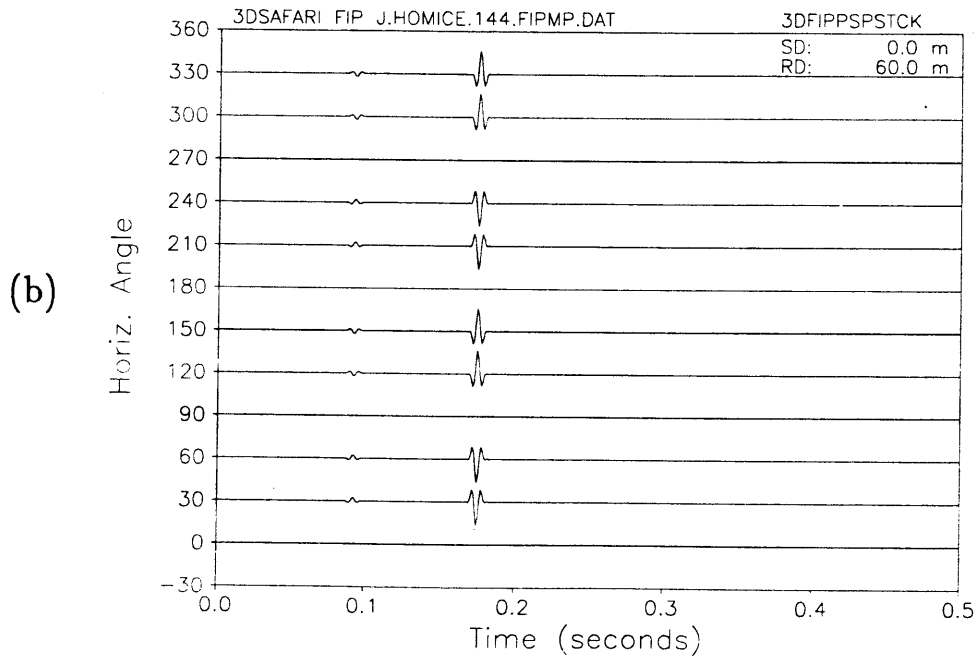


Figure 3.12: Seismogram for strike-slip with dip angle $\delta = 90^\circ$, receivers at $z = 0$ m, $r = 300$ m at every 30° in a homogeneous elastic medium.

where r_r and z_r are the coordinates of receiver location. For the cases considered, since the medium is unbounded, there is no dispersion of the existing waves. However, when there wave guides are introduced by boundaries as in the case of a floating ice plate in a central Arctic environment, the group velocity is different from the phase speed of corresponding waves. These cases are discussed in Chapter 6.

Chapter 4

Radiation from Propagating Cracks

The excitation by a seismic source originates on the dislocation surface. Often, the size of dislocation surface is approximately larger than a quarter of the wave length of interested frequency, causing directivity pattern, as has been observed in some earthquakes [17] . The directivity pattern is caused by the phase interference introduced by the geometry of crack surface, and crack propagation speed or, rupture speed in seismology. Obviously, when the seismic fault dimension is relatively small enough not to cause the phase interference, they can be treated as point or compact sources.

In Chapter 4.1, the solution to a canonical problem of non-compact crack radiation shows that the formulation of radiation pattern is actually the same as that of an array of sonic transducers. Therefore, the developed model can be also applied to the radiation from an array of sources as well as propagating cracks. In Chapter 4.2, an efficient numerical model is developed for the radiation and propagation from propagating cracks in a laterally stratified medium. In the numerical examples section, the same canonical problem is solved using

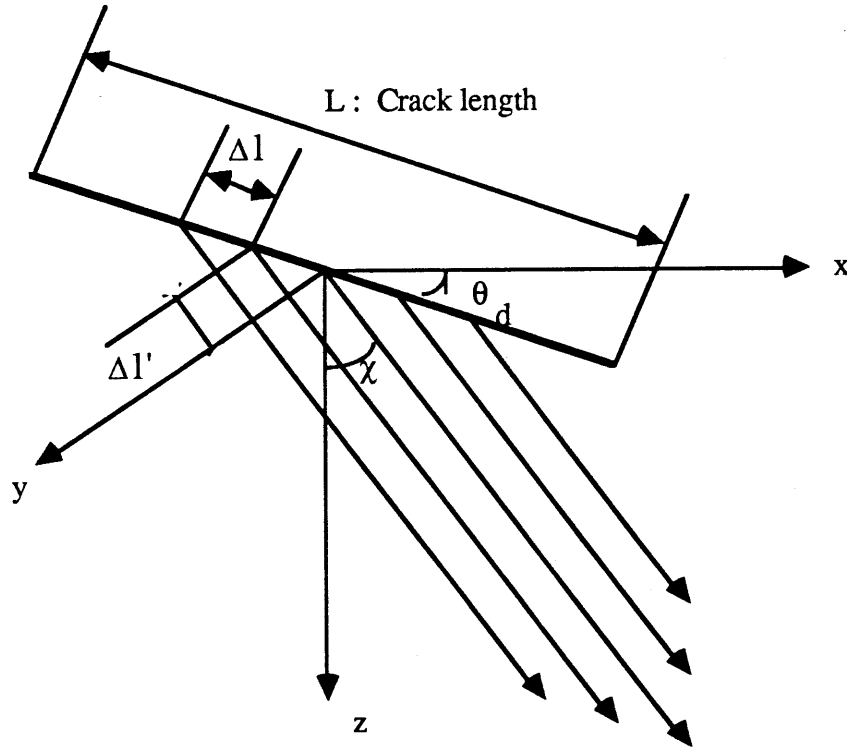


Figure 4.1: Discretized source distributed over the line crack and coordinate system.

the developed model, and the characteristics of radiated field from propagating cracks are discussed.

4.1 Analytic Solution to a Canonical Crack Radiation Problem

A canonical problem simulating the radiated field in an homogeneous unbounded acoustic medium can be analytically solved, giving insights for the radiation in

a laterally stratified elastic medium. The fault surface ¹ can be modeled as an array of discretized sound sources as in Fig 4.1, where a line crack is considered. The total pressure field with contributions from the sources can be expressed as

$$\begin{aligned}
p(\mathbf{x}, t) = & \frac{A \Delta l}{L r} \left[w_0\left(t - \frac{r}{c}\right) \right. \\
& + w_1\left(t - \frac{\Delta l}{c_v} + \frac{\Delta l'}{c} - \frac{r}{c}\right) + w_2\left(t + \frac{\Delta l}{c_v} - \frac{\Delta l'}{c} - \frac{r}{c}\right) \\
& + w_3\left(t - \frac{\Delta l}{c_v} + \frac{\Delta l'}{c} - \frac{r}{c}\right) + w_4\left(t + \frac{\Delta l}{c_v} - \frac{\Delta l'}{c} - \frac{r}{c}\right) \\
& \left. + \dots \right], \quad (4.1)
\end{aligned}$$

where $w_i(t)$ is the source function of the i -th discrete source, L is the crack length (array length), A is the source strength of an array, c_v is the crack propagation speed (phase velocity for an array), Δl is the distance between the discretized sources, and $\Delta l'$ is the distance between adjacent discrete sources to the receiver ($\Delta l' = \Delta l \sin \chi \cos(\theta - \theta_d)$). Assuming that each discrete source has the same source function, the pressure field can be written as

$$p(\mathbf{x}, t) = \frac{A \Delta l}{L r} \sum_{n=-N}^N w\left(\left(t - \frac{n \Delta l}{c_v}\right) - \frac{r - n \Delta l'}{c}\right). \quad (4.2)$$

As can be seen in the above equation 4.2, there are two phase terms introduced. The first term $n \Delta l / c_v$ is the time delay taken for the crack tip to travel the distance between discretized sources $n \Delta l$. The second term $-n \Delta l' / c$ is the time delay due to the different source location to the receiver positions. For the limiting case of $\Delta l \rightarrow 0$, i.e. for the continuously distributed sources, the expression in Eq 4.2 reduces to integral form

$$p(\mathbf{x}, t) = \frac{A}{L r} \int_{-L/2}^{L/2} w\left(t - r_a \left(\frac{1}{c_v} - \frac{\sin \chi \cos(\theta - \theta_d)}{c}\right) - \frac{r}{c}\right) dr_a. \quad (4.3)$$

¹Even if there can not exist a fault surface in an acoustic medium, the fault surface denotes the general surface over which the sources are distributed.

Defining

$$\Xi = \frac{1}{c_v} - \frac{\sin \chi \cos(\theta - \theta_d)}{c}, \quad (4.4)$$

the pressure expression can be written as

$$\begin{aligned} p(\mathbf{x}, t) &= \frac{A}{L} \frac{1}{r} \int_{-L/2}^{L/2} w\left(t - \Xi r_a - \frac{r}{c}\right) dr_a \\ &= \frac{A}{L} \frac{1}{r} \int_{-\infty}^{\infty} w\left(t - \Xi r_a - \frac{r}{c}\right) \text{rect}\left(\frac{L}{2}\right) dr_a, \end{aligned} \quad (4.5)$$

where the rectangular function $\text{rect}(\frac{L}{2})$ is defined as

$$\text{rect}\left(\frac{L}{2}\right) = \begin{cases} 1, & \text{when } |r_a| \leq \frac{L}{2} \\ 0, & \text{otherwise} \end{cases},$$

Using transformation, $\Xi r_a = \tau$,

$$\begin{aligned} p(\mathbf{x}, t) &= \frac{A}{L} \frac{1}{r} \int_{-L/2}^{L/2} w\left(t - \tau - \frac{r}{c}\right) \frac{1}{\Xi} \text{rect}\left(\frac{L}{2}\right) d\tau \\ &= \frac{A}{L} \frac{1}{r} w\left(t - \frac{r}{c}\right) * \frac{1}{\Xi} \text{rect}\left(\frac{L}{2}\right). \end{aligned} \quad (4.6)$$

The rectangular box is the result of uniform source strength distribution along the crack surface using farfield approximation. Of course, the source strength function does not have to be a box type, it can be a triangle, or any kind of shape that best describe the source strength distribution. Since the source distribution function is not known, the rectangular shape is assumed for simplicity.

From Eq 4.6, it is seen that the signal observed at the hydrophone is the source function convolved with the source distribution function, which is a function of $\Xi = \Xi(\theta_d, \chi, c_v)$ as shown in Eq 4.4, so that the observed signal will be different for different receiver directions. However, the area under the rectangular function remains constant for all the receiver directions.

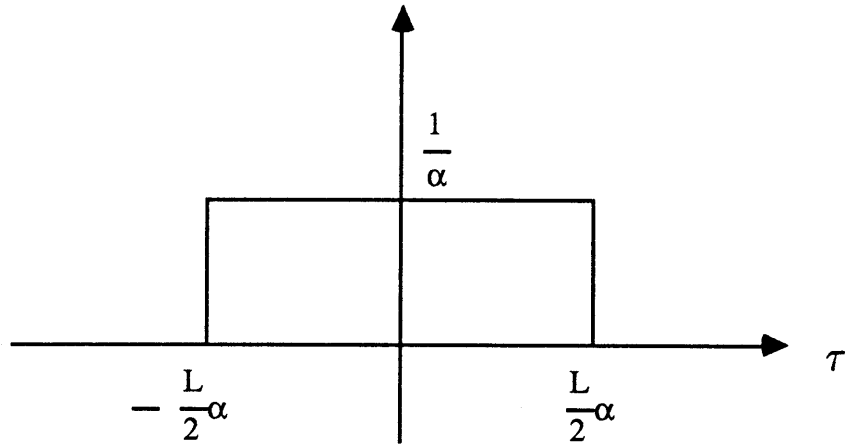
Since the convolution in time domain corresponds to the multiplication of two Fourier transforms in the frequency domain, it will be useful to look at the frequency domain solution. In order to find the frequency domain solution,

the impulse source function is assumed i.e. $w(t) = \delta(t)$. The plot of frequency domain solution is given in Fig 4.2 (b). The Fourier transform of a rectangular function is sinc function ($\text{sinc}(\tau) = \sin \tau / \tau$), so that the peaks and nulls as function of τ corresponds to the radiation pattern in the real space for certain range of τ , which is determined by the crack propagation speed and the ratio of wave length to the crack dimension. In fact, the formulation is exactly same as the radiation from the sonar, which makes the model applicable to the radiation from an array of transducers, such as airguns or explosions.

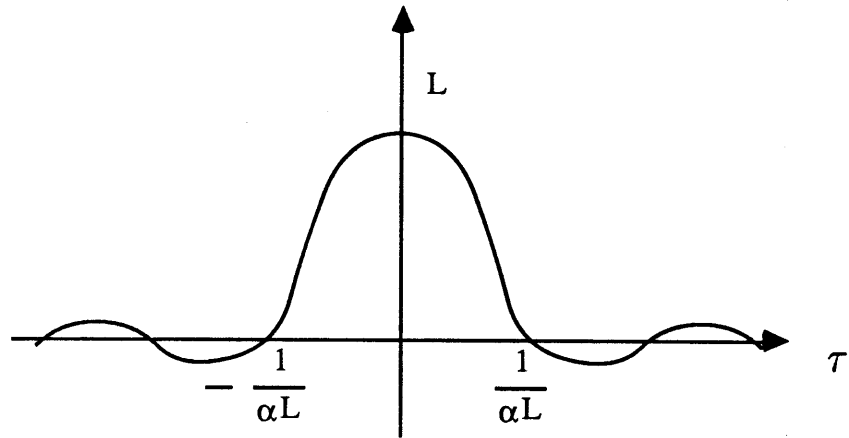
The interpretation of the results for this canonical problem gives useful information about the spectral and temporal radiation characteristics. First, the frequency domain solution shows that the spectral level at fixed receiver position (i.e. fixed Ξ) is different for different frequencies, which is called *frequency dependent directivity*. This is one of the characteristics that distinguishes the non-compact sources from compact sources. The time domain solution in Eq 4.6 shows the convolution of source signal with different duration of rectangular box depending on the receiver directions. These aspects of the frequency and time domain solutions are discussed in the numerical examples *Case 4.1*, where the same example is treated for a given source function using the presently developed code.

4.2 Numerical Model for Propagating Cracks in an Stratified Medium

The field caused by the moving crack can be basically found by integrating the proper Green's function of the specific sources over the fault surface. This method assumes that there is no scattering from the pre-existing crack surface,



(a)



(b)

Figure 4.2: Fourier transform pair, (a) rectangular source strength distribution function along the crack, (b) Fourier transform of $\frac{1}{\alpha}\text{rect}(r_a)$.

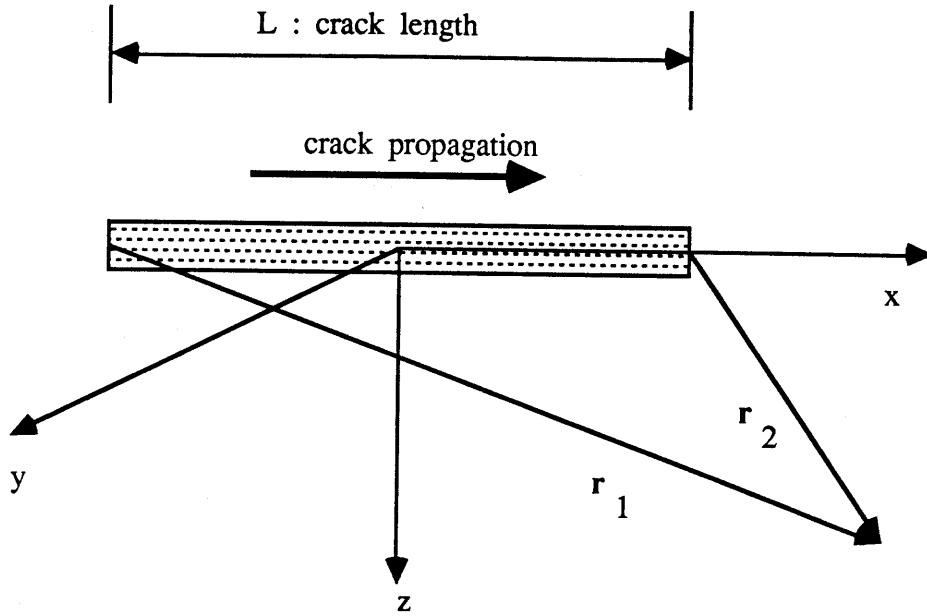
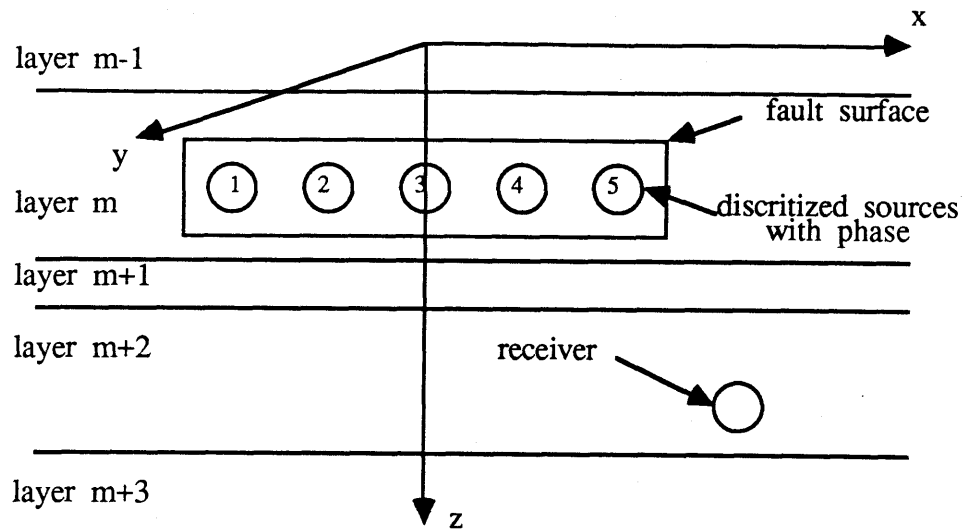


Figure 4.3: Sketch of moving crack.

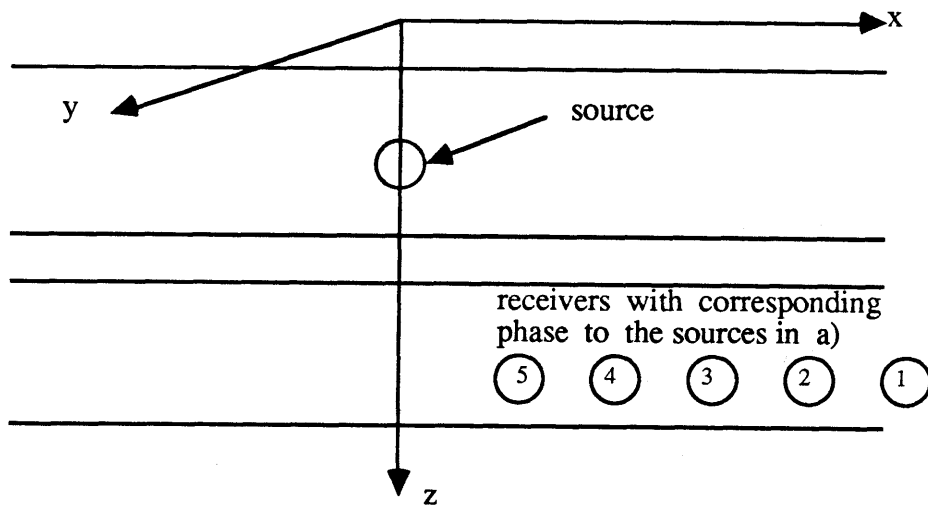
i.e. the distributed sources over the crack surface radiate as if the medium is homogeneous.

In order to treat the moving dislocation sources, it is necessary to place the sources off the z -axis in Fig 4.3 , which has been studied in earlier development of the three dimensional version of SAFARI code [38] . However, the mathematical treatment is rather complex and requires the calculation of higher orders of Bessel functions causing convergence problem and numerical inefficiency. Therefore, simple transformation of source and receiver position is used in this study. The actual problem of distributed sources over the fault surface is reduced to a numerical problem with one source on z -axis, and corresponding receivers for each of the sources (Fig 4.4).

The total radiation field due to moving crack can be obtained by summing the



a) source distribution over fault surface.



b) reduced numerical model.

Figure 4.4: Receiver-source position transformation (a) source distribution over fault surface, (b) reduced numerical model.

fields at receiver positions. In order to apply transform-superposition method, some considerations are needed. First, the Green's function of the source positioned on the z - axis has to be multiplied by a phase term due to traveling crack speed. The phase difference introduced by a propagating crack consists of two parts. One corresponds to the time delay for the crack to propagate from one source position to another, and the other is a time delay due to different source positions, as discussed in the previous section. Therefore, the total phase difference, for example (Fig 4.3), caused by different source positions, \mathbf{r}_1 and \mathbf{r}_2 , is

$$\tau_0 = \frac{L}{v_r} + \frac{|\mathbf{r}_2| - |\mathbf{r}_1|}{c} \quad (4.7)$$

The second term is included in receiver-source position transformation. The first term is a phase to be multiplied to the source Green's function. Secondly, when the field parameters are added, another transformation to correct the receiver-source transformation is necessary. This consideration is made to resolve the farfield approximation for the array, i.e. the following requirement for farfield approximation is not necessary

$$L \ll \sqrt{r^2 + z^2}, \quad (4.8)$$

of which restriction applies to the analytical solutions.

For the case of the multiple depth sources (Fig 4.5), the same procedure will be performed for each source depth. This is due to the fact that the geometry concerned is a laterally stratified medium, so that the source-receiver transformation can be applied to horizontal direction only.

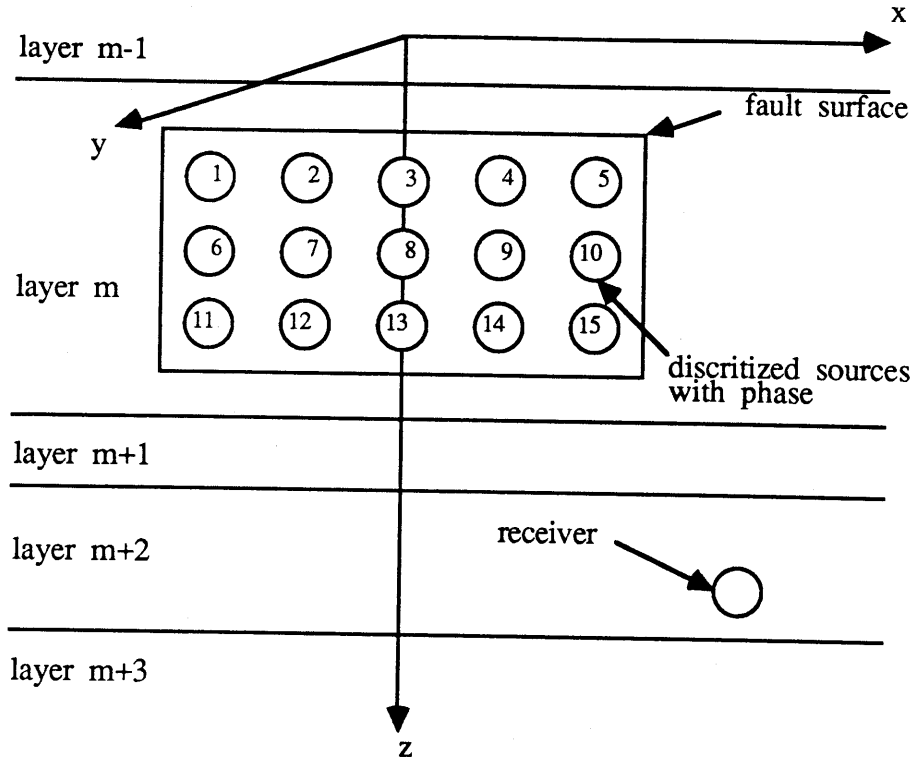


Figure 4.5: Two dimensional crack surface and source distribution.

4.3 Numerical Examples

Two canonical problems are considered in acoustic and elastic media. The media are homogeneous and unbounded, so that there is no boundary effect. This will allow us to look at the effects of non-compact sources. The source and receivers of examples are explained in the followings.

Case 4.1 *Radiation from an array in a homogeneous unbounded acoustic medium*

: The line array is extended from $(-25, 0, 0)$ to $(25, 0, 0)$ m , traveling at speed $c_v = 1800$ $m/sec.$, while the sound speed in the acoustic medium is $c = 1440$ $m/sec.$ The source type is explosive source (monopole). Refer to Fig 4.3.

Case 4.2 Radiation from a propagating crack in a homogeneous unbounded elastic medium : The crack is assumed to be a line crack with a element Green's function being a explosive source, extending from $(-25, 0, 0)$ to $(25, 0, 0)$ m. The crack travels at $c_v = 1800$ m/sec, and the compressional and shear speed of the medium are $c_c = 3500$ m/sec, $c_s = 1800$ m/sec, respectively.

Two types of displays are used to visualize the radiated field. For *Case 4.1*, the contour plot for xy -plane at $z = 60$ m (Refer to Fig 3.6) and the synthetic time series at range 300 m are given in Fig 4.6 and 4.7, respectively. In Fig 4.6, the major lobe direction θ_m due to steering, that is due to propagation speed, can be calculated simply by Snell's law,

$$\begin{aligned}\theta_m &= \sin^{-1} \left(\frac{c}{c_v} \right) \\ &= \sin^{-1} \left(\frac{1440}{1800} \right) = 53.13^\circ\end{aligned}\tag{4.9}$$

This major lobe corresponds to the peak of Sinc function in Fig 4.2 shifted by a corresponding phase due to crack propagation speed, or phase speed of an array. The synthetic time series in Fig 4.7 shows the major lobe effect in the direction at $\approx \pm 60^\circ$ on arrivals with high amplitude. When the higher frequencies with the same crack dimension are considered, the steering effect will become more obvious radiating the acoustic energy spatially in a narrower beam.

For *Case 4.2*, the elastic medium has two wave components, compressional and shear waves. However, since the source is omni-directional explosive source, the shear wave is not excited, which simplifies the problem ². The compressional wave speed is 3500 m/sec, which is greater than the crack propagation speed 1800 m/sec, called subsonic crack speed. For this case, the steering angle, or the major lobe direction θ_m can not be defined in real space, i.e. θ_m is imaginary

²The shear wave excited by directional sources is treated in Chapter 6

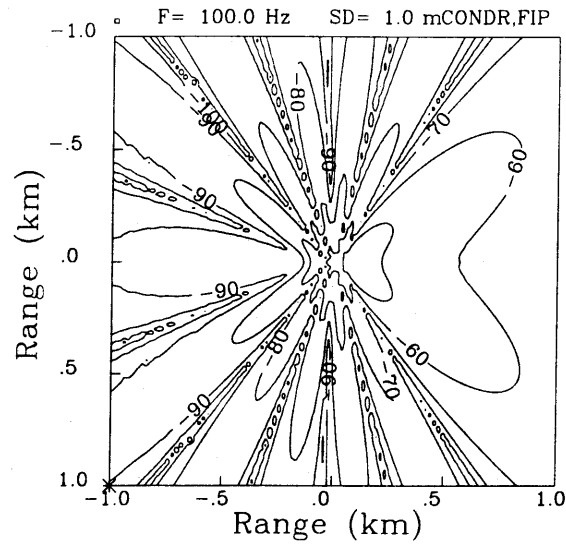


Figure 4.6: Radiation pattern for an array of explosive sources for a single frequency $f = 100$ Hz in a homogeneous acoustic medium.

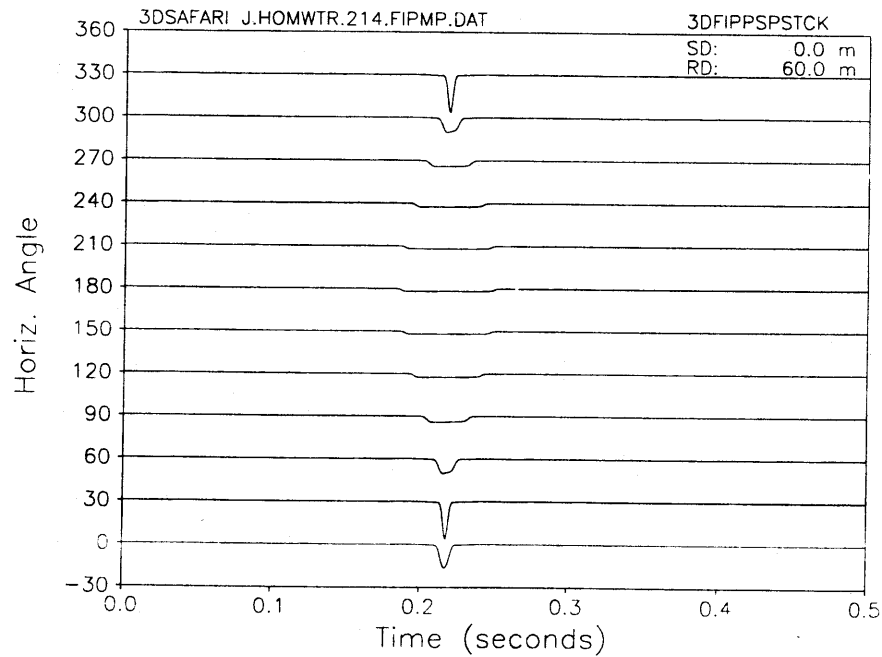


Figure 4.7: Seismogram of σ_{zz} for an array of explosive sources with receivers at $z = 60$ m, $r = 300$ m at every 30° in a homogeneous acoustic medium.

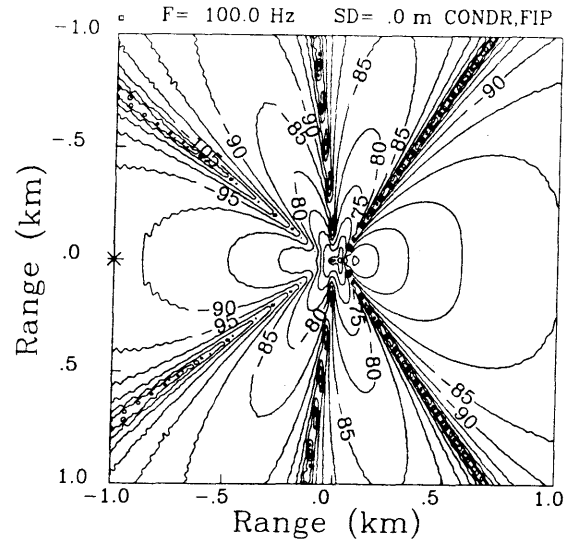


Figure 4.8: Radiation pattern for an array of explosive sources for a single frequency $f = 100$ Hz in a homogeneous elastic medium.

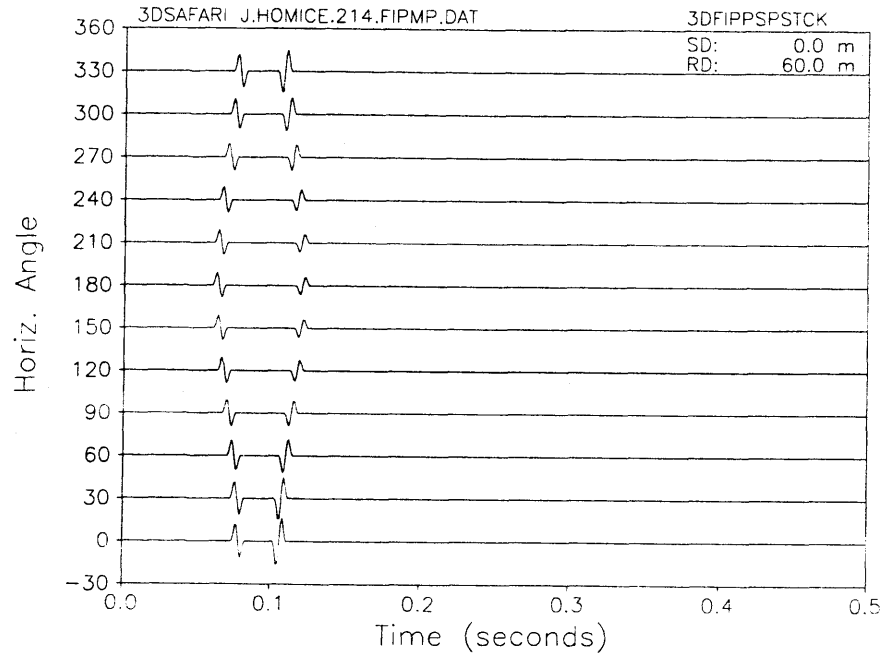


Figure 4.9: Seismogram of the vertical velocity for an array of explosive sources with receivers at $z = 60$ m, $r = 300$ m at every 30° in a homogeneous elastic medium.

in Eq 4.9. Therefore, the major lobe is not seen in Fig 4.8, and the directivity pattern is not as drastic as *Case 4.1* since the ratio of the compressional wave length to crack length is greater than the previous case. This effect is shown in Fig 4.9 with moderate changes in amplitude between channels compared to Fig 4.7, which means the beam is broader spatially.

Chapter 5

Transversely Isotropic Medium

In this Chapter, it is shown how the global matrix method can be applied to the formulation of propagation in a transversely isotropic medium. A transversely isotropic medium is characterized by five independent elastic constants. Often, the situation occurs when the periodically repeated finely layered sediment, or the sea and lake ice are considered.

Since the theory for the wave propagation in a transversely isotropic medium is well established [3] [13] [14] [15] [20] [26] [27] [28], the emphasis is given on the application of global matrix method to a transversely isotropic medium. First, the equation of motion is presented in cylindrical coordinates. The equation of motion is no longer expressed as a wave equation, as in the case of an isotropic medium. Then, the equivalent transversely isotropic elastic constants for periodically fine layered medium are summarized. By introducing intermediate functions, the decoupled equations are formulated for SH and $SV - P$ waves. These functions are utilized to express the boundary conditions at the interfaces in a form compatible with the isotropic case. It is noted that, in order to set up a system of linear equations, the intermediate functions need to be arranged as the potentials in an isotropic medium, which is discussed in Section 5.4.

5.1 Equation of Motion

The equation of motion in cylindrical coordinates is [43, pp.219]

$$\rho \frac{\partial^2 \mathbf{u}}{\partial t^2} = \rho \mathbf{F} + (\text{div } \sigma_r, \text{div } \sigma_\theta, \text{div } \sigma_z) + \frac{1}{r}(-\sigma_{\phi\phi}, \sigma_{r\phi}, 0). \quad (5.1)$$

For an isotropic medium, the above equation 5.1 reduces to Eq 2.8 using the stress-strain relationship with two independent elastic constants λ and μ . In the following sections, the general equation of motion 5.1 will be further simplified for a transversely isotropic medium to a system of equations with the five independent elastic constants, which decouples for $P - SV$ and SH waves by introducing a set of proper intermediate functions, \mathbf{f} .

5.2 Stress-Strain Relation

The stress-strain relation in cylindrical coordinates is

$$\begin{Bmatrix} \sigma_{rr} \\ \sigma_{\phi\phi} \\ \sigma_{zz} \\ \sigma_{\phi z} \\ \sigma_{zr} \\ \sigma_{r\phi} \end{Bmatrix} = \begin{bmatrix} C_{11} & C_{12} & C_{13} & 0 & 0 & 0 \\ C_{12} & C_{11} & C_{13} & 0 & 0 & 0 \\ C_{13} & C_{13} & C_{33} & 0 & 0 & 0 \\ 0 & 0 & 0 & 2C_{44} & 0 & 0 \\ 0 & 0 & 0 & 0 & 2C_{44} & 0 \\ 0 & 0 & 0 & 0 & 0 & 2C_{66} \end{bmatrix} \begin{Bmatrix} \epsilon_{rr} \\ \epsilon_{\phi\phi} \\ \epsilon_{zz} \\ \epsilon_{\phi z} \\ \epsilon_{zr} \\ \epsilon_{r\phi} \end{Bmatrix} \quad (5.2)$$

where $C_{12} = C_{11} - 2C_{66}$. The expressions for strain in cylindrical coordinates are

$$\begin{aligned} \epsilon_{rr} &= \frac{\partial u_r}{\partial r}, \quad \epsilon_{\phi\phi} = \frac{1}{r} \frac{\partial u_\phi}{\partial \phi} + \frac{1}{r} u_r, \quad \epsilon_{zz} = \frac{\partial u_z}{\partial z}, \\ \epsilon_{\phi z} &= \frac{1}{r} \frac{\partial u_z}{\partial \phi}, \quad \epsilon_{zr} = \frac{\partial u_r}{\partial z} + \frac{\partial u_z}{\partial r}, \\ \epsilon_{r\phi} &= \frac{\partial u_\phi}{\partial r} - \frac{1}{r} u_\phi + \frac{1}{r} \frac{\partial u_r}{\partial \phi} \end{aligned} \quad (5.3)$$

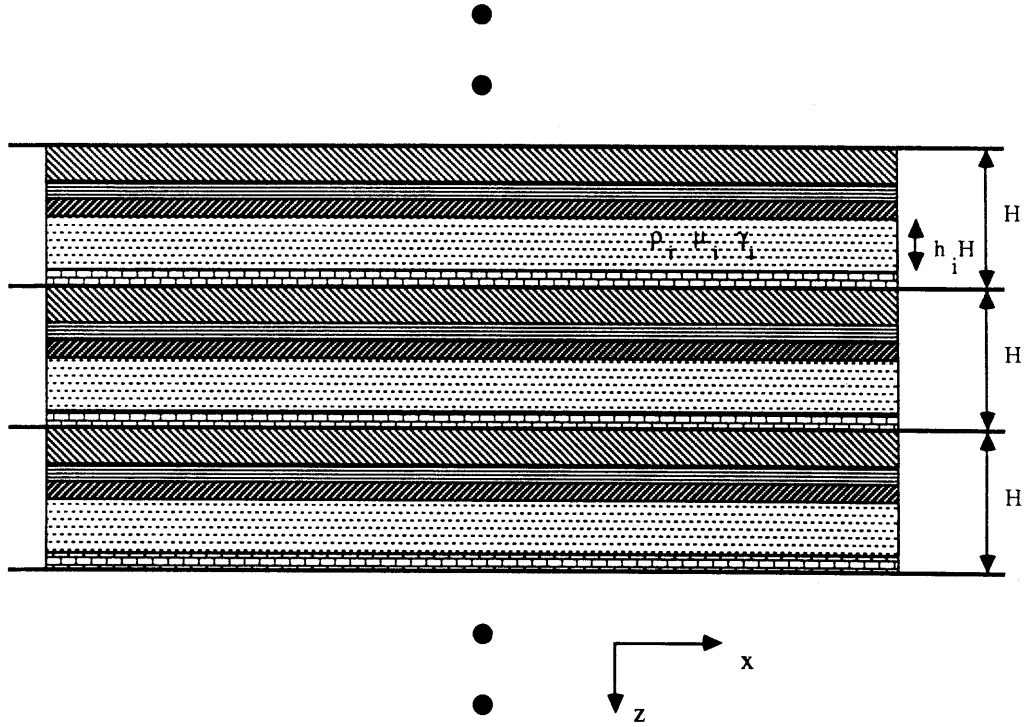


Figure 5.1: Sketch of a periodically finely layered medium.

of which general relation in curvilinear coordinates are found in Takeuchi and Saito [43]. For an isotropic medium, the stress-strain relation can be found by substituting $C_{11} = C_{33} = \lambda + 2\mu$, $C_{44} = C_{66} = \mu$, and $C_{12} = C_{13} = \lambda$.

5.3 Equivalent Transversely Isotropic Elastic Constants for Periodically Fine Layered Medium

The periodic finely layered medium described in Fig 5.1, when H is much smaller than the wave length of the interested frequency, can be treated as an equivalent homogeneous transversely isotropic medium. Consequently, the equivalent elastic constants for a periodically finely layered medium with N homogeneous

layers (Fig 5.1) may be shown to be

$$\begin{aligned}
C_{44} &= \langle \mu^{-1} \rangle^{-1} \\
C_{66} &= \langle \mu \rangle \\
C_{33} &= \langle \gamma / \mu \rangle^{-1} \\
C_{13} &= (1 - 2\langle \gamma \rangle) \langle \gamma / \mu \rangle^{-1} \\
C_{11} &= 4\langle \mu \rangle - 4\langle \gamma \mu \rangle + (1 - 2\langle \gamma \rangle)^2 \langle \gamma / \mu \rangle^{-1} \\
C_{12} &= C_{11} - 2\langle \mu \rangle = C_{11} - 2C_{66} ,
\end{aligned} \tag{5.4}$$

where the angled bracket denotes the thickness-weighted average [41].

5.4 Decoupled Equations for SH and P-SV Waves

Returning to solving the equation of motion, Eq 5.1 can be reduced to the equation with respect to displacement \mathbf{u} , first using stress-strain relation and then, using strain-displacement relation as in Eq 5.2. While the three displacement potentials, ϕ , Λ , and ψ , defined in Eq 3.6 and 3.4, that express the P , SV , and SH waves respectively, can be defined in an isotropic medium, the potentials cannot be defined for the equation of motion in an transversely isotropic medium since the $P - SV$ waves cannot be separated. However, a set of intermediate functions, f_1, f_2, f_3 , and f_4 , which combines the $P - SV$ waves and f_5 and f_6 for the SH wave, may be defined, since the $P - SV$ and SH waves still decouple. Therefore, the problems for $P - SV$ and SH waves are solved separately.

In cylindrical coordinates, the solution to the propagation of $P - SV$ waves may be assumed as

$$\begin{aligned}
w &= f_2(z; \omega, s) Y_k^m e^{i\omega t} \\
u &= f_1(z; \omega, s) \frac{1}{sr} \frac{\partial Y_k^m}{\partial \theta} e^{i\omega t} \\
v &= f_1(z; \omega, s) \frac{1}{s} \frac{\partial Y_k^m}{\partial r} e^{i\omega t}
\end{aligned}$$

$$\begin{aligned}
\sigma_{zz} &= f_3 Y_k^m(r, \theta) \\
\sigma_{zr} &= f_4 \frac{1}{s} \frac{\partial Y_k^m}{\partial r} \\
\sigma_{z\theta} &= f_4 \frac{1}{sr} \frac{\partial Y_k^m}{\partial \theta},
\end{aligned} \tag{5.5}$$

where Y_k^m is defined as

$$Y_k^m = J_m \begin{bmatrix} \cos m\theta \\ \sin m\theta \end{bmatrix}. \tag{5.6}$$

For the SH wave, the solution assumes the following forms,

$$\begin{aligned}
w &= 0 \\
u &= f_5(z; \omega, s) \frac{1}{sr} \frac{\partial Y_k^m}{\partial \theta} e^{i\omega t} \\
v &= -f_5(z; \omega, s) \frac{1}{s} \frac{\partial Y_k^m}{\partial r} e^{i\omega t} \\
\sigma_{zz} &= 0 \\
\sigma_{zr} &= f_6 \frac{1}{s} \frac{\partial Y_k^m}{\partial r} \\
\sigma_{z\theta} &= f_6 \frac{1}{sr} \frac{\partial Y_k^m}{\partial \theta},
\end{aligned} \tag{5.7}$$

where Y_k^m in f_5 and f_6 is defined as

$$Y_k^m = J_m \begin{bmatrix} \sin m\theta \\ -\cos m\theta \end{bmatrix}. \tag{5.8}$$

Comparing Eq 5.8 with 5.6, the different arrangements of Fourier orders for the $SV - P$ and SH waves are similar to those defined in Eq 3.4 in an isotropic medium¹. Obviously, this is to enable the boundary conditions to be compatible with the previous formulation in the isotropic medium. Substituting these

¹The major difference is that the potentials for the isotropic medium represent the P , SV , and SH waves fully separated, while the intermediate functions for the transversely isotropic medium represent the coupled $P - SV$ waves and decoupled SH wave.

equations into the equations of motion, it can be shown that

$$\begin{aligned}
\frac{df_1}{dz} &= -sf_2 + \frac{1}{L}f_4 \\
\frac{df_2}{dz} &= \frac{kF}{C}f_1 + \frac{1}{C}f_3 \\
\frac{df_3}{dz} &= -\rho\omega^2 f_2 + sf_4 \\
\frac{df_4}{dz} &= [s^2(A - \frac{F^2}{C}) - \rho\omega^2]f_2 - \frac{sF}{C}f_3 \\
\frac{df_5}{dz} &= \frac{1}{L}f_6 \\
\frac{df_6}{dz} &= (s^2N - \rho\omega^2)f_5.
\end{aligned} \tag{5.9}$$

The above equations are taken from the references [43] [29], and rearranged to be compatible with global matrix method. As can be seen in the above Eq 5.9, f_i , for $i = 1, \dots, 4$ are decoupled from f_i , for $i = 5, 6$. The eigenvalues for the first 4 equations can be found from

$$\nu^4 - \left[\frac{k^2 A - \rho\omega^2}{L} + \frac{k^2 L - \rho\omega^2}{C} - \frac{k^2 (F + L)^2}{CL} \right] \nu^2 + \frac{(k^2 L - \rho\omega^2)(k^2 A - \rho\omega^2)}{CL} = 0 \tag{5.10}$$

The four eigenvalues represent the up-going and down-going components of quasi- P and quasi- SV waves. The two eigenvalues obtained from

$$\nu^2 = \frac{Nk^2 - \rho\omega^2}{L} \tag{5.11}$$

represent the up-going and down-going components of the SH wave. In the isotropic case, ν_1 and ν_2 corresponds to α and β , which are the vertical wave numbers for compressional and shear waves, respectively. And, ν_3 corresponds to β since the SH wave has the same wave number as the SV wave in an isotropic medium.

In Eq 5.10 and 5.11, considering the vertical wave number $\nu \rightarrow 0$, in which case the waves travel in the horizontal direction, the phase speeds are found to

be $\sqrt{C_{11}/\rho}$ for P wave and $\sqrt{C_{44}/\rho}$ for SV wave, and $\sqrt{C_{66}/\rho}$ for SH wave, respectively. Now, considering $k \rightarrow 0$, in which the waves propagate in the vertical direction, the phase speeds are $\sqrt{C_{33}/\rho}$ for the compressional wave P , and $\sqrt{C_{44}/\rho}$ for the shear waves, SV and SH .

Once, the eigenvalues and eigenvectors are found, the homogeneous solution to Eq 5.9 can be written

$$\mathbf{f} = \mathbf{E}\mathbf{\Lambda}\mathbf{K}, \quad (5.12)$$

where \mathbf{E} is the eigenvector matrix of Eq 5.9, $\mathbf{\Lambda}$ is a diagonal matrix for eigenvalues, and \mathbf{K} is a unknown coefficient matrix for six components of up-going and down-going P , SV , and SH waves, respectively. They are written as follows,

$$\mathbf{E} = \begin{bmatrix} 1 & 1 & 0 & 1 & 1 & 0 \\ -\gamma_1 & -\gamma_2 & 0 & \gamma_1 & \gamma_2 & 0 \\ X_1 & X_2 & 0 & X_1 & X_2 & 0 \\ -Y_1 & -Y_2 & 0 & Y_1 & Y_2 & 0 \\ 0 & 0 & 1 & 0 & 0 & 1 \\ 0 & 0 & -C_{44}\nu_3 & 0 & 0 & C_{44}\nu_3 \end{bmatrix} \quad (5.13)$$

$$\mathbf{\Lambda} = \text{diag} \{ e^{-\nu_1 z}, e^{-\nu_2 z}, e^{-\nu_3 z}, e^{\nu_1 z}, e^{\nu_2 z}, e^{\nu_3 z} \} \quad (5.14)$$

$$\mathbf{K} = \{ a_1^m, b_1^m, c_1^m, a_2^m, b_2^m, c_2^m \}^T, \quad (5.15)$$

where γ_i , X_i , and Y_i are defined as

$$\begin{aligned} \gamma_i &= \frac{k\nu_i(C_{13} + C_{44})}{\rho\omega^2 - k^2C_{44} + \nu_i^2C_{33}} \\ X_i &= C_{33}\nu_i\gamma_i - kC_{13} \\ Y_i &= C_{44}(\nu_i + k\gamma_i). \end{aligned} \quad (5.16)$$

It is noted that $\mathbf{\Lambda}$, \mathbf{K} and \mathbf{E} correspond to \mathbf{I} , \mathbf{B} and \mathbf{A} for the isotropic case in Eq 3.25, 3.26, and 3.23, respectively. As in the case in the isotropic medium,

the \mathbf{E} matrix is independent of Fourier order m , while the unknown coefficient matrix \mathbf{K} has to be found for each orders of m . However, note that the \mathbf{f} matrix is an intermediate set of functions like potentials in the isotropic medium. In the next Section, the intermediate functions are combined to represent the boundary conditions used in the interface in the global matrix method.

5.5 Formulation of Boundary Conditions Compatible with Global Matrix Method

The boundary conditions at the interfaces (Eq 3.20) are formulated based on Eq 5.12, which is a form of homogeneous solution in a transversely isotropic medium.

$$\begin{aligned}
w^m(r, z) &= \int_0^\infty f_2 s J_m(rs) ds \\
u^m(r, z) + v^m(r, z) &= \int_0^\infty (-f_1 + f_5) s J_{m+1}(rs) ds \\
u^m(r, z) - v^m(r, z) &= \int_0^\infty (f_1 + f_5) s J_{m-1}(rs) ds \\
\sigma_{zz}^m(r, z) &= \int_0^\infty f_3 s J_m(rs) ds \\
\sigma_{rz}^m(r, z) + \sigma_{z\phi}(r, z) &= \int_0^\infty (-f_4 + f_6) s J_{m+1}(rs) ds \\
\sigma_{rz}^m(r, z) - \sigma_{z\phi}(r, z) &= \int_0^\infty (f_4 + f_6) s J_{m-1}(rs) ds.
\end{aligned} \tag{5.17}$$

where the explicit expression for \mathbf{f} can be calculated from Eq 5.12

$$\begin{Bmatrix} f_1 \\ f_2 \\ f_3 \\ f_4 \\ f_5 \\ f_6 \end{Bmatrix} = \begin{bmatrix} 1 & 1 & 0 & 1 & 1 & 0 \\ -\gamma_1 & -\gamma_2 & 0 & \gamma_1 & \gamma_2 & 0 \\ X_1 & X_2 & 0 & X_1 & X_2 & 0 \\ -Y_1 & -Y_2 & 0 & Y_1 & Y_2 & 0 \\ 0 & 0 & 1 & 0 & 0 & 1 \\ 0 & 0 & -C_{44}\nu_3 & 0 & 0 & C_{44}\nu_3 \end{bmatrix} \begin{Bmatrix} a_1^m(s) e^{-z\nu_1(s)} \\ b_1^m(s) e^{-z\nu_2(s)} \\ c_1^m(s) e^{-z\nu_3(s)} \\ a_2^m(s) e^{z\nu_1(s)} \\ b_2^m(s) e^{z\nu_2(s)} \\ c_2^m(s) e^{z\nu_3(s)} \end{Bmatrix} \tag{5.18}$$

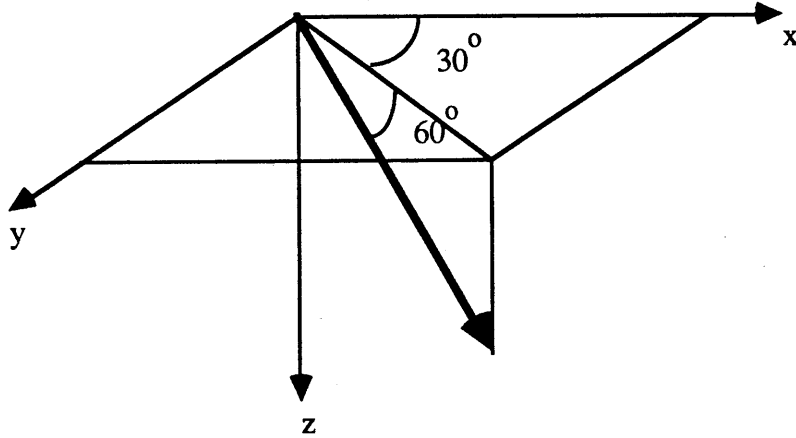


Figure 5.2: A single force as a source.

In the implementation of the numerical code, the eigenvectors are scaled in the same way as the coefficient matrix \mathbf{A} in Eq 3.23 for the isotropic medium for compatibility.

5.6 Numerical Examples

One of the most characteristic features of the wave propagation in transversely isotropic medium is the separation of the SH and SV waves depending on the direction of propagation. The separation is maximized generally for the propagation in the horizontal direction, as can be seen in the slowness diagram in Fig 5.3 which has been computed for the *Case 5.1*. In order to see the separation, the source needs to excite the SH wave, of which sources include

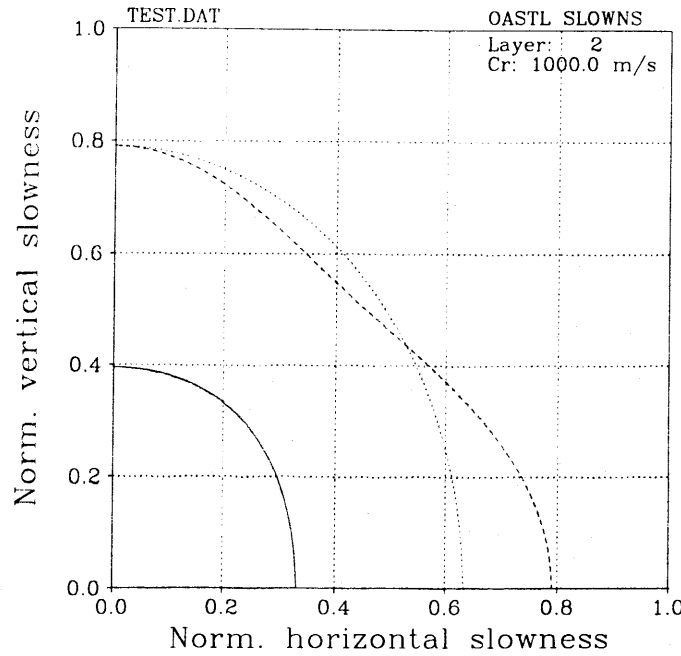


Figure 5.3: Slowness surface of P (solid line), SV (dotted line), and SH (dashed line) waves for case 1.

forces, or couples with Fourier orders greater than the zero-th. For simplicity, a single force in an unbounded and homogeneous medium ² is considered in the following examples.

Case 5.1 Transversely isotropic medium : The transversely isotropic medium considered consists of two isotropic layers, which are repeatedly fine layered. For the first and second layer, the compressional wave speeds are 4000 and 2000 m/sec , and the shear speeds 2000 and 1000 m/sec , respectively. The density are 1 g/cm^3 for both layers. The point force is placed at the origin and the direction of the force is to the horizontal angle 30° , and the vertical angle is

²Since the presently developed codes can not have a source in the anisotropic medium, an infinitesimally thin isotropic layer is placed at the depth of source.

60° towards the z -axis as shown in Fig 5.2. The 12 receivers are placed at every 30° at depth of 60 m and range of 300 m , as in Fig 3.6.

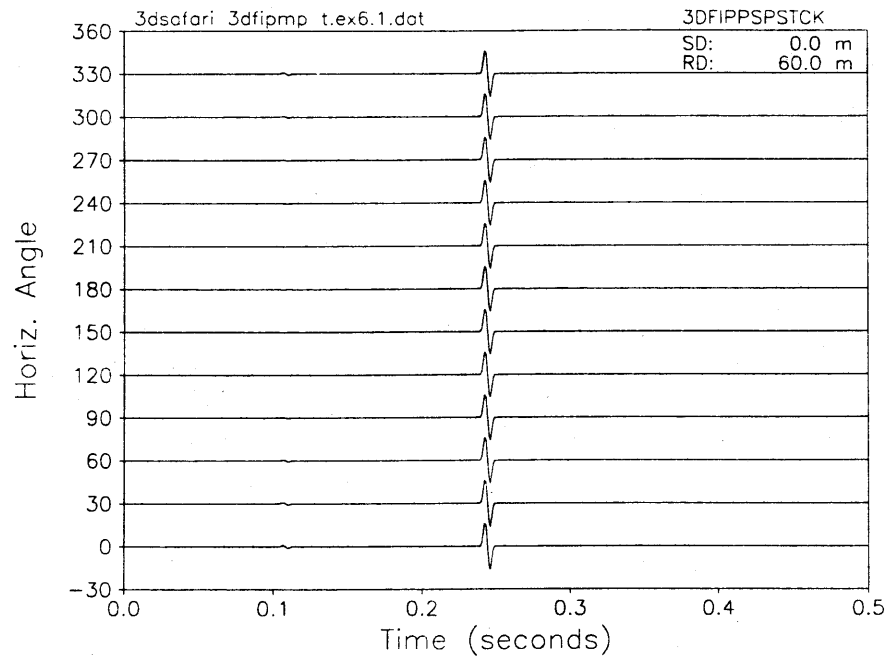
Case 5.2 Isotropic medium : In this example, the isotropic medium is considered. The other parameters are the same as previous Case 5.1, except that the compressional and shear wave speeds are 3000 and 1500 m/sec , respectively.

Through these examples, the propagation effects in a transversely isotropic medium are discussed. The slowness surfaces show the varying phase speeds depending on the propagation direction. For the horizontal direction, the waves, P , SV , and SH , travel with different speeds, while for the vertical direction, the shear waves, SV and SH waves, travels at the same speed so that the shear waves does not separate. This can be demonstrated in the synthetic time series. Again, the same source function in Fig 3.5 is used. The synthetic time series of the velocities in z , x , and y -directions are shown in Fig 5.4 and 5.5 for the cases 5.1 and 5.2, respectively. The comparison of the seismogram for Case 5.1 in Fig 5.4 with Case 5.2 in Fig 5.5 shows the separation of the SH and SV waves, as expected. The separation time can be calculated using the receiver directions from the slowness surfaces for SV and SH waves in Fig 5.3. Since the receiver positions are almost horizontal, SH arrives faster than SV wave. The relative strength of each modes of propagation as well as the propagation speed in the horizontal direction can be also identified in the modulus plot of the Hankel inverse transform integrand in Fig 5.6.

First, the equivalent five elastic constants can be calculated for the case 5.1 from Eq 5.4.

$$\begin{aligned} C_{44} &= 1.6 \times 10^9 \quad , \quad C_{66} = 2.5 \times 10^9 \quad , \\ C_{33} &= 6.4 \times 10^9 \quad , \quad C_{13} = 3.2 \times 10^9 \quad , \\ C_{11} &= 9.1 \times 10^9 \quad , \end{aligned} \tag{5.19}$$

(a)



(b)

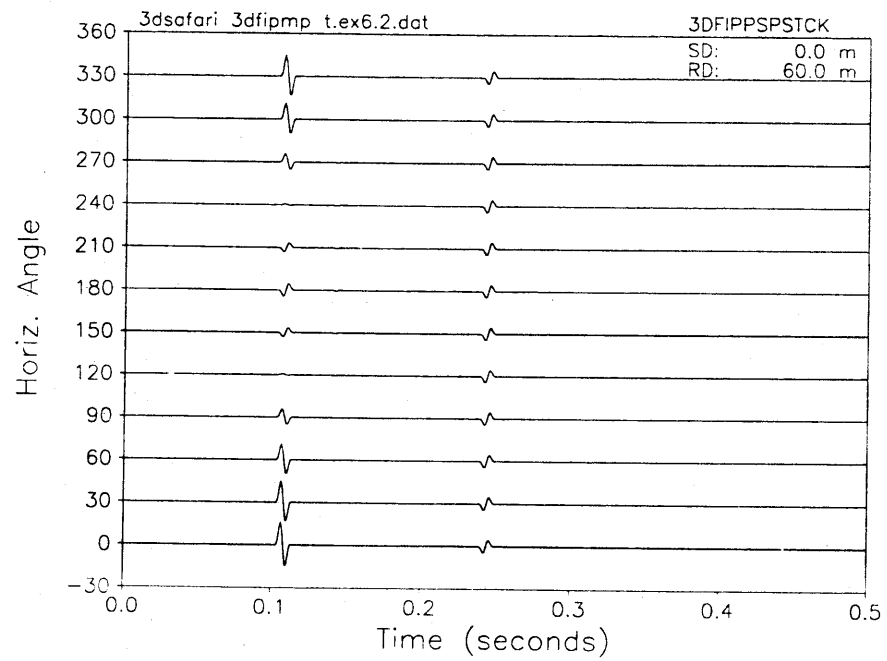


Figure 5.4: Synthetic time series in an unbounded homogeneous, transversely isotropic medium, (a) vertical velocity, (b) x-direction velocity.

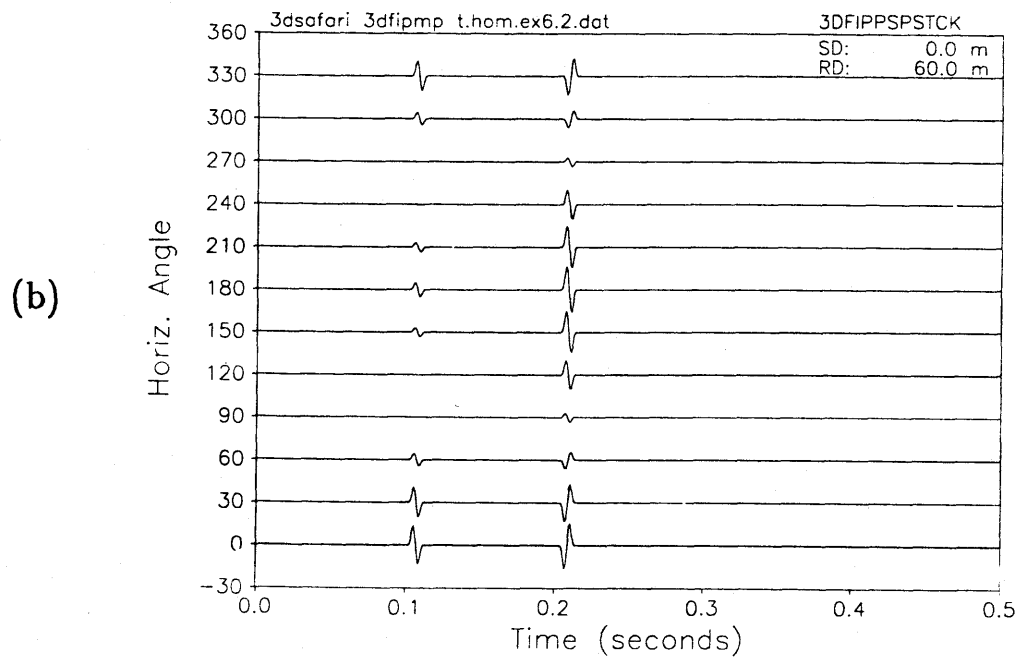
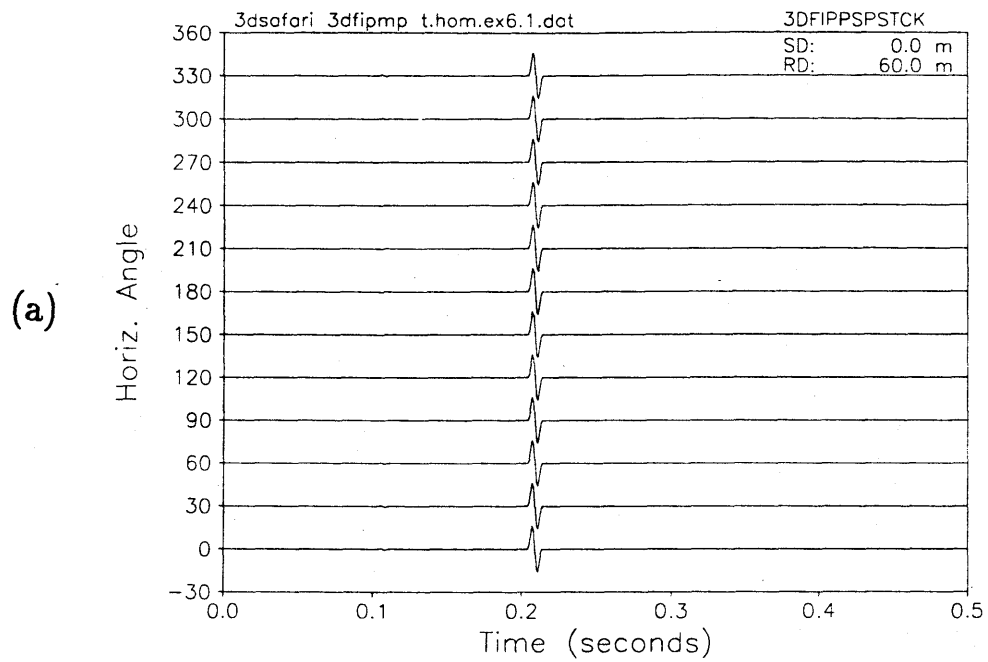


Figure 5.5: Synthetic time series in an unbounded homogeneous isotropic medium, (a) vertical velocity, (b) x-direction velocity.

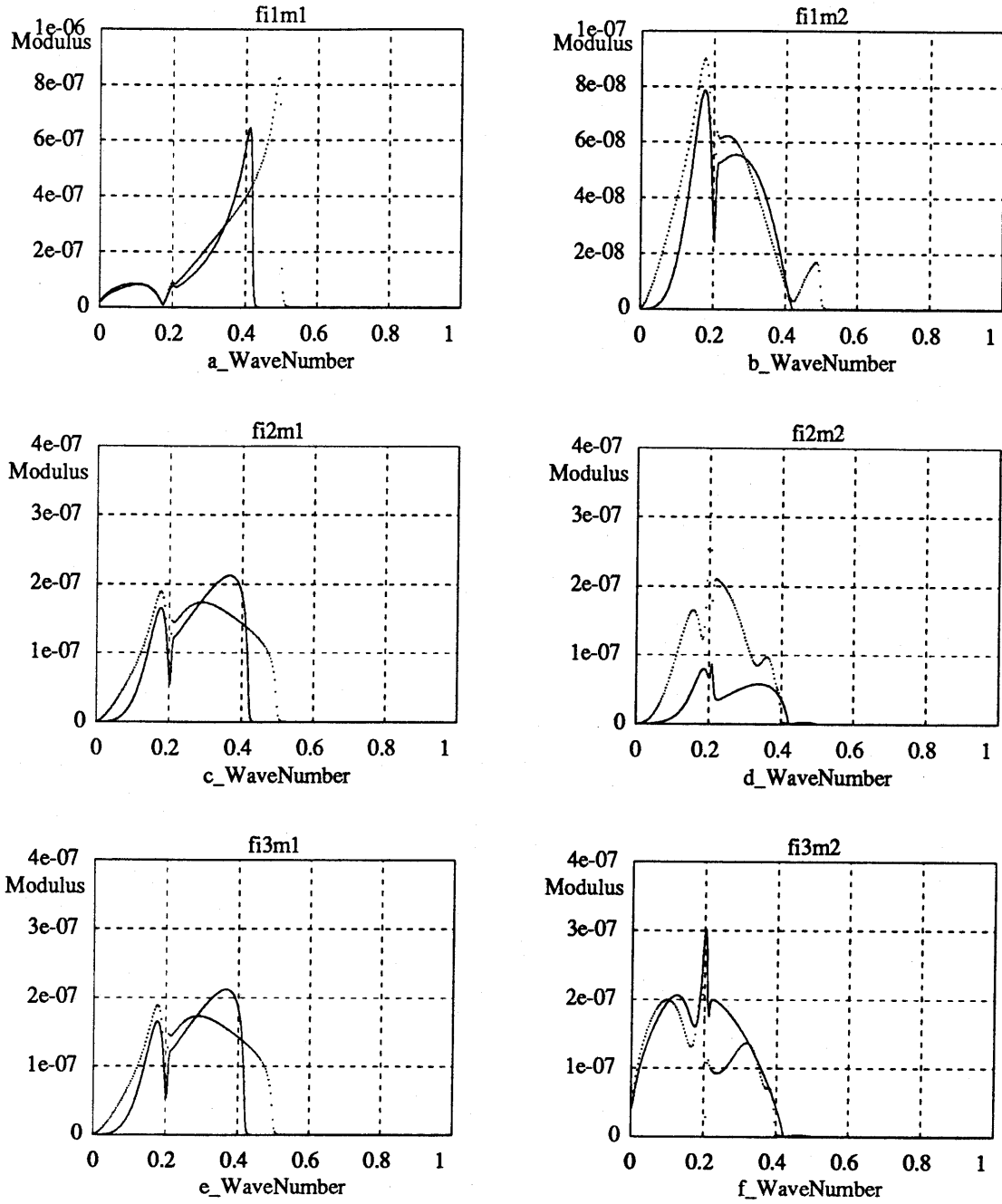


Figure 5.6: Modulus of the inverse Hankel transform integrand for the isotropic medium (solid line), and transversely isotropic medium (broken line), (a) and (b) show the vertical displacements for Fourier orders zero-th and $\cos \theta$ orders, respectively, (c) and (d) for the x -direction velocity, and (e) and (f) for the y -direction velocity.

where the unit is $Kg/m \cdot sec^2$. From these elastic constants and using the center frequency of 100 Hz, the phase speeds and wave numbers for the P , SV , and SH waves in the horizontal direction are found as

$$\begin{aligned} c_P &= \sqrt{\frac{C_{11}}{\rho}} = 3162.1m/sec \Rightarrow s = \frac{\omega}{c_P} = 0.200 \\ c_{SV} &= \sqrt{\frac{C_{44}}{\rho}} = 1326.0m/sec \Rightarrow s = \frac{\omega}{c_{SV}} = 0.474 \\ c_{SH} &= \sqrt{\frac{C_{11}}{\rho}} = 1657.5m/sec \Rightarrow s = \frac{\omega}{c_{SH}} = 0.379 \end{aligned} \quad (5.20)$$

For case 5.2, the phase speeds for all wave types are the same in all directions, and the horizontal wave number can be calculated from the phase speed and frequency,

$$\begin{aligned} c_c &= c_P = \sqrt{\frac{\lambda + 2\mu}{\rho}} = 3000.m/sec \Rightarrow s = 0.209 \\ c_s &= c_{SV} = c_{SH} = \sqrt{\frac{\mu}{\rho}} = 1500.m/sec \Rightarrow s = 0.419 \end{aligned} \quad (5.21)$$

Now, the moduli of the inverse Hankel transform integrand in Fig 5.6 can be interpreted based on the horizontal wave numbers found from the phase speed of each mode. The peaks at $s = 0.419$ and 0.474 in Fig 5.6(a) for the zeroth Fourier order of vertical velocity represent the dominant SV wave in the isotropic and the transversely isotropic medium, respectively. For the first Fourier order of the vertical velocity in Fig 5.6 (b), the peak at $s = 0.474$ for the SV wave in the transversely isotropic medium is observed, which does not exist in the isotropic medium. The magnitude of the zeroth order is greater than the first order by an order of 10, the directional variation in the horizontal angle is negligible in the synthetic time series for the vertical velocity in Fig 5.4 and 5.5 (b) and (c). The peaks at $s = 0.200$ and 0.209 in Fig 5.6 (d) for the first Fourier order shows the P wave in the isotropic and the transversely isotropic medium, respectively. Another peak at $s = 0.379$ is the contribution of the SH wave, of which peak appears only in the transversely isotropic medium.

Although the modulus of the inverse Hankel transform integrand is not the final form of the quantitative field presentation, it gives the idea of what modes of wave exist and are dominant. The previously given examples are, however, the most simple cases without any boundaries, where the group velocity is the same as the phase speed, and not dispersive. When there exists a wave guide, the Hankel transform integrand can be very useful in identifying the phase speed of existing modes along with the dispersion relation. These examples in relation to the wave propagation in the floating ice plate in the central Arctic environment will be discussed in Chapter 6.5.

Chapter 6

Application to Ice Crack

Radiation in the Central Arctic Environment

The main source of the central Arctic ambient noise has been known to originate from the elastic motion of the ice plate caused by environmental stresses. When the stress in the ice plate is locally greater than the strength of the ice causing fracture, the stored energy is released in the form of elastic motion of the ice. This energy radiates into the water, forming ambient noise when the events are aggregated. In order to better understand the Arctic ambient noise generating mechanism, two levels of approaches are being pursued [9]. One approach is to correlate the spectral and temporal characteristics of ambient noise to gross environmental parameters such as thermal changes, current and wind stresses [33]. The other level of approach is to look into the individual ice cracking events, and treat them as a noise generating source element, which forms the average ambient noise when aggregated. The latter approach is based on the assumption that the central Arctic ambient noise is dominated by the radiation due to

mechanical processes in the ice cover, so that the ambient noise is aggregate of individual events [9] [34]. Therefore, it is obvious that the models that represent probable source mechanisms of a single event need to be developed to understand the central Arctic ambient noise characteristics as an aggregate of events.

In order to be more specific about the issue investigated in this study in relation to the central Arctic ambient noise, the processes involved in the generation of Arctic ambient noise can be categorized as

- (1) Development of environmental stresses,
- (2) Ice plate motion induced by fracture due to the environmental stresses,
- (3) Radiation from the ice plate into water.

The first phenomenon has been extensively studied and associated with the observed ambient noise [31] [33]. The radiation mechanism from the ice plate to water is also studied by some authors [42] [24] [23] [22]. However, previous publications are mostly speculative, and assume certain simple source types in the ice plate. Also, it is not clearly understood yet how the environmental stresses are released as a major source of induced ice motion. The possible candidates are the three dominant types of crack [18]. Since the field observation of such cracks does not seem to be feasible, modeling of radiation from different types of crack is comparative to infer the source mechanism from the observed signal of the ice event.

Another motivation of the modeling will be the expectation that an understanding of the relationship between the observed acoustic signal and the physical process of sound generation will lead to the development of remote sensing techniques suitable for the study of ice behavior and properties [10].

In this study, the scattering is not included, which may be important in average ambient noise for certain frequencies [22]. But, the observation of individual event is made in the near field, where presumably the scattered field is much

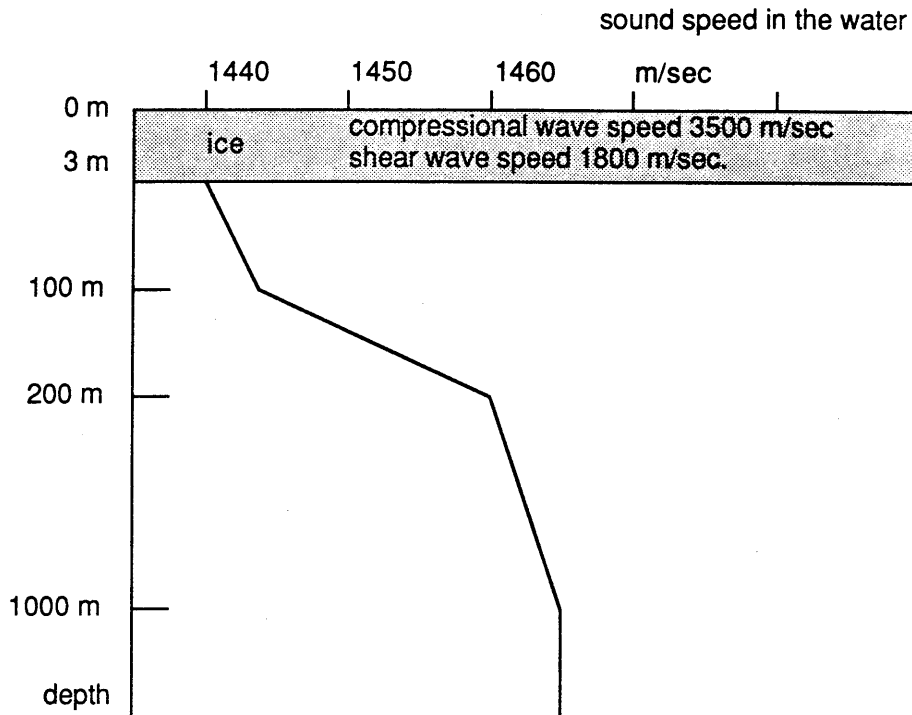


Figure 6.1: Geometry for central Arctic environment.

smaller than the direct field. It is noted that the attenuation can be included by using complex wave number, and the water absorption is also included.

In Section 6.1, the environmental model for Central Arctic is discussed. In Section 6.2, the radiation from three types of cracks is considered. For different types of sources, the radiation pattern and temporal characteristics are given and discussed. In Section 6.4, the effect of the non-compact and propagating crack is discussed. Next, in Section 6.5, it is stated qualitatively how the important parameters affects the radiation pattern and the spectral and temporal characteristics. In Section 6.6, the effects of the anisotropy observed in the sea ice on the propagation are discussed. Finally, in Section 6.7, the results are summerized, and an experiment will be proposed based on the results.

6.1 The Central Arctic Environment

The central Arctic environment can be idealized as the laterally stratified medium, assuming smooth boundaries¹, and neglecting the scattering due to ice ridges and roughness. The assumption of homogeneity of the ice can be justified up to the frequency of wave length much larger than the grain size of ice separated by brine pocket. However, the inhomogeneity due to the temperature change along thickness is expected to be significant. The change of the compressional and shear speed due to the seasonal temperature is also significant [16], but the ice is assumed to be homogeneous for the purpose of studying radiation characteristics, concentrating on the source mechanisms. However, it is noted that there is no limitation in obtaining solutions for such environmental model.

The Arctic environment assumed in this study consists of 6 layers (Fig 6.1). The first layer is a vacuum half space, and then, a homogeneous elastic ice layer of 3 *m* thickness. The next three layers are acoustic layers with sound speed gradient, for which the analytical solution can be obtained in the form of Airy functions. The last layer is a fluid half space with constant sound speed. Although the bottom can be replaced by a sediment layer at 3000 *m* deep, the contribution from bottom reflection will be neglected.

¹The scattering due to rough surface has been treated by Kuperman and Schmidt [21]. This scattering effect may affect significantly the average ambient noise, but it is neglected in studying the direct radiation from sources.

6.2 Radiation from Three Modes of Compact Cracks

In this section, the acoustic emission from different compact sources in the ice plate will be studied using the developed numerical code. The central Arctic environment in Fig 6.1 is considered, and a compact crack is assumed to be induced at 1 *m* from the top of the ice. The source time series and spectrum for the seismic moment is shown in Fig 6.2. The fault orientation parameters are $\delta = 90^\circ$ and $\phi_s = 0^\circ$, as the cases considered before. Note that the strike angle ϕ_s is referred to *x*-axis, i.e. the crack surface is parallel to the *xz*-plane as shown in Fig 3.6. The following cases will be considered.

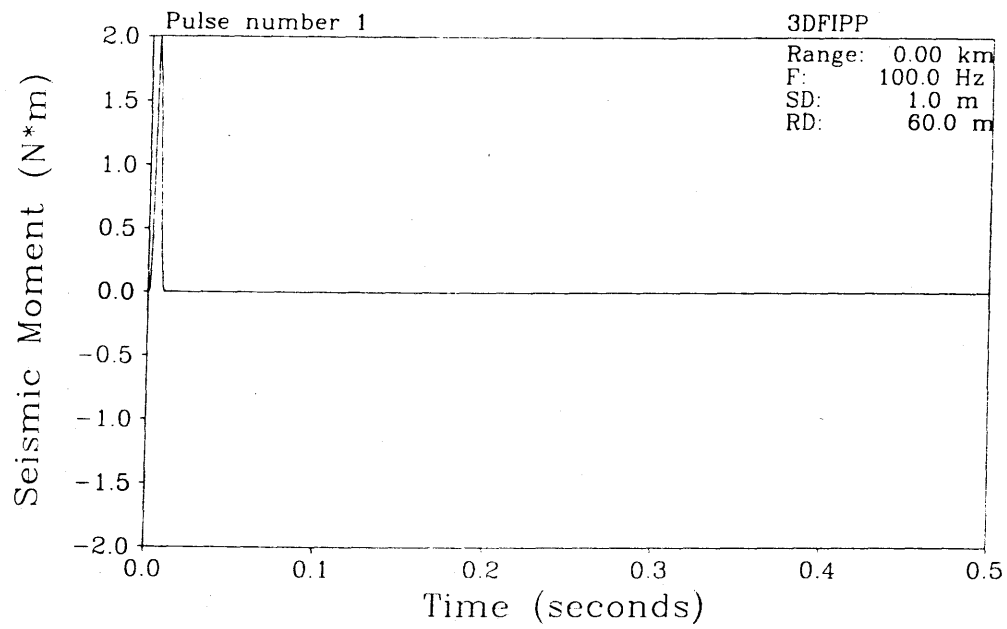
Case 6.1 *Compact tensile crack with receivers at $z = 60$ m* : The results are shown in Fig 6.3 for radiation pattern and synthetic time series. The receiver locations are same as for the previous outputs as in Fig 3.6.

Case 6.2 *Compact tensile crack with receivers at $z = 5$ m* : The synthetic time series is shown in Fig 6.4, where the only difference from the *Case 6.1* is that the receiver depth is now at $z = 5$ m in order to observe the radiation from the evanescent first antisymmetric mode in the floating ice plate. The inverse Hankel integrands for the different receiver depths at $z = 5$ and $z = 60$ m are given in Fig 6.6.

Case 6.3 *Compact dip-slip* : The same source and environment as in the *Cases 6.1* and *6.2* are considered, except the source type is dip-slip. The radiation pattern and synthetic time series are given in Fig 6.7

Case 6.4 *Compact strike-slip* : The same source and environment are considered, except the source type is strike-slip. The radiation pattern and synthetic time series are given in Fig 6.8

(a) SOURCE PULSE



(b) SOURCE SPECTRUM

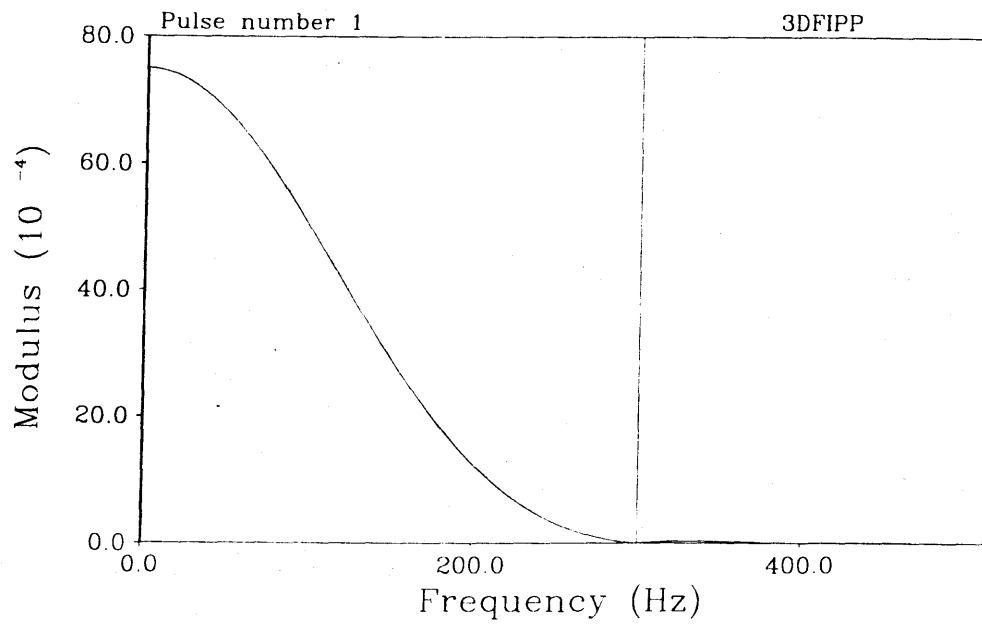


Figure 6.2: Seismic moment (a) source function, (b) spectrum

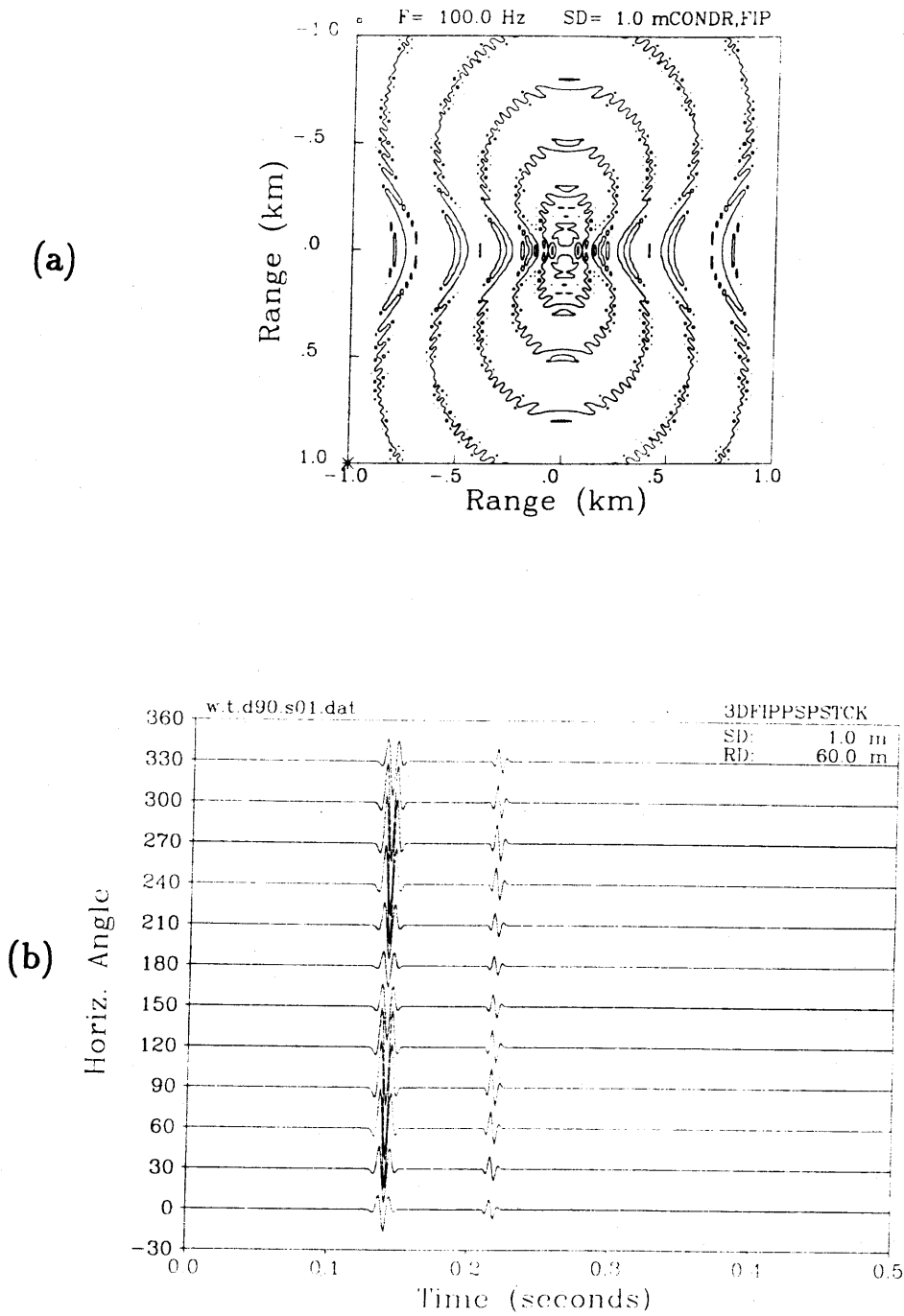


Figure 6.3: (a) Radiation pattern for $f = 100$ Hz, (b) synthetic time series for tensile crack with dip angle $\delta = 90^\circ$ in the central Arctic environment.

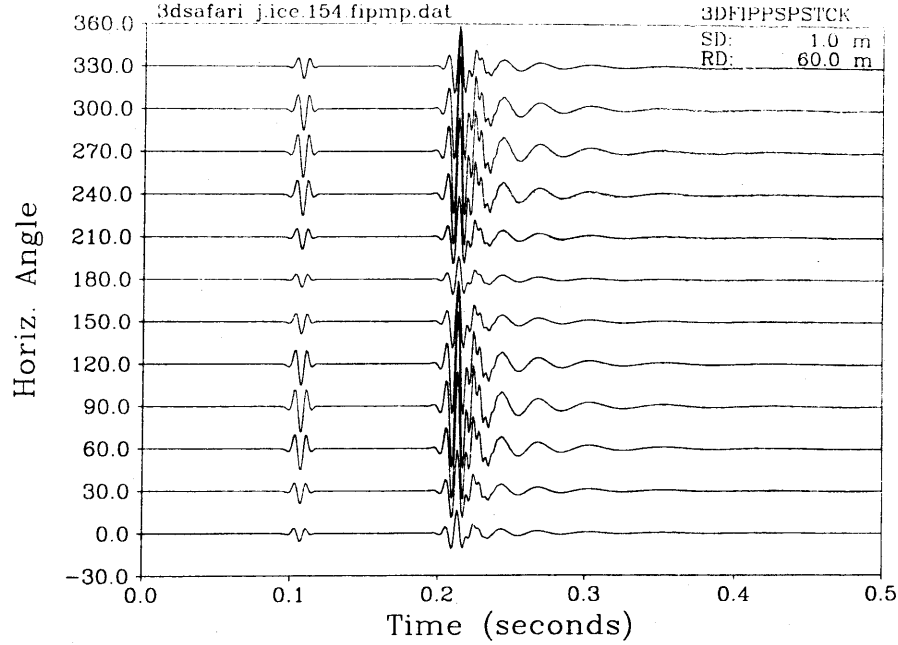


Figure 6.4: Synthetic time series for tensile crack with dip angle $\delta = 90^\circ$, receivers at $z = 5 \text{ m}$, $r = 300 \text{ m}$ at every 30° in a central Arctic environment.

Two kinds of graphical display will be used. The first one is the contour plot of the pressure field at 60 m depth, in Fig 6.3(a), 6.7(a), and 6.8(a) for tensile crack, dip-slip, and strike-slip, respectively. For the same geometry and sources, the synthetic time series are presented in Fig 6.3(b), 6.7(b), and 6.8(b). Since the hydrophones are placed in the water, the pressure (negative of normal stress) will be studied.

Considering the tensile crack case, the pressure field in the water at 60 m depth shown in Fig 6.3 reflects the radiation pattern for tensile crack. The time series in Fig 6.3 (b) shows two arrivals. As discussed in Stein [42], the first arrival is a radiation from the first symmetric mode in the ice plate, often referred as the longitudinal mode. The second arrival is the so called acoustic mode, i.e. the mainly waterborn arrival. The arrival time of the first signal can

DISPERSION CURVES

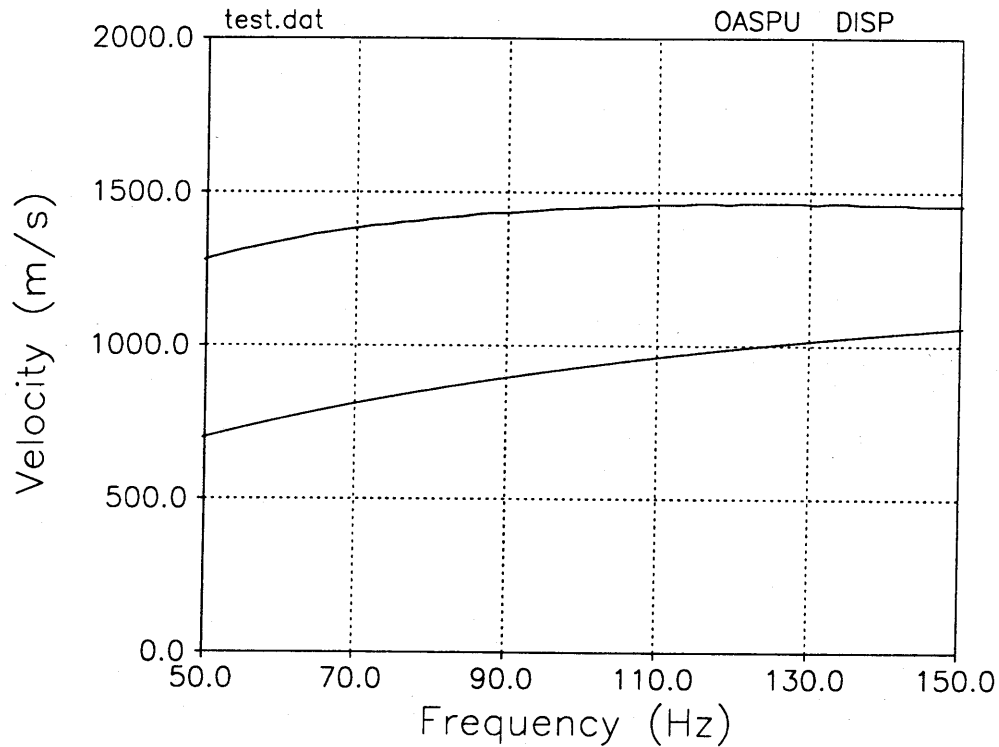


Figure 6.5: Dispersion curve for the first antisymmetric mode of the ice plate, the upper line is for the group velocity and the lower line for the phase speed.

be roughly calculated from geometry by considering the critical angle at the ice-water interface, giving 0.121 sec. The second arrival time is 0.212 sec. Another mode that exists is the contribution of the radiation from the first antisymmetric mode in the ice plate, which is often referred as the flexural mode. However, at low frequencies, the first antisymmetric mode travel subsonically in the ice plate with an evanescent field in the water. Since the 60 *m* depth is 2 wave lengths deep for 50 Hz, which is the lower limit of the frequency components of the source function given in Fig 3.5, this mode does not appear in the synthetic time series shown in Fig 6.3(b). In order to see the dispersive flexural wave

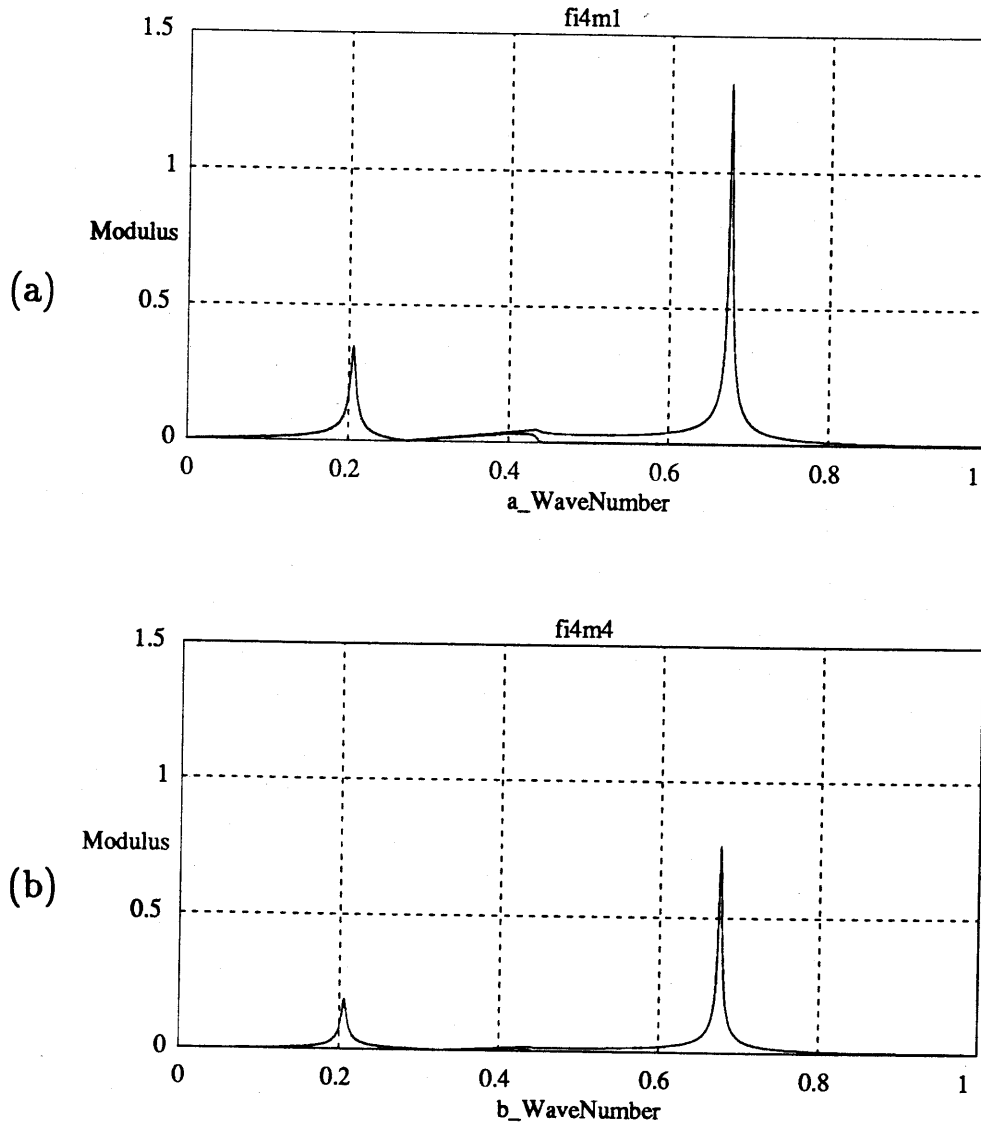


Figure 6.6: Modulus of inverse Hankel transform integrand for Fourier (a) zeroth and (b) second, $\cos 2\theta$, orders and frequency $f = 100$ Hz, at $z = 5$ m and $z = 60$ m.

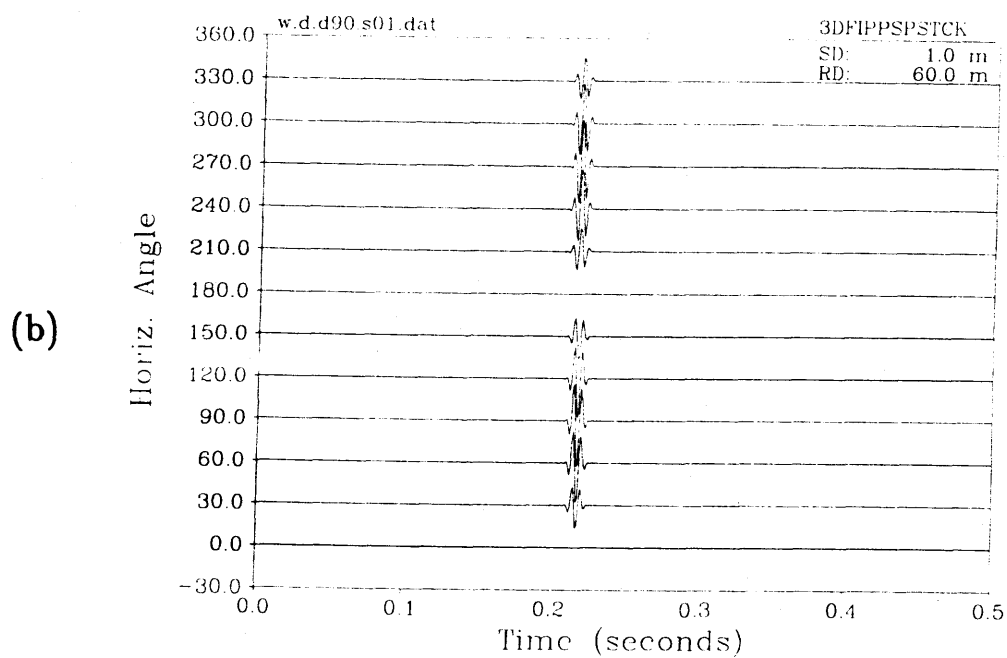
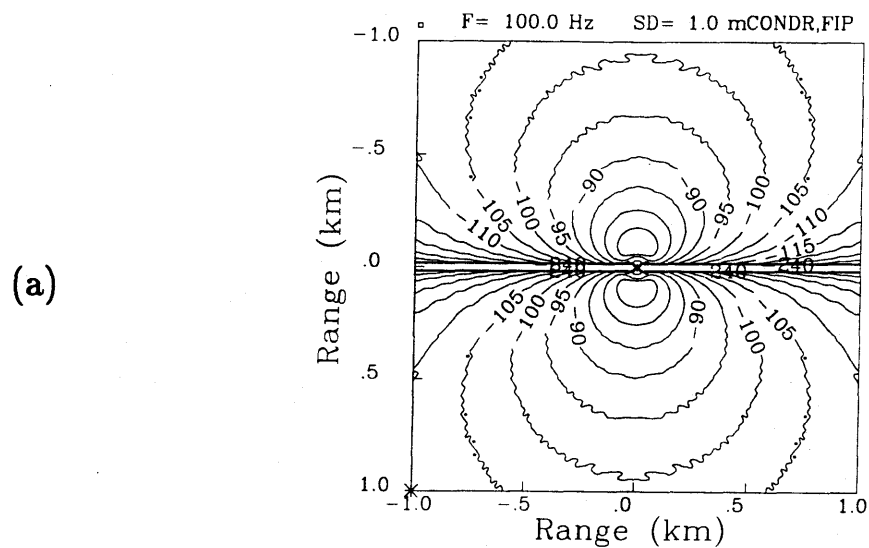


Figure 6.7: (a) Radiation pattern for $f = 100 \text{ Hz}$, (b) synthetic time series for dip-slip with dip angle $\delta = 90^\circ$ in a central Arctic environment

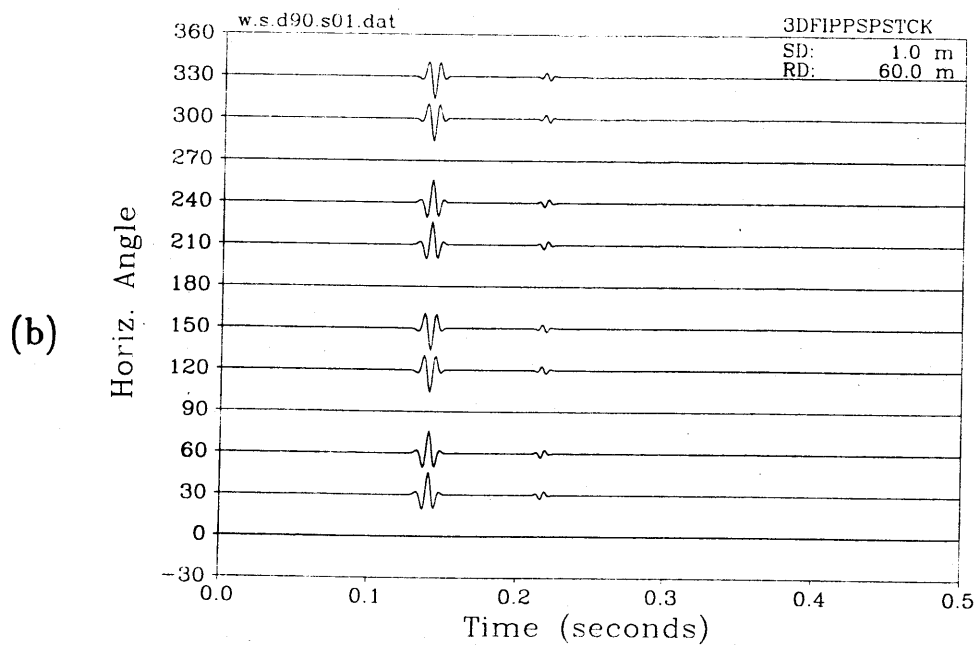
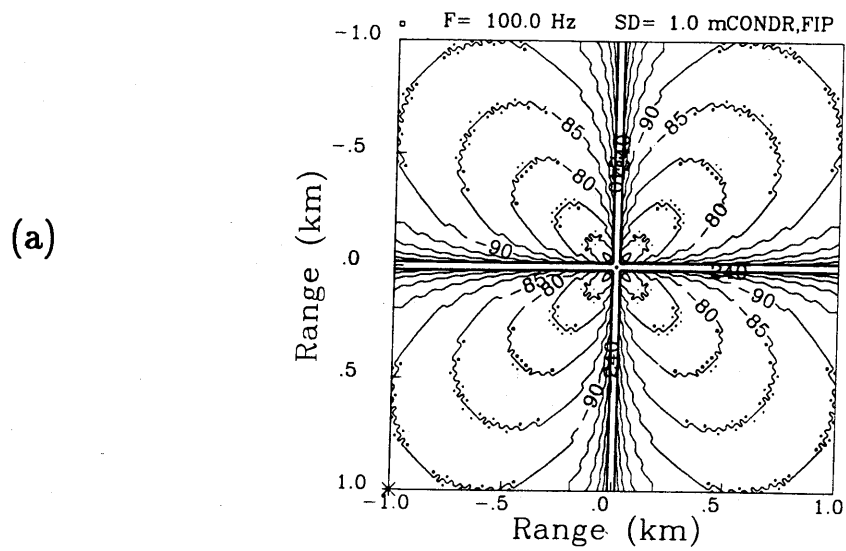


Figure 6.8: (a) Radiation pattern for $f = 100 \text{ Hz}$, (b) synthetic time series for strike-slip with dip angle $\delta = 90^\circ$ in a central Arctic environment.

radiation, the receiver is placed at $z = 5m$, for which the synthetic time series for pressure is shown in Fig 6.4. At this point, it will be helpful to look at the modulus of the integrand of inverse Hankel transform for each Fourier orders in order to identify how the energy trapped in the ice plate contribute to the pressure below the ice. The moduli of integrand for depth $z = 5 m$ and $60 m$ are given in Fig 6.6. The modulus of the integrand for Fourier zeroth order at depth $z = 60 m$ has two peaks at horizontal numbers $s = 0.205$ and 0.435 . The phase velocity of the first peak is $3065 m/sec$, and represents the radiation from the first symmetric mode in the ice plate. The second peak appears at a speed of $1444 m/sec$, and corresponds to horizontal acoustic propagation in the water. The modulus in Fig 6.6 shows another peak at horizontal wave number $s = 0.675$ corresponding to the first antisymmetric mode radiation. This mode has a phase speed of $931 m/sec$. However, the arrival from the flexural mode arrives almost same time as the acoustic mode in Fig 6.4. The explanation to this arrival time difference is contributed to the fact that the group velocity of antisymmetric mode is larger than its phase speed. In fact, the dispersion curve of the first antisymmetric mode of ice plate can be determined numerically from the Hankel integrand using the relation,

$$c_g = \frac{d\omega}{dk} . \quad (6.1)$$

Eq 6.1 has been estimated numerically for the flexural wave, with the result shown in Fig 6.5 together with the associated phase speed. The dispersion curve shows that the group velocity is $\approx 1450 m/sec$. and the phase velocity is $\approx 930 m/sec$. for $100 Hz$, in agreement with the observation of the Hankel integrand. In the high frequency limit, the phase velocity will approach to the speed of the interface waves, i.e. Stoneley waves for the elastic-acoustic and elastic-elastic interfaces or Rayleigh waves for the elastic half space, where the wave is no longer dispersive. Since the group velocity is dispersive for the present

cases, the waves with low frequencies arrive late, which can be seen in Fig 6.4. For the second Fourier order $\cos 2\theta$, the position of poles are the same but the magnitude is about half of the zeroth order, which explains the slowly varying amplitude along the azimuthal angle θ in Fig 6.3 and 6.4. Thus, the observation of the Hankel integrand gives physical insights in the excitation of the various modes, and their corresponding phase speeds.

For the dip-slip crack, the pressure field and time series are given in Fig 6.7. The amplitude of the first arrival, i.e. radiation from the symmetric mode in the ice plate is of much smaller amplitude than the acoustic arrival, while, for strike-slip (Fig 6.8), the amplitude of the acoustic mode is small. This is contributed to the different source mechanisms. For dip-slip with dip angle $\delta = 90^\circ$ which is presently considered, the particle motion is induced in vertical direction causing more volume fluctuation at the ice-water interface, however, for strike-slip, the particle motion is in horizontal direction exciting the compressional wave more effectively.

Another important observation can be made from the transfer functions of each crack mode. Denoting the source function in Fig 6.2 as $s(t)$ in time domain and $S(f)$ in frequency domain respectively, and the system transfer function $h(t)$ and $H(f)$ for each mode of cracks, the received signal at a receiver position \mathbf{r} can be expressed as

$$\begin{aligned} r(t, \mathbf{r}) &= s(t) * h(t, \mathbf{r}) \\ R(f, \mathbf{r}) &= S(f) \cdot H(f, \mathbf{r}) \end{aligned}$$

in the time and frequency domains. The transfer functions at the receiver position $r = 300$ m, $d = 60$ m, and $\theta = 30^\circ$, are shown in Fig 6.9. The vertical axis represents

$$Y = 20 \log_{10} |H(f)|. \quad (6.2)$$

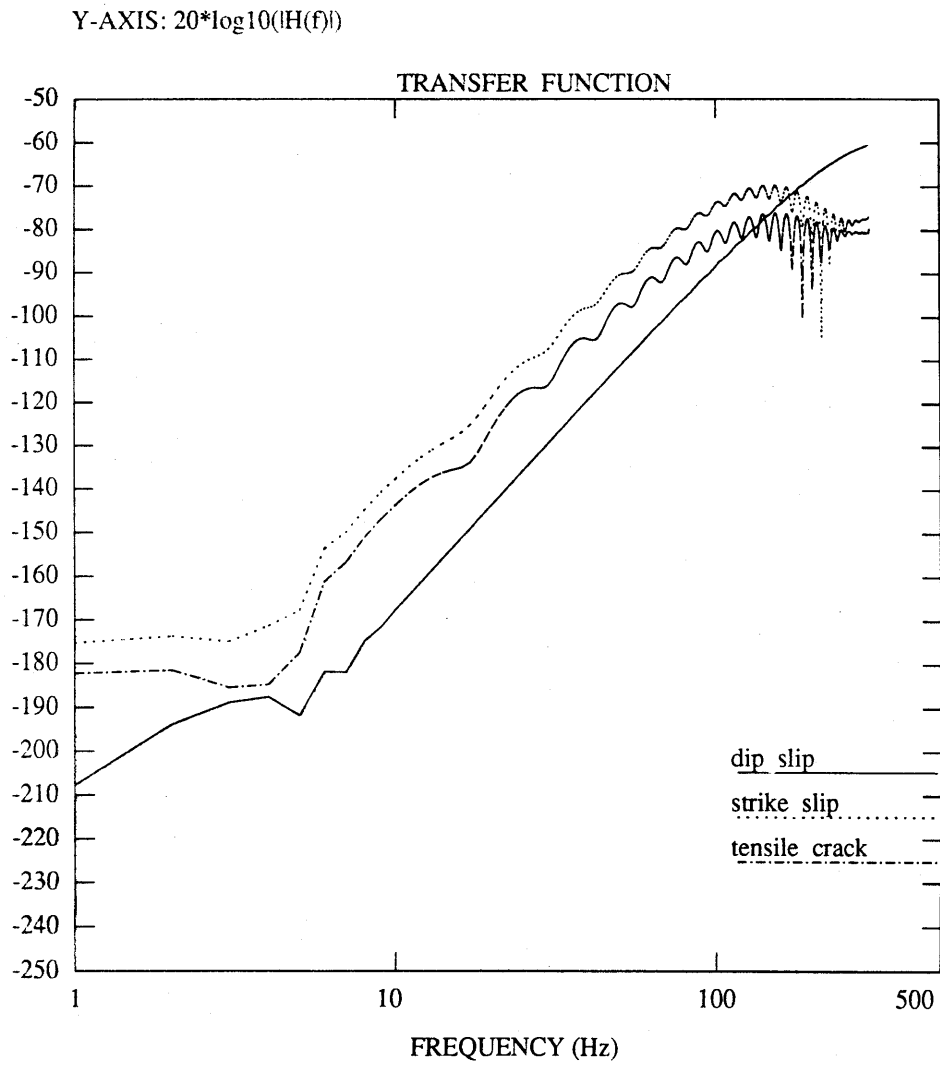


Figure 6.9: Transfer functions for each mode of cracks

The transfer function characterizes the spectral shape of the received signal for an impulse source function of a particular crack type, as can be seen in Fig 6.9. However, the source type is not known priori, and has to be observed. Thus, the transfer function can be only used for source time series inversion if the source type is known.

It has been shown, from the figures 6.3, 6.7, and 6.8, that the radiation patterns and other information concerning the different types of cracks including the relative strength of existing modes, can be obtained. These distinct characteristics of each crack mode can be used to identify the dominant source mechanisms in the central Arctic environment from the collected data. These discussions are found in the following section.

6.3 Most probable source types and corresponding source strength

Most Probable Source Types

Among the three examples in the previous section, it is shown that the radiation from the longitudinal wave in the ice plate is much stronger than the acoustic mode in the water for tensile crack and strike-slip with dip angle $\delta = 90^\circ$, which is not the case for the observed signal in the central Arctic environment². Thus, the ratio of the amplitude of the radiation from the longitudinal wave in the ice plate (A_l) to the amplitude of the acoustic mode (A_a) can be used to determine the most probable source types. The ratio, $\frac{A_l}{A_a}$, are shown in Fig 6.10 for three crack types with different fault orientations. From the figure, the source types that

²Discussion with Professor Dyer

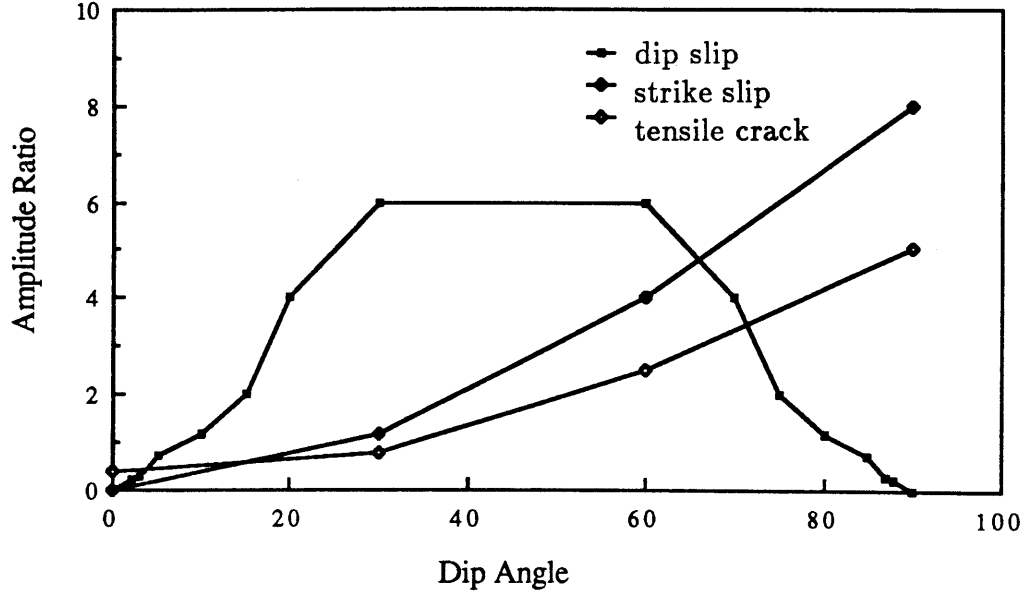


Figure 6.10: Ratio of the amplitude of the radiation from the longitudinal wave in the ice plate(A_l) to the amplitude of acoustic mode(A_a), i.e. $\frac{A_l}{A_a}$, for three types of cracks with varying dip angle

satisfy the relative smallness of the radiation from longitudinal wave compared to the acoustic mode are dip-slip with dip angle $\delta \approx 0^\circ$ and 90° and strike-slip with dip angle $\delta \approx 0^\circ$. In fact, it is noted that the mathematical formulation for strike-slip with dip angle $\delta = 0^\circ$ is the same as those of dip-slip with dip angle $\delta = 0^\circ$ and 90° .

The previous study by Stein[42] used acoustic monopole as a source in the ice plate. Due to the nature of the omnidirectional volume expansion, the radiation from the longitudinal wave in the ice plate is much stronger than the acoustic mode. Study by Langley[24,23,22] used a point force[24,23] and tensile crack[22]. The radiation pattern at farfield caused by tensile crack with vertical fault surface(dip angle $\delta = 90^\circ$) shows the strong radiation from the longitudinal

wave in the ice plate regardless of the source depth at frequencies around 100 Hz, which agrees with the results given in section 6.2.

Source Strength Inversion

Since the formulations for dip-slip with dip angle $\delta = 0^\circ$ and 90° , and strike-slip with dip angle $\delta = 0^\circ$, are all same, dip-slip with dip angle 90° are considered for source strength inversion from the pressure in the water.

The pressure amplitude of synthetic time series in Fig 6.11 at range $r = 300\text{ m}$ and at depth $z = 60\text{ m}$ in the horizontal angle $\theta = 30^\circ$ is used to find the source strength. The seismic moment to produce pressure 1 Pa at the specified receiver position is

$$M = 2.5 \times 10^5 N \cdot m$$

Since the seismic moment is $M = A\bar{u}\mu$,

$$A\bar{u} = \frac{2.5 \times 10^5}{\mu} = 8.6 \times 10^{-5} m^3$$

The average displacements on the fault surface for give fault surface area are

| $A\text{ m}^2$ | $\bar{u}\text{ mm}$ |
|----------------|---------------------|
| 10 | 0.0086 |
| 1 | 0.086 |
| 0.1 | 0.86 |
| 0.01 | 8.6 |

The pressure field variation depending on the horizontal angle and range for 200 Hz is shown in Fig 6.12.

Although the amplitude ratio for the tensile crack with dip angle $\delta = 0^\circ$, $\frac{A_t}{A_s}$, is somewhat large, the source strength will be given since the amplitude of

RECEIVED SIGNAL

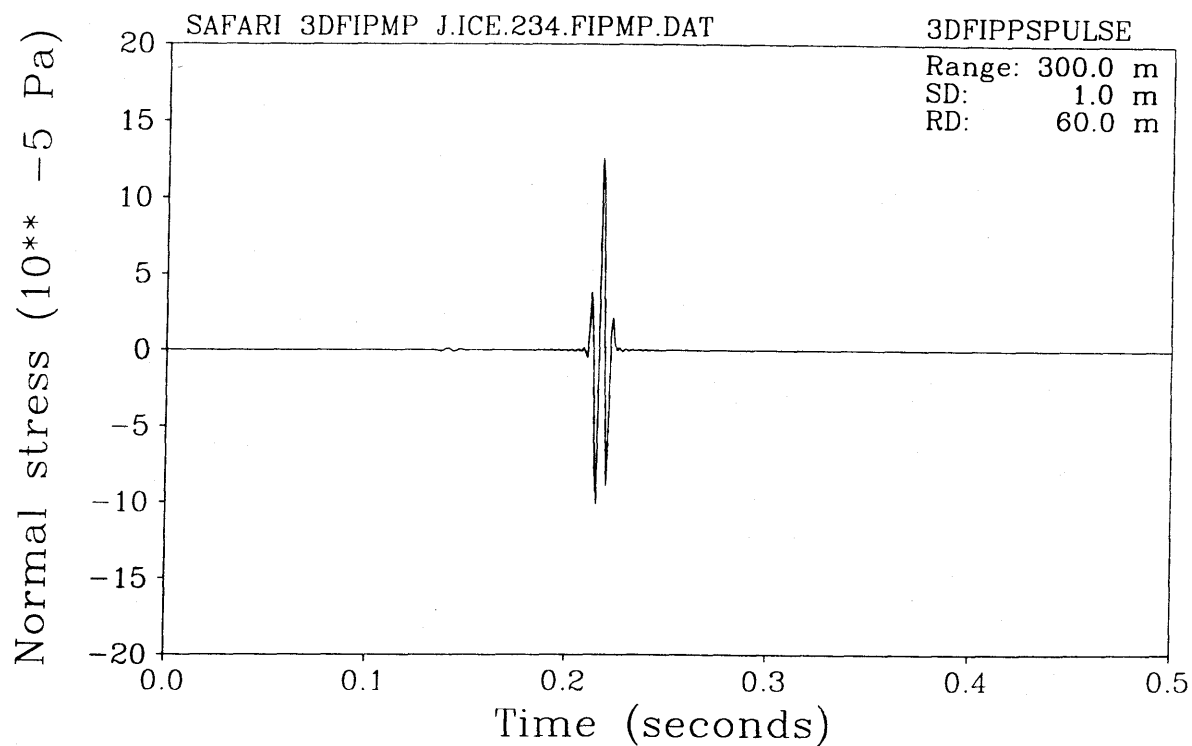


Figure 6.11: Synthetic time series in the horizontal direction 30° at range $r = 300$ m and at depth of $z = 60$ m for dip-slip with dip angle $\delta = 0^\circ$

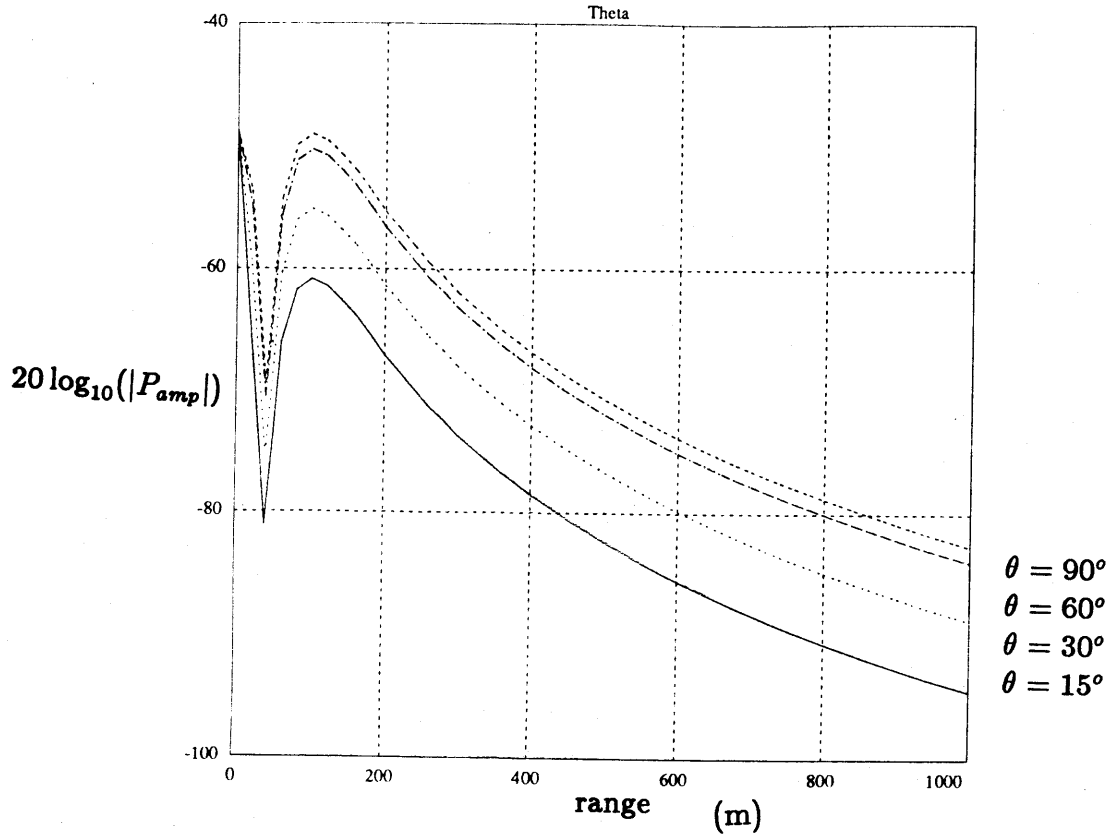


Figure 6.12: Field pressure variation depending on the horizontal angle and range for 200 Hz., source strength is $4\pi N \cdot m$

radiation from the longitudinal wave is affected by scattering due to the rough surface of ice plate. From Fig 6.13, the seismic moment to produce pressure 1 Pa at the same receiver position is

$$M = 7.5 \times 10^6 N \cdot m$$

Since the seismic moment is $M = A\bar{u}(\lambda + 2\mu)$,

$$A\bar{u} = \frac{7.5 \times 10^6}{\lambda + 2\mu} = 6.8 \times 10^{-4} m^3$$

The average displacements on the fault surface for give fault surface area are

RECEIVED SIGNAL

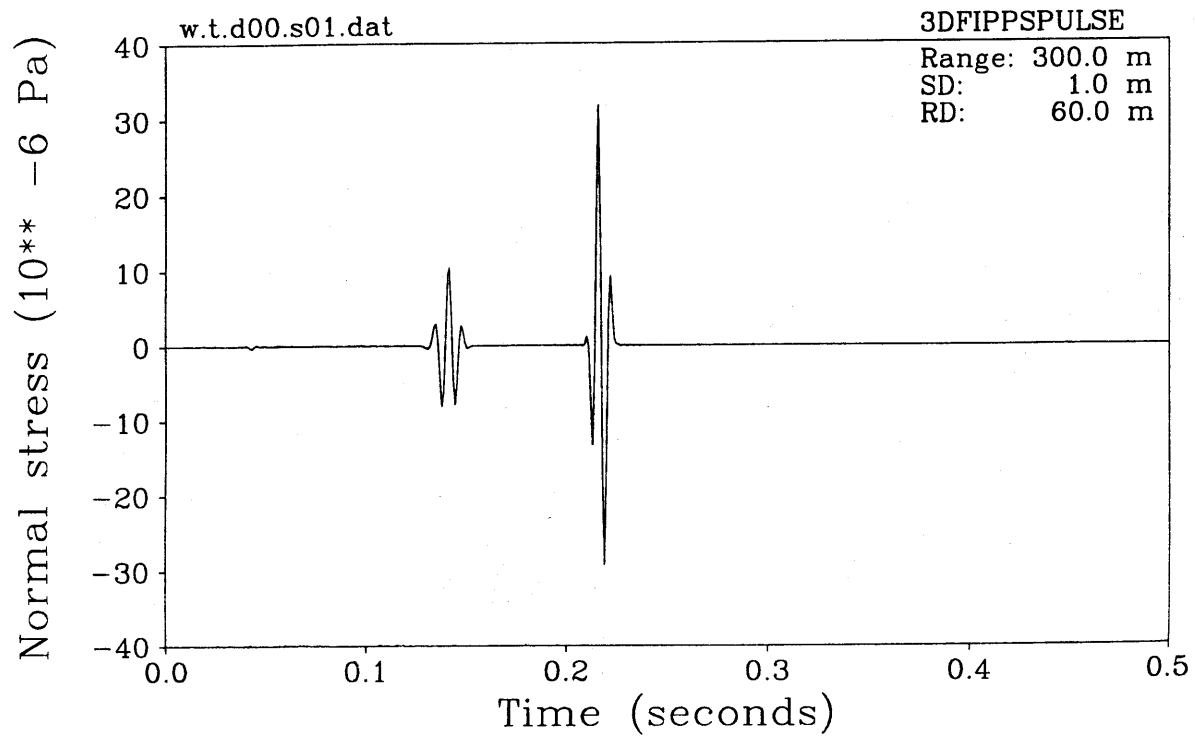


Figure 6.13: Synthetic time series in the horizontal direction 30° at range $r = 300$ m and at depth of $z = 60$ m for tensile crack with dip angle $\delta = 0^\circ$

| $A \text{ m}^2$ | $\bar{u} \text{ mm}$ |
|-----------------|----------------------|
| 10 | 0.068 |
| 1 | 0.68 |
| 0.1 | 6.8 |
| 0.01 | 68 |

6.4 Radiation from Propagating Cracks

The effect of the cracks being non-compact is important for the frequencies with wave length of order of crack length or less, causing frequency dependent directivity pattern. In reality, the crack dimension varies from the order of grain boundary length to order of $10^3 \sim 4 \text{ m}$. The field data analysis by Farmer[10] suggests that the crack could be non-compact, and the estimated crack length range between 27 and 63 m for maximum length based on the analysis of four events. For the crack propagation speed, Mansinha[30] showed that the maximum crack propagation speed for a medium with Poisson's ratio of 0.25 is $0.775c$, for pure shear fracture and $0.631c$, for pure tensile fracture. The fracture propagation speed increases as the Poisson's ratio increases. Therefore, for the case of propagating cracks in the ice plate, the propagation speed will be assumed to 1200 m/sec . for all types of crack. The model developed in Chapter 4 is applied to the following examples with a set of typical source parameters to investigate the effect of propagating cracks. The radiation from propagating cracks for the same environment (Fig 6.1) is considered. The source types are again tensile, dip-slip, and strike-slip cracks with fault dip angle $\delta = 90^\circ$ and strike angle $\phi_s = 0^\circ$. The crack geometry is considered to be a unilateral line crack with length 10 m , propagating from $x = -5 \text{ m}$ to $+5 \text{ m}$. Since the smallest wave length $\lambda = c_{min}/f_{max}$, where $f_{max} = 150 \text{ Hz}$ and $c_{min} = 1800$

m/sec for shear wave speed, is greater than $10\ m$, the spacing between source should be smaller than $\lambda/8$, which corresponds to phase difference $\pi/4$. In the following examples, the distance between the discretized sources are taken to be $1\ m$. The vertical dimension of the fault surface is also assumed to be less than $\lambda/8$ to be treated as a vertically compact line crack. In order to consider a crack with a vertical dimension greater than $\lambda/8$, it is necessary to use a two dimensional surface crack rather a line crack. Therefore, the propagating cracks presently considered are internal cracks centered at $z = 1\ m$.

Case 6.5 *Propagating dip-slip* : The radiation pattern and synthetic time series are given in Fig 6.14

The pressure field for dip-slip for 100 Hz harmonic source function (Fig 6.14) is compared to the non-propagating compact crack (Fig 6.7). The spatial phase interference causes the directivity pattern varying rapidly in the azimuthal angle θ . The dominant radiation direction is not quite clear since the direction of major lobe is affected not only by the radiation pattern of the particular source type, but also by the propagation speed. Since the crack propagation speed is subsonic, i.e. less than the sound speed in the water, the major lobe does not appear in the real space. However, for dip-slip, the acoustic mode is dominant, defining the dominant radiation direction more clearly. The pressure field in 0° and 180° directions vanish as the dip-slip radiation pattern has null in those directions. This is an indication of strong dependence of the radiation of propagating crack on the source types.

An important observation is the modulated, spread signal in the time series (Fig 6.14(b)). This is directly contributed to the modulation introduced by distributed sources over the fault surface. The later arrival especially in the direction of $\theta = 150^\circ$ has been observed in the crack radiation experiment by

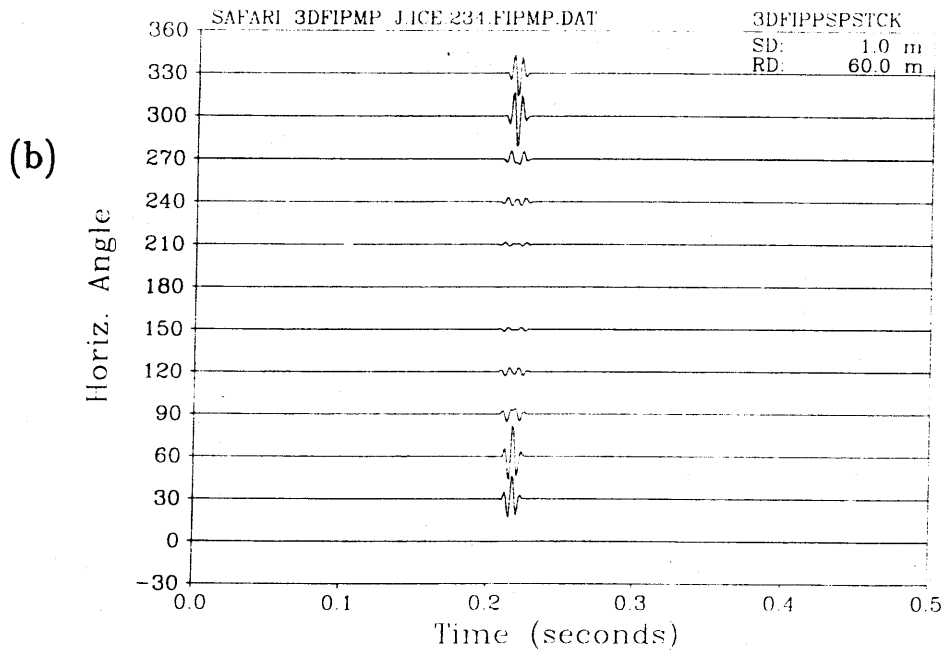
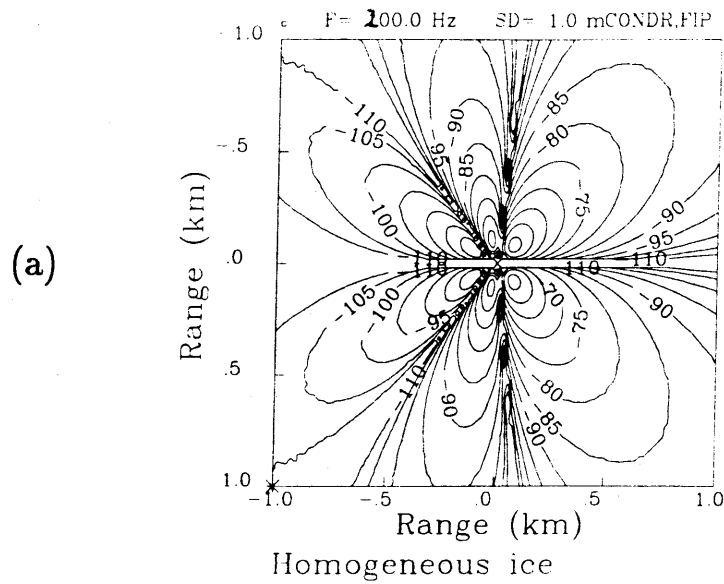


Figure 6.14: (a) Radiation pattern at $f = 200$ Hz, (b) synthetic time series for dip-slip with dip angle $\delta = 90^\circ$ in a central Arctic environment.

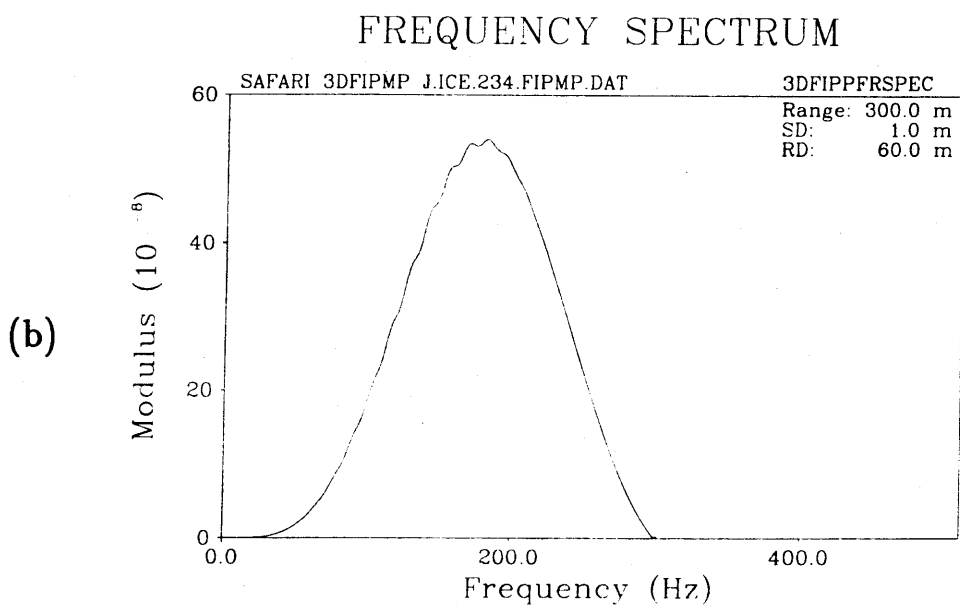
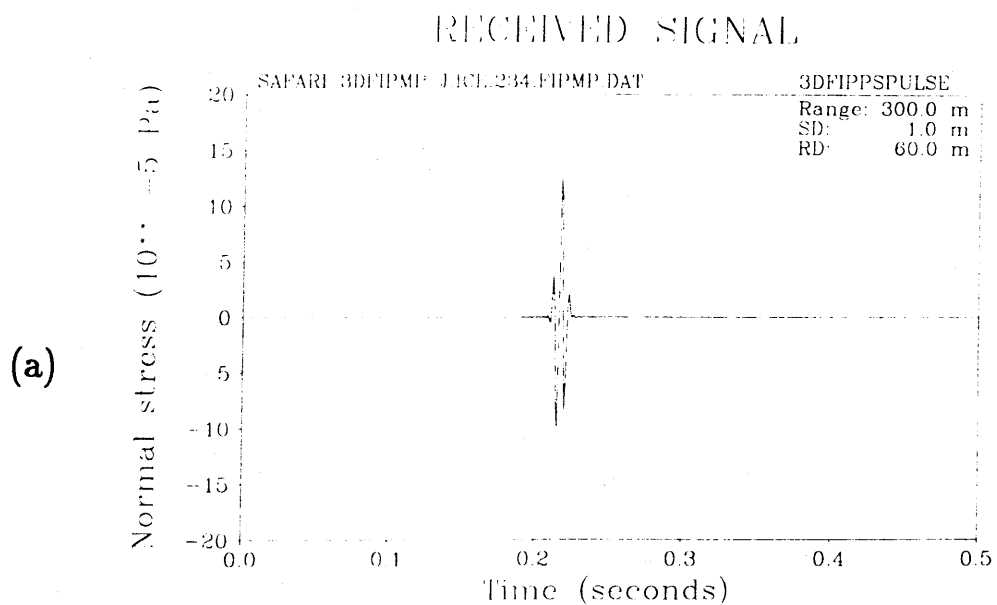
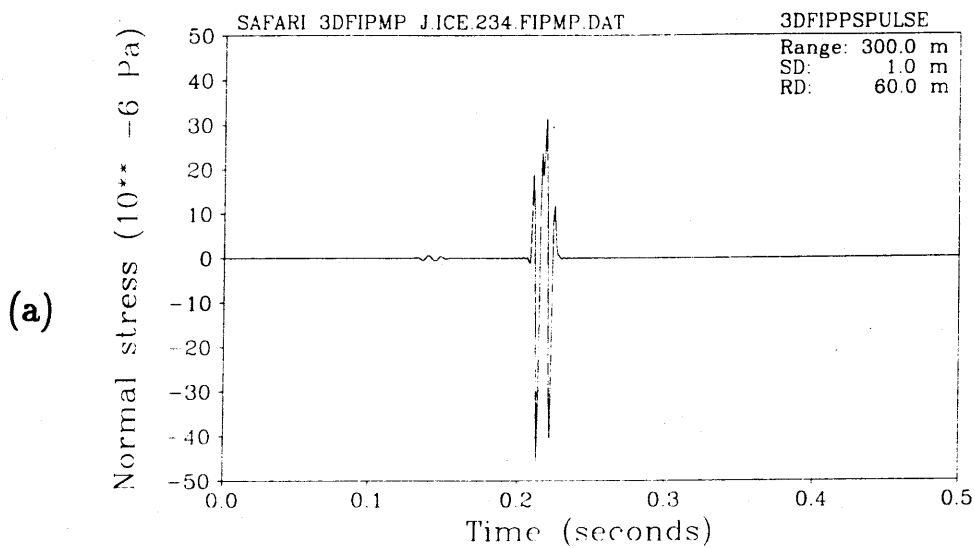


Figure 6.15: (a) Synthetic time series, and (b) spectrum, in the horizontal angle $\theta = 30^\circ$ for moving dip-slip

RECEIVED SIGNAL



FREQUENCY SPECTRUM

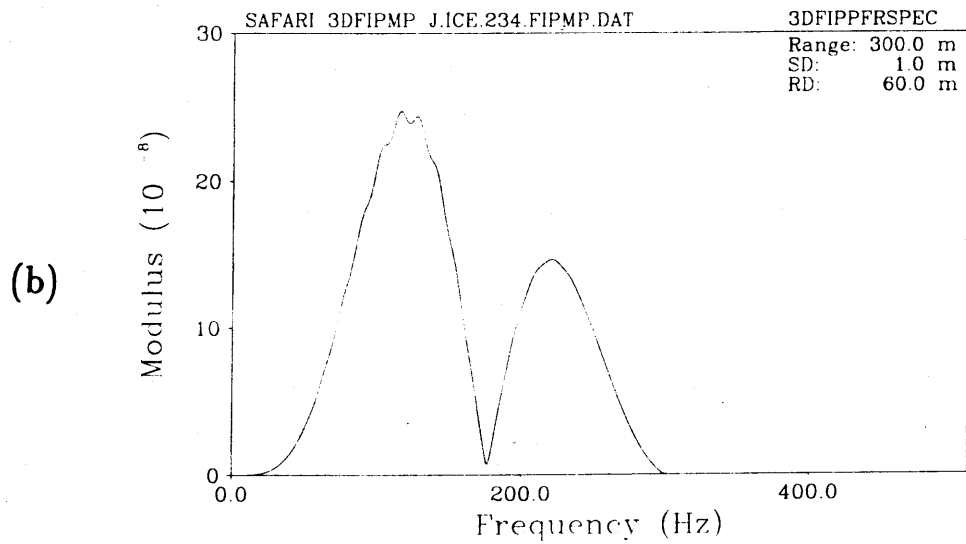


Figure 6.16: (a) Synthetic time series, and (b) spectrum, in the horizontal angle $\theta = 90^\circ$ for moving dip-slip

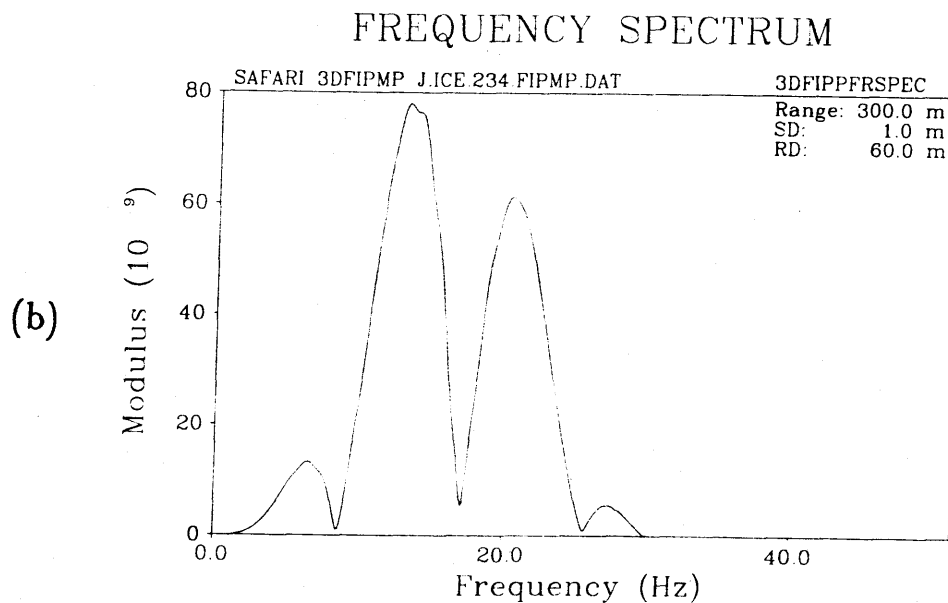
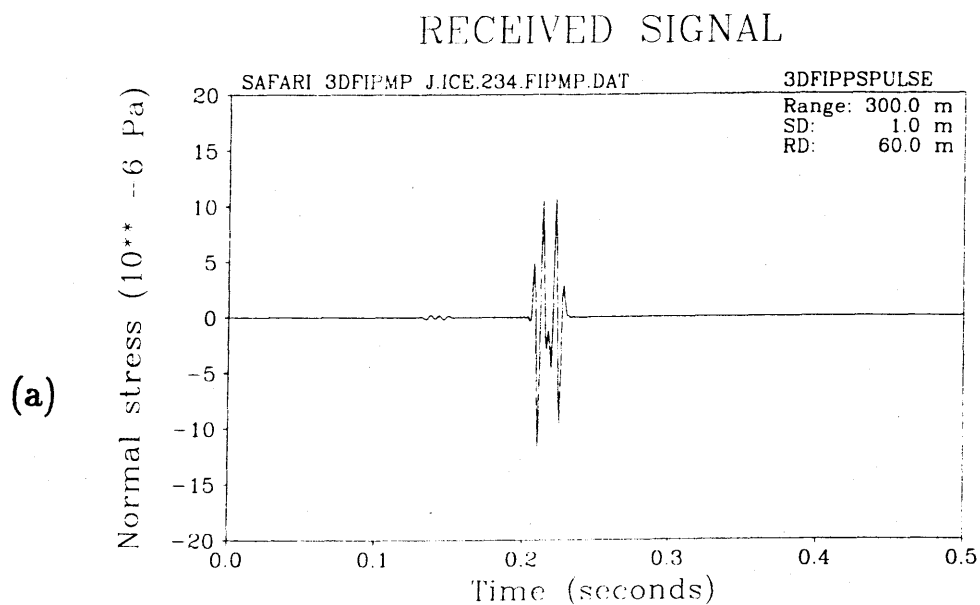


Figure 6.17: (a) Synthetic time series, and (b) spectrum, in the horizontal angle $\theta = 150^\circ$ for moving dip-slip

Savage and Mansinha [37] and considered as the stopping phase.

6.5 Parametric Study of Crack Radiation

In the previous sections 6.2 and 6.4, the radiation pattern and temporal characteristics have been studied for a set of source and environmental parameters. Source parameters include the modes of crack, fault orientation parameters, source depth, and crack propagation speed and dimension for moving cracks. The effect of the varying source parameters on the radiated field will be important to identify those source parameters, since the interpretation of observation can lead us to better understanding of the source mechanism.

In field observation of the acoustic radiation, the signal contains the information on the source mechanism. The information consists of the temporal and spectral characteristics for each spatial observation positions. The complete description of the field due to all source parameters can take up the rest of this thesis, therefore, only the qualitative description is briefly given. It is considered to be another research area to be studied for the source inversion techniques.

The effect of crack dimension on the directivity pattern is dependent on the frequency. The number of lobes in the real space is determined by the relative length of the crack dimension to the wave length. The spectral analysis of time series at spatially distributed sampling positions can be used to determine the frequency dependent directivity pattern giving the estimation of crack dimension. However, this problem may be more complicated by introducing other parameters. For example, the crack propagation speed might vary along the crack length, and the crack geometry can be complex. Although the theoretical synthesis of these source mechanisms by the present approach is possible, the inversion from the data may be a formidable task, unless the geometry of the

crack is known. These considerations could only be resolved by a controlled experiment, where the measurement of source parameters is possible. The design of an experiment is, therefore, proposed in Section 6.7

The effect of source depth has been discussed in Langley [23] using the vertical and horizontal forces based on the low frequency approximation. It shows that the importance of the force position can be generally neglected for low frequencies. For finite frequencies, however, the position of forces is important exciting different modes of waves in the ice plate. For example, the symmetric waves are likely to be excited when the source depth is in the neutral axis of the plate including the fluid loading. Similarly, the antisymmetric loading excites the antisymmetric modes more effectively. The orientation of fault surface has significant effect on the radiated field for the tensile and shear cracks as well as the point forces. The results for the varying fault orientation parameters are not given, but their effects can be found by running the developed numerical code. In fact, the inversion of the fault orientation parameters (refer to Fig 3.2) are calculated from the field observation using various inversion techniques in seismology.

For the finite frequencies, where the thickness of the ice is about the same order or greater than the wave lengths of the frequencies of interest, there exist higher modes of the symmetric and antisymmetric modes in the ice plate. In turn, each mode radiates into the water complicating the field. In higher frequencies, it is expected that the interface waves, such as Rayleigh and Stonely waves, propagate along the interfaces of vacuum-ice and ice-water interfaces. Since these waves are evanescent spreading cylindrically (amplitude $\sim \frac{1}{r}$), the field at the surfaces of ice plate is dominated by them in the long range propagation, unless there is scattering due to the rough surface of the ice plate.

Another environmental parameter which contains useful seismic information

is the anisotropy of the ice. The anisotropy of the ice is caused by the vertically oriented column of the ice separated by brine pocket, where the horizontal strength of the ice is greater than the vertical direction. The distinguishing characteristics of the transversely isotropic medium is the separation of SH and SV waves when traveling in the horizontal direction. This is discussed in the next section.

6.6 Anisotropy of Ice

The separation of SH and SV waves in the floating ice plate in the central Arctic ocean has been reported in Hunkins [16], and is contributed to the anisotropy of the ice. The anisotropy is caused by the structure of the ice, where the vertically oriented plates separated by brine brine pockets. Thus, any vertical shear stress would act along the many lines of weakness presented by the vertical brine pockets, but any horizontal shear stress would meet the resistance of the interlocking , randomly oriented grains. Indeed, the measurement of static ice strength shows that the lake ice as well as the sea ice are not isotropic [16].

The velocity of SV and SH waves vary considerably with a seasonal change, which is largely attributed to the variation of ice temperature affecting, again, the elastic constants. Although the measurement of the SH wave provides, when observed in the ice, the seismic properties of ice including some of the elastic constant, this wave can not be detected in the water because the SH wave is decoupled from the vertical displacement of ice, so that the water wave is not excited. Therefore, it is concluded that the SH wave does not radiate any energy into the water, and is trapped in the ice plate unless there is scattering from the rough surface.

The following examples for the isotropic and transversely isotropic media

will show that the effect of anisotropy of the sea ice. The compact tensile crack at $z = 1 \text{ m}$ with fault orientation parameters $\delta = 90^\circ$ and $\phi_s = 0^\circ$ will be considered.

Case 6.6 *Isotropic ice plate in the central Arctic environment* : This case is the same as the *Cases* 6.1 and 6.2, where the compressional and shear velocities are 3500 m/sec and 1800 m/sec , respectively. except that the receivers are now in the ice plate instead of water. Therefore, the field parameters are calculated for 3 components of the particle velocities(Fig 6.18). Also, the inverse Hankel transform integrands for each components of field parameters and Fourier orders are shown in Fig 6.21, where the solid line is for the isotropic ice plate and broken line for the anisotropic ice plate treated in the next *Case* 6.7.

Case 6.7 *Transversely isotropic ice plate in the central Arctic environment* : The source and environmental parameters are same as the *Case* 6.6, except that the ice plate is now transversely isotropic. The transversely isotropic ice plate consists of two layers. The compressional and shear velocities are 4000 m/sec and 2300 m/sec for the first layer, and 3000 m/sec and 1300 m/sec for the second layer, respectively. The synthetic time series for the 3 components of particle velocities are given in Fig 6.19. Also, the slowness surfaces for the existing waves are shown in Fig 6.20.

First, let us take a look at the synthetic time series for *Cases* 6.6 and 6.7. For the vertical displacements, *Case* 6.6(Fig 6.18(a)) shows that the earlier arrival of *SV* Waves of flexural waves (second arrival) compared to that of *Case* 6.7(Fig 6.19(a)). This is due to the slow *SV* waves in the transversely isotropic medium as can be seen in Fig 6.21. The peaks around 0.675 is the contribution from the *SV* waves. The phase speed is

$$c_{SV} = \frac{\omega}{k} \approx 930 \text{ m}. \quad (6.3)$$

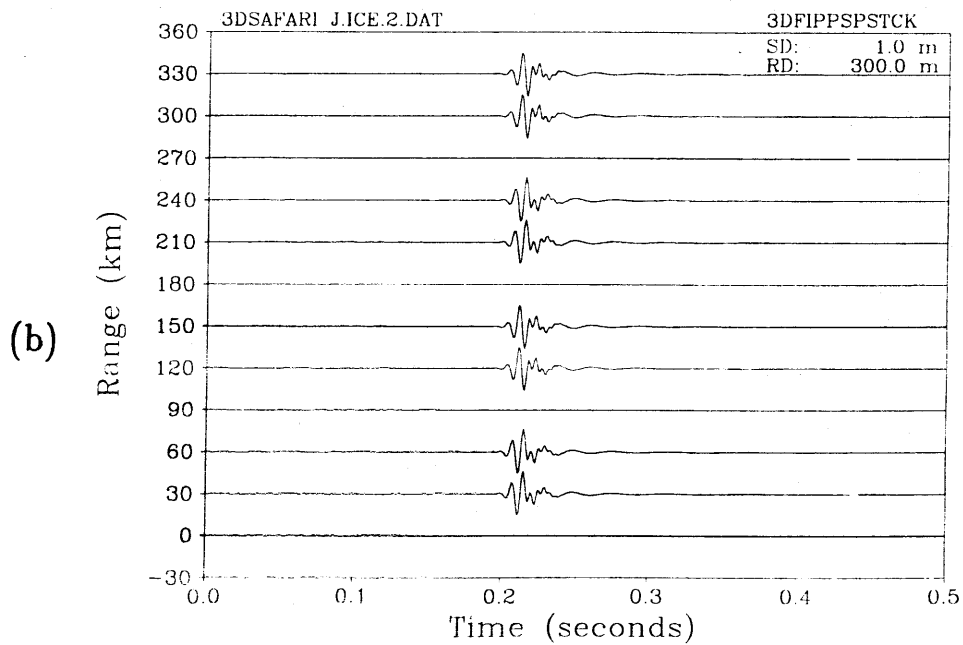
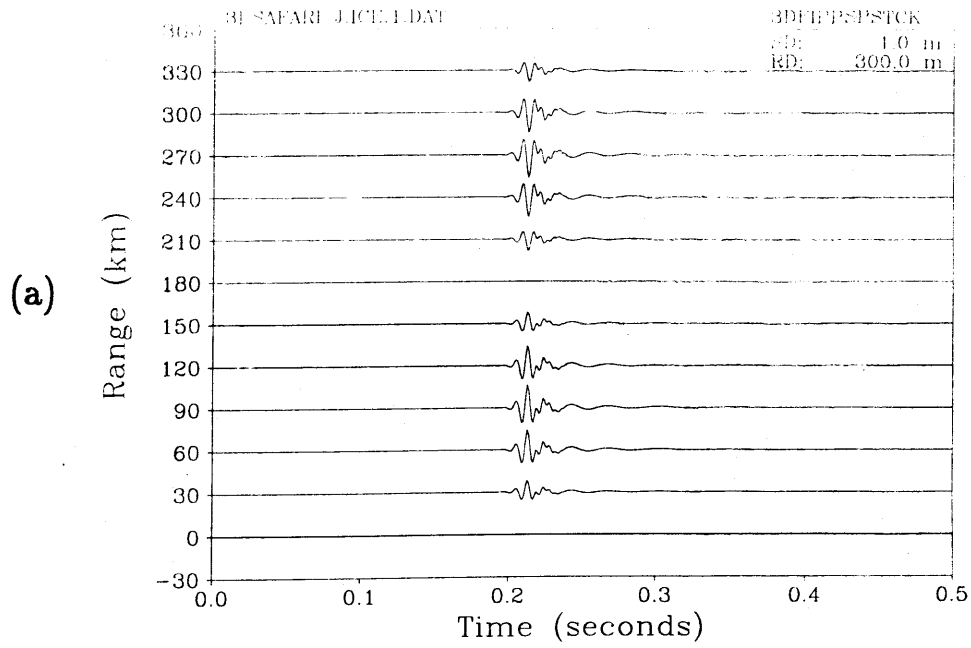


Figure 6.18: Synthetic time series in an isotropic ice plate in the central Arctic environment, (a) vertical displacement, (b) x-direction displacement.

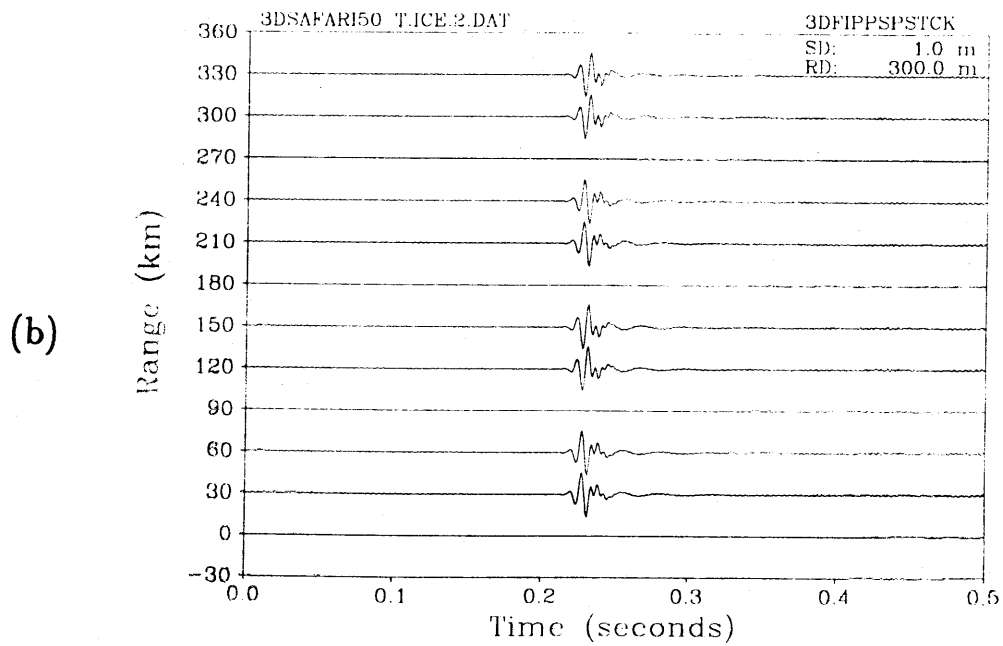
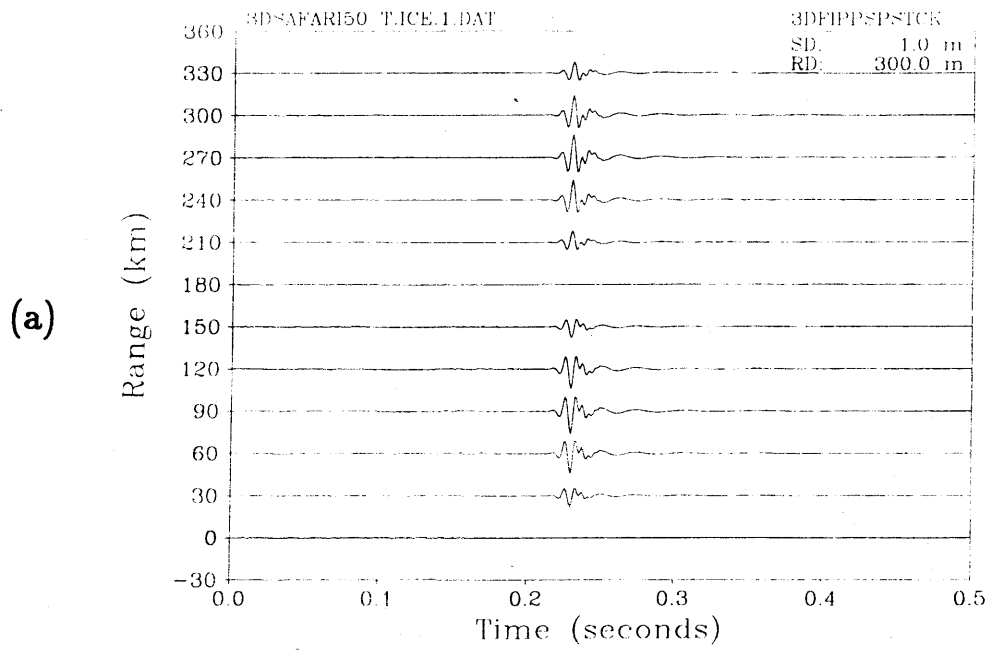


Figure 6.19: Synthetic time series in a transversely isotropic ice plate in the central Arctic environment, (a) vertical displacement, (b) x-direction displacement.

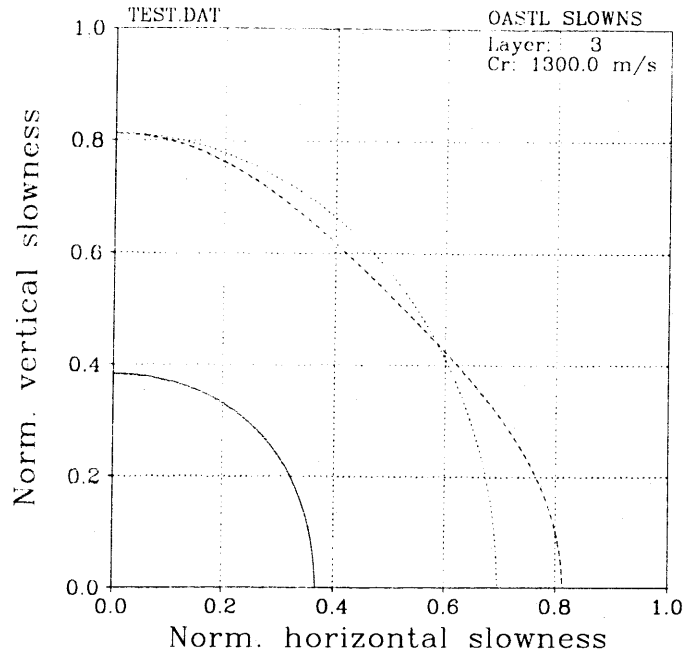


Figure 6.20: Slowness surface of P (solid line), SV (dotted line), and SH (dashed line) waves.

However, it is noted that the group velocity is much faster than the phase speed for the SV wave giving $\approx 1450 \text{ m/sec}$ from Fig 6.5, which explains the arrival time of approximately 0.212. The second peak of broken line in Fig 6.21(a) for the transversely isotropic ice plate represents SV wave in the transversely isotropic ice plate traveling slower than the SV wave in the isotropic ice plate. The second arrival in the synthetic time series in Fig 6.18(b) is the SH wave in the isotropic ice plate, which travels slightly slower than the SH wave in the transversely isotropic ice plate. This can be explained again from the position of the peaks for both media in Fig 6.21(d) and (f). The second peak with solid

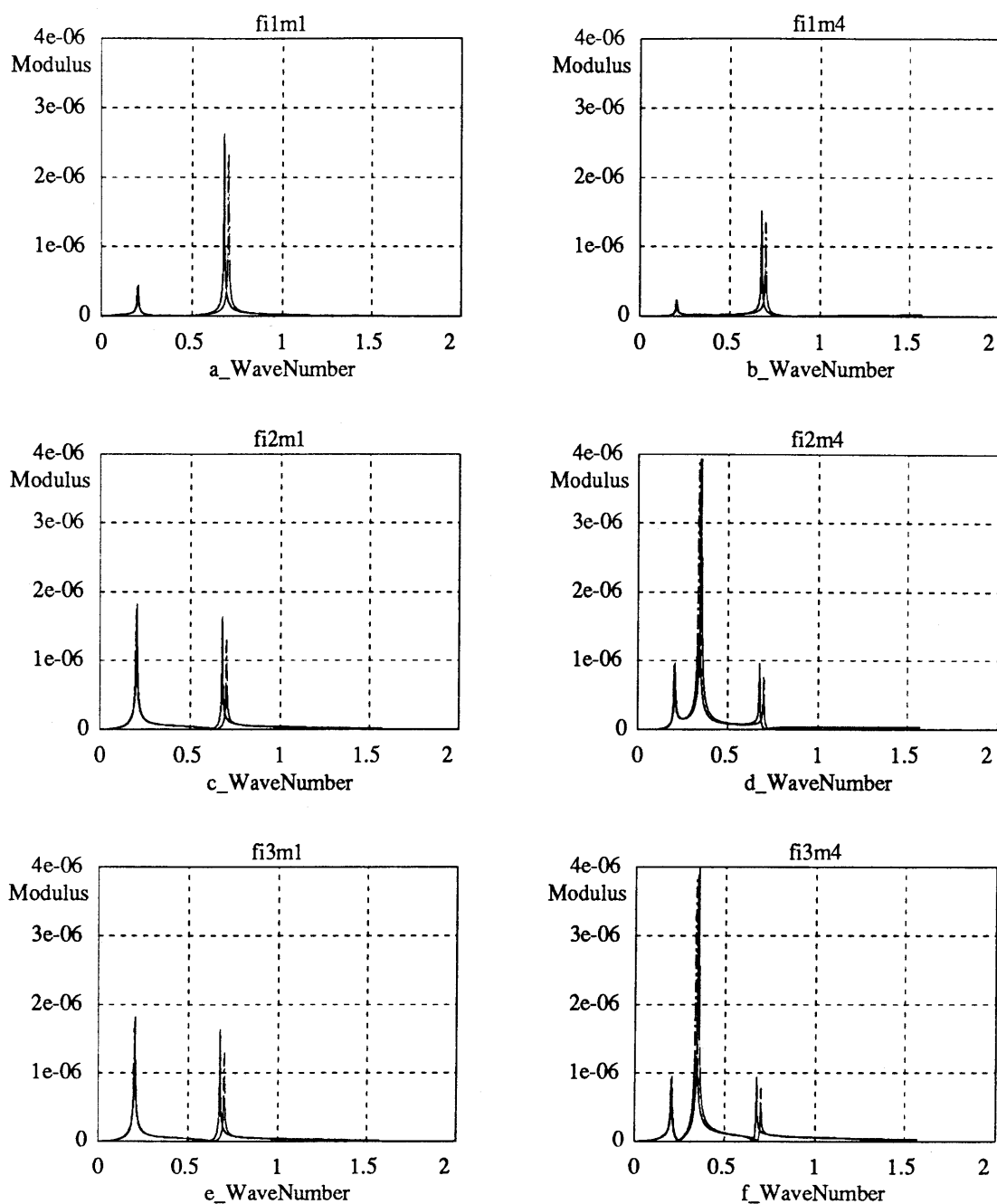


Figure 6.21: Modulus of Hankel transform integrand for isotropic medium (solid line), and transversely isotropic medium (dotted line), (a) and (b) show the vertical displacements for Fourier orders zero-th and $\cos 2\theta$ orders, respectively, (c) and (d) for the x -direction velocity, and (e) and (f) for the y -direction velocity.

line represents the wave number for the isotropic ice plate and that with broken line for the transversely isotropic ice plate, explaining earlier arrival of the SH wave in the transversely isotropic ice plate than that of the isotropic ice plate. The phase speed of the SH waves are

$$c_{SH} = \frac{\omega}{k} \approx 1800 \text{ m}, \quad (6.4)$$

which is almost the same as the medium SH wave speed of the ice (Fig 6.20). This is because the SH wave is completely decoupled from the waves existing in the water. The exact values of the phase speed of SH wave can be found in Fig 6.20 for the different directions of propagation.

The arrival of the compressional waves for both media (Fig 6.18 and 6.19) is not much affected as can be seen in Fig 6.21 for the modulus of Hankel integrand at the top of the ice.

6.7 Proposed Crack Radiation Experiment

In spite of the large amount of ambient noise data collected over the years, no data sets available are directly suited for studying the individual events to confirm existing crack radiation hypotheses. This is due to several factors including the limited spatial sampling imposed by economy and the fact that most experiments have focused on the low frequency, overall ambient noise, requiring large apertures. Also, the layout of sensors requires a certain arrangement suited for studying the radiation patterns from the sources. Therefore, in this section, a series of experiment, i.e. laboratory and field experiments, will be proposed.

The objective of the proposed laboratory and field experiments are

1. Laboratory Experiment

- Validation of model with the controlled sources.

- Development of inverse technique.

2. Field Experiment

- Source parameters inversion from the observed data including source location, crack type, crack dimension, and propagation speed.

The data obtained in the laboratory will be analyzed to show the radiation pattern in the ice and water, and used to test the existing analytical and numerical models. This will be done by investigating the directivity pattern as well as the temporal characteristics for different modes of cracking or different forcing mechanisms. Also, the effects on the pressure field in the water of the non-compactness of a source with finite crack propagation speed in the floating ice sheet will be studied. It is the expected outcome of this proposed experiment to develop the inversion techniques from the known source parameters and the observed data. Once the spectral and temporal characteristics of each fracture modes are identified by fitting data through our analytical models, these models can be applied to the data collected in the central Arctic environment in various field experiments. For example, radiation patterns for each mode of cracking can be used to identify which modes of cracking are dominant, and how they radiate energy into water in the central Arctic environment. Thus, better understanding of the individual crack radiation events can lead us to refined Arctic Ocean ambient noise model.

The model developed in this research served as a guide to design the experiment and gives ideas about what is to be sought from the analysis of data. The idea is to relate the characteristics of the observed data to the features predicted by the model, yielding the source parameters of the event. The source parameters thus obtained are directly related to the physical source mechanisms. Following are discussions about what aspects are to be sought from the data.

The details of these aspects are found in the sections 6.2, 6.3, and 6.4.

In the frequency domain, the spectral level at each spatially distributed sensor is plotted to display the directivity pattern at each frequency. This will be done for a known mode of cracking with crack parameters such as dimension, direction and propagation speed. This directivity can be used to identify the source type and crack size effect. This methodology has been developed and widely used in seismology. Also the slope of roll-off in spectrum for each sensor location can be used for identifying the source time series. The temporal characteristics, including the duration of observed signal and the stopping phase, can be related to the dimension of the crack.

6.7.1 Laboratory Experiment

In order to investigate the crack radiation problem, it is necessary to minimize scattering due to rough surface, pre-existing cracks, or ridges so as to concentrate on the source inverse problem. In the Arctic Ocean, scattering due to inhomogeneity of the ice such as rough surfaces, pre-existing cracks and ridges are complicating factors obscuring the crack radiation problem. It is therefore essential initially to perform a laboratory experiment which eliminates these complicating factors.

The laboratory experiment should include direct measurement of crack parameters, such as size, propagation speed and direction. Crack size and direction can be observed after the event, however the propagation speed is hard to measure because of its highly transient nature. Here, a high speed camera could be used provided that the precise position and time of crack formation is known. Another way is to measure the time history of the displacement along and across the crack, e.g. by means of accelerometers or strain gauges.

Inducing a desired mode and size of crack without interfering with the wave

field is difficult, and is another research area being studied ³. Although the mechanical properties of ice are rather complex, it is known that the ice is much stronger in compression than in tension. It is possible that this fact may be exploited. In order to ensure the crack is formed at the desired position with certain direction, the prescribed crack surface is cut so as to reduce the cross sectional area. These aspects of inducing different modes of cracks can be found in the ice mechanics literature[8].

The field parameters to be observed include the pressure in the water as well as the displacement in the ice plate. Since the ice is an elastic plate, supporting a large number of Lamb modes, it is expected that valuable information concerning the cracking process can be obtained by measuring the ice motion in addition to the sound field in the water. The other observables are the crack parameters, such as the volume expansion for tensile cracks, the seismic moment for shear cracks, the dimension of the crack, and the crack propagation speed. These crack parameters can be best observed by measuring the particle motion at the vicinity of the crack surface. In order to measure the time history of displacement at the crack surface, it is suggested to use high speed camera with a resolution enough to observe the moving crack tip. Another way is to place the accelerometers or strain gauges along the prescribed crack allowing for localization of the moving crack tip.

Temporal Sampling

The sampling frequency of the sensors is determined based on the size of the crack to be induced, since we are looking at the radiation pattern of non-compact source. Non-compactness of the crack is determined by the size of the crack relative to the wave length. The non-compact source has phase interference due

³Discussion with Professor T. Wierzbicki

to its finite size of source distribution. This spectral behavior of the pressure field (or, stress field in the ice) show the periodic nulls and peaks depending on the frequency, which is called *frequency dependent directivity*. In order to identify this behavior, the observation of data with high Nyquist frequency is necessary. For this purpose, the sampling frequency of 10 KHz is suggested. Above approximately 10 KHz, the assumption of homogeneity of ice does not hold, since the roughness and grain sizes are greater than the wave length.

Spatial sampling

Although the presently developed solution technique is not restricted to the far field, the far field measurement have some advantages in applying to the average ambient noise, so that it is recommended to place the receivers and accelerometers in the far field. If the sensors are in the near field, the radiation pattern will be range dependent so that the directivity pattern is hard to identify. Moreover, most analytical solutions are valid only in the far field. Conditions for the far field approximation are $l \ll r$ for amplitude, and $\frac{kl^2}{8r} \leq \frac{\pi}{4}$ for phase, where r is the distance from crack to observation point. These conditions reduces to

$$l \ll r \quad (6.5)$$

$$\frac{kl^2}{2\pi} = \frac{l^2 f}{c} \leq r, \quad (6.6)$$

where c is the medium phase speed, f is the frequency of interest, k is wave number, l is the crack dimension, and r is the receiver range.

Based on the considerations presented in the previous sections, it is recommended that the spatial sampling is at every 30° at least in the horizontal and vertical directions to identify the spatial directivity due to the compact directional sources, as well as the frequency dependent directivity due to the moving

cracks.

Design Of Array Of Sensors

Based on the considerations presented in the previous sections, an array design will be proposed. To measure the displacement field in the ice, 16 tri-axial accelerometers need to be placed in the ice (Fig 6.22). The distance from the crack to the accelerometers r is recommended to be as large as the dimension of the laboratory allows, so that the longitudinal and flexural modes in the ice plate can be observed separately. When the accelerometers are placed at $r \approx 150\text{ m}$, the 10 Hz frequency components will be separated by a time delay of one wave length traveling time, i.e. 0.1 seconds (refer to Fig 6.5), for flexural mode. Similarly, a time delay of 10 wave lengths of traveling time will be achieved for the 100 Hz frequency component. If the distance, r , is 15 m, the separation time will be reduced by a factor of 10. When the separation of existing modes is critical, the scaled experiment with artificial is suggested to reduce the size of laboratory. Alternatively, the lake ice can be used, where the sensors are placed far enough to separate the different modes.

To measure the pressure field in the water, 20 hydrophones are to be suspended in the water (Fig 6.23). The hydrophones can be placed about same distance as the accelerometers in order to separate the longitudinal mode from the acoustic mode. The depth of hydrophones, however, need to be greater than half the wave length at the frequency of interest, so that the flexural wave does not interfere with the other modes. For example, when the frequency of interest is 100 Hz, the depth of hydrophones should be greater than $d \approx 3.5\text{ m}$.

The crack parameters are found from the time history of the particle motion at the crack surface. To measure the displacement along and cross the crack, tri-axial accelerometers are placed as indicated in Fig 6.24. As mentioned earlier,

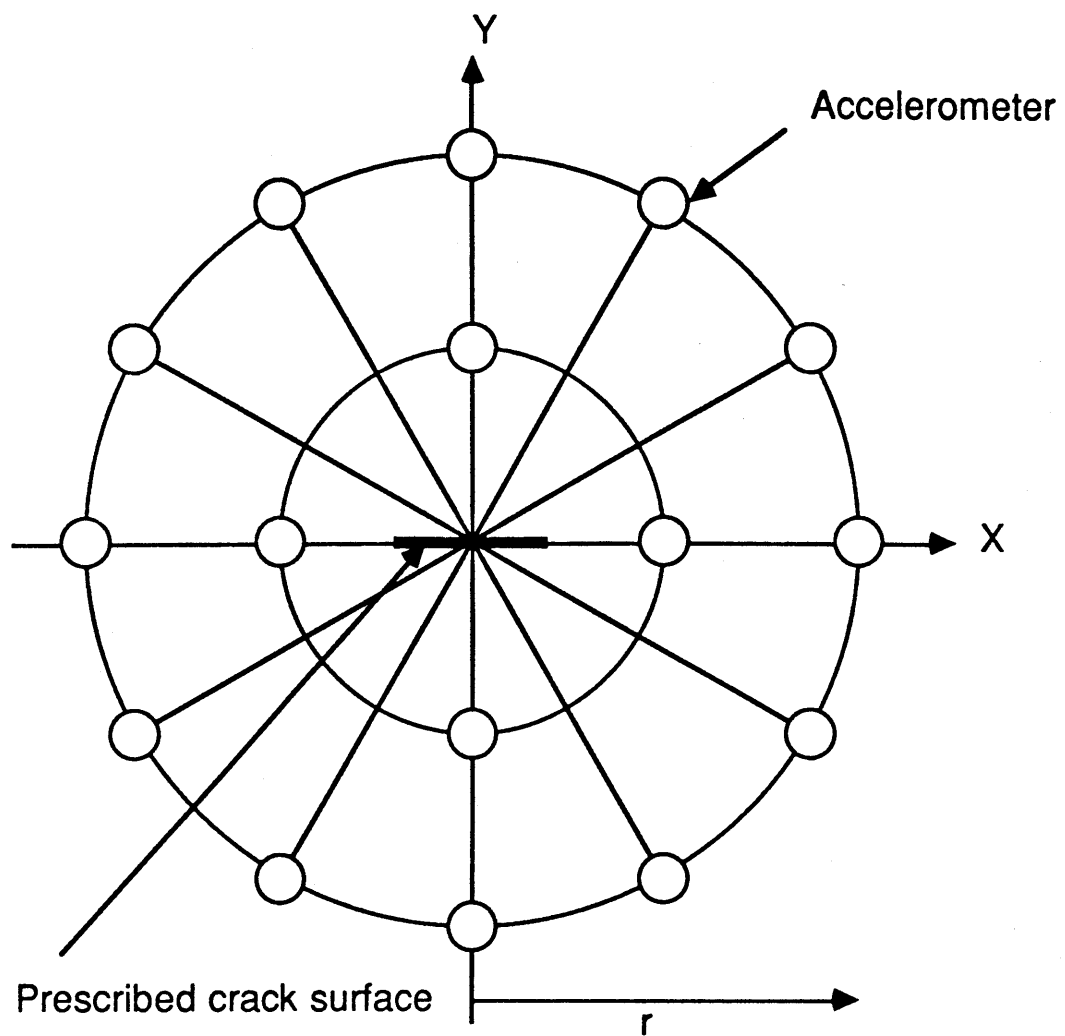


Figure 6.22: Top view of an array of accelerometers in the ice.

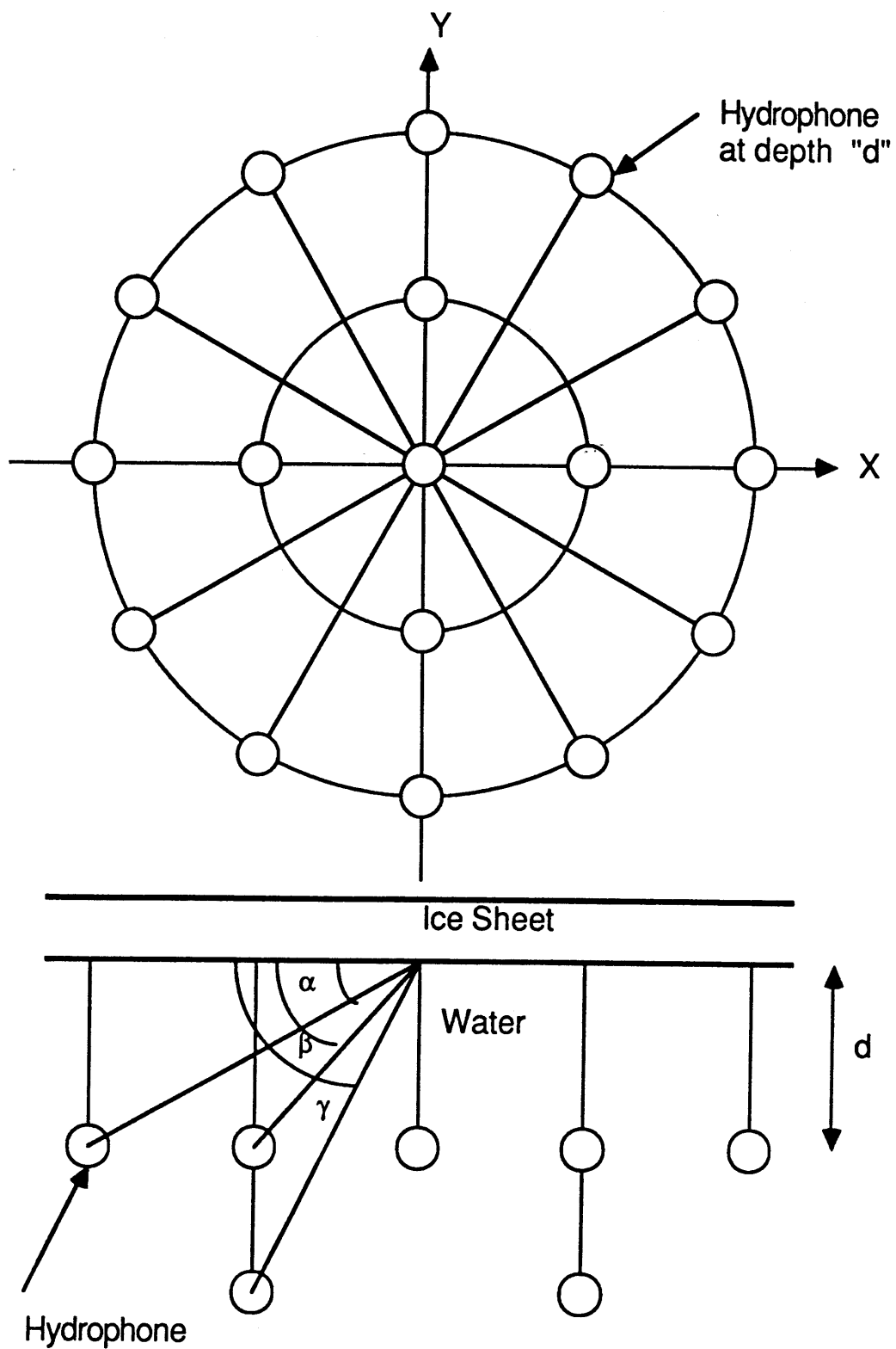


Figure 6.23: (a) Top view of hydrophone array and (b) Cross section along x -axis.

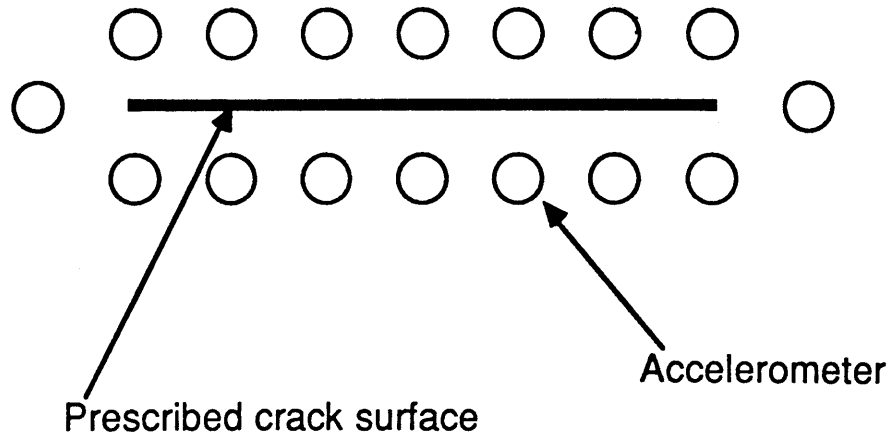


Figure 6.24: Tri-axial accelerometers placed along the prescribed crack surface to measure the displacement along and across the crack surface.

a high speed camera is recommended along with the accelerometers.

6.7.2 Field Experiment

Once the controlled experiment in the laboratory is carried out, and the features of the data are properly explained and matched with the model developed, a field experiment should be performed. The difference between the laboratory and field experiment will be the randomness of the event. The likelihood of observing events within the circular array of radius 300 m , in which we can obtain data points in all directions, can be estimated from previous experiments.

For example, in the FRAM IV study [44], it has been shown that for the center annulus of 30 square Km, there were 91 events per 30 square Km per 662 minutes of observation, or approximately 0.3 events per square Km per hour. Since our circular array has 0.28 square Km, we expect about 0.1 events per hour within the circular array. Therefore, the expected duration of the experiment should be 10 Hrs to observe an event within the circle. However, since the signal to noise ratio of an event depends on the distance from the event to the hydrophones, we might observe more events in the small circular area enclosed by an array of hydrophones.

6.8 Conclusion

The developed model has been applied to the various examples to demonstrate the solution technique, and to find a number observations for the radiation pattern and temporal characteristics depending on the source and environmental parameters. The source parameters can be the types of source, or mode of crack, dimensions of crack as well as geometry (fault surface orientation parameters λ, ϕ, δ , refer to Fig 3.2), propagation speed and, source depth. Among the environmental parameters, the parameters of importance are thickness of the plate, the mechanical properties of the medium, such as the anisotropy and inhomogeneity. The change of the radiation pattern, and temporal and spectral characteristics are discussed.

First, the radiated field from the three types of fracture show the distinct directivity pattern when observed in the water, depending on the fault orientation parameters. The presence of the ice-water interface, coupling the P and SV waves, complicates the radiation pattern as well as the time series separating the contributions from the radiation of different modes existing in the ice plate.

The relative strength between the radiation from the acoustic, antisymmetric, and symmetric modes in the ice plate for the three types of fracture is used to infer the most probable source types and corresponding dip angle based on the observation that the acoustic mode is much stronger than the radiation from the longitudinal wave in the ice plate. It is found that the shear cracks, i.e. dip-slip with dip angle $\delta \approx 0^\circ$ and 90° and strike-slip with dip angle $\delta \approx 0^\circ$, are the most probable source types. The corresponding source strength is related to the field pressure in terms of the seismic moment and the average displacement over specified fault surface area.

The temporal characteristics of the non-compact and propagating crack can be characterized as the modulated signal, of which cross-correlation between channels (receiver positions) are very poor. Another noticeable result is the rapid change of directivity in the varying angle. The larger the dimension of the crack is, the more peaks and nulls of the radiation pattern appears to give rapid variation with angle.

Next, the effect of anisotropy of the sea ice is discussed. The sea ice is shown to be anisotropic, where the SH and SV waves separates. The additional mode existing due to anisotropy, however, does not affect the radiation pattern, since the SH wave in the ice plate does not excite the vertical displacement at the ice-water interface so that the water wave is decoupled from the SH wave.

The sources in the ice plate as an element of Arctic ambient noise can contribute to the average noise either as the direct radiation or as the scattered field due to the inhomogeneity and rough boundary of the ice. In certain frequencies, the different types of crack modes, or physical mechanism can be important. Further, the ambient noise forming process in other frequency regimes may be completely different, as well as the responsible environmental stresses. The application of this model, therefore, should be made with the careful physical

insights to the overall ambient noise frequencies as well as the corresponding generation mechanisms and driving forces.

Chapter 7

Conclusions

7.1 Summary

The summary of this thesis emphasizing the original contributions can be made under two categories. One is the development of the efficient numerical algorithm as well as the corresponding solution techniques for radiation from the compact and non-compact directional seismic sources in a laterally stratified medium, combining the existing numerical code (SAFARI) with source representation in an unbounded medium. The compact source representation by Keilis-Borok (1950), reviewed in Sato [36], is treated in Chapters 2, and serves, in nature, as tutorial and background for the further development in the Chapter 3. In Chapter 3, which is the kernel of this thesis, the representation of seismic sources is extended to the formulation of tensile crack in addition to the shear fault formulation, and transformed to the cylindrical coordinates and arranged in such a way that the formulation can be applicable to the global matrix method. Consequently, the source terms are incorporated into the global matrix method, treating the multiple azimuthal Fourier orders simultaneously. In Chapter 4, the superposition model to treat the radiation from non-compact

array and propagating crack model taking advantage of numerical method, also, has been developed eliminating the numerical inefficiency and convergence problems caused by the expansion of the field with Bessel function[38]. This non-compact model is of great practical importance with potential applications to the radiation from an array of airgun or explosions for seismic exploration and propagation. Another problem treated in Chapter 5 is the propagation effect of the transversely isotropic medium, of which applications are found in the sea and lake ice, and the periodic finely layered sediment. Since the theory for the transversely isotropic medium is well established, the focus is on the formulation of the compatible boundary conditions with the global matrix approach.

The other category is the outcome of the application of the developed model to the physical system. The developed model is basically applied to the canonical problems and to the environmental model of the central Arctic. In Chapter 3, the canonical examples of radiation from the three different modes of crack in an homogeneous unbounded medium are discussed. The spatial and temporal characteristics of the radiated field are distinctively different for the three modes of crack, i.e. tensile crack, dip-slip, and strike-slip. The detailed discussions are given in Chapter 3.5. The application of non-compact and propagating crack model is found in Chapter 4, where the radiated field are characterized by the frequency dependent directivity pattern, and the temporal characteristics include the existence of the stopping phase, the modulation of signal by the dimension of the crack surface, and poor cross correlation due to the phase interference due to the crack dimension. The results of the application to the central Arctic environment shows more complications introduced by a wave guide in addition to the general characteristics mentioned above for the canonical problems. The coupling of the P and SV waves at the ice-water interface introduces the dispersion of each components of waves, and the corresponding radiated field in

the water. For the directional sources, the SH wave is excited and trapped in the ice plate, since the SH wave decouples from the P and SV waves and there exists only the P wave in the water. When the rough boundary with scattering effect is considered, the contribution of the scattered field from SH and SV to the average ambient noise could be significant, of which effect needs to be studied in a organized way. Finally, the effect of anisotropy of the ice reported by Hunkins[16] is simulated to give the separation of the SV and SH waves, which contains the information on the elastic constants in different directions as well as the dispersion relation for the given geometry.

7.2 Discussions and Suggestions for Future Studies

Solution Techniques

The applicability of presently developed solution technique is limited to the range independent medium, which is often referred as the laterally stratified medium, the vertically varying medium, or the laterally homogeneous medium. This environmental model is of the great practical importance for many physical problems, such as the seismic propagation and underwater acoustic propagation, where the medium can be treated as laterally homogeneous. As the more accurate modeling becomes necessary, the laterally inhomogeneous medium needs to be modeled, especially for high frequencies where the effect of the local inhomogeneity is significant, of which example can be found in the scattering from the ridges in the central Arctic environment affecting the directly observed signal as well as the average ambient noise as result of long range scattering effect.

Applications

Application of the developed code can be found in seismology as well as in underwater acoustics. The applications include the seismic exploration, the field solution to the radiation from the sonar, and the design of the efficient volume transducer array with focusing and steering. For given environment, the source discrimination can be made from the spectral and temporal characteristics of the observed data.

As a source inverse problem, the developed code can be instrumental in studying the source mechanisms of fracture in the floating ice plate in the central Arctic environment as an element of the average ambient noise. The directivity pattern of the compact and non-compact fracture and the temporal characteristics including the dispersion and separation of different modes existing in the ice plate as well as the field in the water for different types of fracture have been found to be readily applicable to a proper set of data. For continuing research effort, controlled crack radiation experiment is proposed in Chapter 6.6 and given with some insights to the layout and the measurement of field parameters based on the preliminary outcome of the model. The experiment will be used in identifying the dominant crack mechanisms, the radiation and propagation effects that might be important for different environment. The broader issues, to which the developed model and crack radiation experiment is instrumental in relation to the central Arctic ambient noise, are

- in what frequency band is the crack radiation most important ?
- what other mechanisms are dominant in other frequencies ?

Regarding to the first question, only the field observation can be source of information that leads to the answer. Again, the problem is complicated by the varying environment, which modifies the natural frequencies of the environmental system. However, the properly scaled and conditioned experiment and

analysis is the most probable candidate as means of the answering the raised questions.

Therefore, it is concluded that two lines of research be pursued towards better understanding of the crack radiation. First relates the proper modeling of the physical system, as being undertaken by many researchers. These include the propagation effect in the range dependent environment including scattering, and other kinds of sources, such as gravity waves at extreme low frequency, radiation and propagation at high frequency where the medium can no longer be treated as homogeneous, and so on. Second, the experimental approach using the field and laboratory data should be used to define the dominant mechanisms as well as confirm the prediction made by modeling, which will eventually lead to better understanding of the physical mechanism and to constructing a model to predict the necessary informations.

Appendix A

Potentials, Displacements and Stresses of Various Sources with an Arbitrary Direction in Cylindrical Coordinates

The potentials, displacements and stresses caused by various sources are presented in this section. The potentials are related to displacements in the following manners.

$$\mathbf{u} = \nabla\phi + \nabla \times \nabla \times (\psi_r, \psi_\theta, \psi_z) \quad (\text{A.1})$$

$$= \nabla\phi + \nabla \times \nabla \times (0, 0, \Lambda) + \nabla \times (0, 0, \psi) \quad (\text{A.2})$$

The potentials are summed over each Fourier order m , where the m -th order are denoted by superscript m . Using the potentials defined in Eq A.1, the potentials are

$$\phi(r, \theta, z) = \sum_{m=0}^{\infty} \phi^m(r, z) \begin{bmatrix} \cos m\theta \\ \sin m\theta \end{bmatrix}$$

$$\begin{aligned}
\Lambda(r, \theta, z) &= \sum_{m=0}^{\infty} \Lambda^m(r, z) \begin{bmatrix} \cos m\theta \\ \sin m\theta \end{bmatrix} \\
\psi(r, \theta, z) &= \sum_{m=0}^{\infty} \psi^m(r, z) \begin{bmatrix} \sin m\theta \\ -\cos m\theta \end{bmatrix}
\end{aligned} \tag{A.3}$$

Using the definition in Eq A.2, the potentials are

$$\begin{aligned}
\phi(r, \theta, z) &= \sum_{m=0}^{\infty} \phi^m(r, z) \begin{bmatrix} \cos m\theta \\ \sin m\theta \end{bmatrix} \\
\psi_r(r, \theta, z) &= \sum_{m=0}^{\infty} \psi_r^m(r, z) \begin{bmatrix} \cos m\theta \\ \sin m\theta \end{bmatrix} \\
\psi_\theta(r, \theta, z) &= \sum_{m=0}^{\infty} \psi_\theta^m(r, z) \begin{bmatrix} \sin m\theta \\ -\cos m\theta \end{bmatrix} \\
\psi_z(r, \theta, z) &= \sum_{m=0}^{\infty} \psi_z^m(r, z) \begin{bmatrix} \cos m\theta \\ \sin m\theta \end{bmatrix}
\end{aligned} \tag{A.4}$$

A.1 Point Force in an Arbitrary Direction

Denoting the force vector $\mathbf{F} = F_x \mathbf{e}_x + F_y \mathbf{e}_y + F_z \mathbf{e}_z$ as a source term, the potentials and the field parameters are as follows.

Potentials

$$\phi = \frac{e^{i\omega t}}{4\pi\rho\omega^2} \int_0^\infty \begin{bmatrix} F_z \zeta \alpha J_0(sr) \\ + F_x \cos \theta s J_1(sr) \\ + F_y \sin \theta s J_1(sr) \end{bmatrix} e^{-\alpha|z-z_*|} \frac{s}{\alpha} ds$$

$$\Lambda = \frac{e^{i\omega t}}{4\pi\rho\omega^2} \int_0^\infty \begin{bmatrix} F_z J_0(sr) \\ + F_z \zeta \frac{\beta}{s} \cos \theta J_1(sr) \\ + F_v \zeta \frac{\beta}{s} \sin \theta J_1(sr) \end{bmatrix} e^{-\beta|z-z_*|} \frac{s}{\beta} ds$$

$$\psi = \frac{e^{i\omega t}}{4\pi\rho\omega^2} \int_0^\infty \begin{bmatrix} F_z \frac{k^2}{s} \sin \theta J_1(sr) \\ - F_v \frac{k^2}{s} \cos \theta J_1(sr) \end{bmatrix} e^{-\beta|z-z_*|} \frac{s}{\beta} ds$$

Displacements and stresses

For zeroth order,

$$w^m(r, z) = \frac{e^{i\omega t}}{4\pi\rho\omega^2} \int_0^\infty \begin{bmatrix} -F_z \alpha e^{-\alpha|z-z_*|} \\ + F_z \frac{s^2}{\beta} e^{-\beta|z-z_*|} \end{bmatrix} J_0(sr) s ds$$

$$u^m(r, z) + v^m(r, z) = \frac{e^{i\omega t}}{4\pi\rho\omega^2} \int_0^\infty \begin{bmatrix} -F_z \zeta s e^{-\alpha|z-z_*|} \\ + F_z \zeta s e^{-\beta|z-z_*|} \end{bmatrix} J_1(s) ds$$

$$u^m(r, z) - v^m(r, z) = \frac{e^{i\omega t}}{4\pi\rho\omega^2} \int_0^\infty \begin{bmatrix} F_z \zeta s e^{-\alpha|z-z_*|} \\ - F_z \zeta s e^{-\beta|z-z_*|} \end{bmatrix} J_{-1}(sr) s ds$$

$$\sigma_{zz}^m(r, z) = \frac{e^{i\omega t}}{4\pi\rho\omega^2} \mu \int_0^\infty \begin{bmatrix} F_z (2s^2 - k^2) e^{-\alpha|z-z_*|} \\ - F_z \zeta 2s^2 e^{-\beta|z-z_*|} \end{bmatrix} J_0(sr) s ds$$

$$\sigma_{rz}^m(r, z) + \sigma_{\theta z}^m(r, z) = \frac{e^{i\omega t}}{4\pi\rho\omega^2} \mu \int_0^\infty \begin{bmatrix} 2F_z \alpha s e^{-\alpha|z-z_*|} \\ - F_z \frac{s}{\beta} (2s^2 - k^2) e^{-\beta|z-z_*|} \end{bmatrix} J_1(sr) s ds$$

$$\sigma_{rz}^m(r, z) - \sigma_{\theta z}^m(r, z) = \frac{e^{i\omega t}}{4\pi\rho\omega^2} \mu \int_0^\infty \begin{bmatrix} -2F_z \alpha s e^{-\alpha|z-z_*|} \\ + F_z \frac{s}{\beta} (2s^2 - k^2) e^{-\beta|z-z_*|} \end{bmatrix} J_{-1}(sr) s ds$$

For $\cos \theta$ order,

$$w^m(r, z) = \frac{e^{i\omega t}}{4\pi\rho\omega^2} \int_0^\infty \begin{bmatrix} -F_z \zeta s e^{-\alpha|z-z_*|} \\ + F_z \zeta s e^{-\beta|z-z_*|} \end{bmatrix} J_1(sr) s ds$$

$$u^m(r, z) + v^m(r, z) = \frac{e^{i\omega t}}{4\pi\rho\omega^2} M_0 \int_0^\infty \begin{bmatrix} -F_z \frac{s^2}{\alpha} e^{-\alpha|z-z_*|} \\ + F_z \frac{s^2}{\beta} e^{-\beta|z-z_*|} \end{bmatrix} J_2(sr) s ds$$

$$\begin{aligned}
u^m(r, z) - v^m(r, z) &= \frac{e^{i\omega t}}{4\pi\rho\omega^2} \int_0^\infty \left[\begin{aligned} &F_x \frac{s^2}{\alpha} e^{-\alpha|z-z_*|} \\ &+ F_x \frac{k^2 - \beta^2}{\beta} e^{-\beta|z-z_*|} \end{aligned} \right] J_0(sr) s ds \\
\sigma_{zz}^m(r, z) &= \frac{e^{i\omega t}}{4\pi\rho\omega^2} \mu \int_0^\infty \left[\begin{aligned} &-F_x \frac{s}{\alpha} (k^2 - 2s^2) e^{-\alpha|z-z_*|} \\ &-2F_x \beta s e^{-\beta|z-z_*|} \end{aligned} \right] J_1(sr) s ds \\
\sigma_{rz}^m(r, z) + \sigma_{\theta z}^m(r, z) &= \frac{e^{i\omega t}}{4\pi\rho\omega^2} \mu \int_0^\infty \left[\begin{aligned} &2F_x s^2 \zeta e^{-\alpha|z-z_*|} \\ &-2F_x s^2 \zeta e^{-\beta|z-z_*|} \end{aligned} \right] J_2(sr) s ds \\
\sigma_{rz}^m(r, z) - \sigma_{\theta z}^m(r, z) &= \frac{e^{i\omega t}}{4\pi\rho\omega^2} \mu \int_0^\infty \left[\begin{aligned} &-2F_x \zeta s^2 e^{-\alpha|z-z_*|} \\ &+ 2F_x \zeta \beta^2 e^{-\beta|z-z_*|} \end{aligned} \right] J_0(sr) s ds
\end{aligned}$$

For $\sin \theta$ order,

$$\begin{aligned}
w^m(r, z) &= \frac{e^{i\omega t}}{4\pi\rho\omega^2} \int_0^\infty \left[\begin{aligned} &-F_y \zeta s e^{-\alpha|z-z_*|} \\ &+ F_y \zeta s e^{-\beta|z-z_*|} \end{aligned} \right] J_1(sr) s ds \\
u^m(r, z) + v^m(r, z) &= \frac{e^{i\omega t}}{4\pi\rho\omega^2} M_0 \int_0^\infty \left[\begin{aligned} &-F_y \frac{s^2}{\alpha} e^{-\alpha|z-z_*|} \\ &+ F_y \frac{s^2}{\beta} e^{-\beta|z-z_*|} \end{aligned} \right] J_2(sr) s ds \\
u^m(r, z) - v^m(r, z) &= \frac{e^{i\omega t}}{4\pi\rho\omega^2} \int_0^\infty \left[\begin{aligned} &F_y \frac{s^2}{\alpha} e^{-\alpha|z-z_*|} \\ &+ F_y \frac{k^2 - \beta^2}{\beta} e^{-\beta|z-z_*|} \end{aligned} \right] J_0(sr) s ds \\
\sigma_{zz}^m(r, z) &= \frac{e^{i\omega t}}{4\pi\rho\omega^2} \mu \int_0^\infty \left[\begin{aligned} &-F_y \frac{s}{\alpha} (k^2 - 2s^2) e^{-\alpha|z-z_*|} \\ &-2F_y \beta s e^{-\beta|z-z_*|} \end{aligned} \right] J_1(sr) s ds \\
\sigma_{rz}^m(r, z) + \sigma_{\theta z}^m(r, z) &= \frac{e^{i\omega t}}{4\pi\rho\omega^2} \mu \int_0^\infty \left[\begin{aligned} &2F_y s^2 \zeta e^{-\alpha|z-z_*|} \\ &-2F_y s^2 \zeta e^{-\beta|z-z_*|} \end{aligned} \right] J_2(sr) s ds \\
\sigma_{rz}^m(r, z) - \sigma_{\theta z}^m(r, z) &= \frac{e^{i\omega t}}{4\pi\rho\omega^2} \mu \int_0^\infty \left[\begin{aligned} &-2F_y \zeta s^2 e^{-\alpha|z-z_*|} \\ &+ 2F_y \zeta \beta^2 e^{-\beta|z-z_*|} \end{aligned} \right] J_0(sr) s ds
\end{aligned}$$

A.2 Dip-slip

Potentials

The potentials following the definition in Eq A.2

$$\begin{aligned}
 \phi &= \frac{M_0}{4\pi\rho\omega^2} e^{i\omega t} \int_0^\infty \begin{bmatrix} -0.5 \sin 2\delta (2\alpha^2 + s^2) J_0(sr) \\ -2 \cos 2\delta \zeta s \alpha \sin \theta J_1(sr) \\ -0.5 \sin 2\delta s^2 \cos 2\theta J_2(sr) \end{bmatrix} e^{-\alpha|z-z_*|} \frac{s}{\alpha} ds \\
 \Lambda &= \frac{M_0}{4\pi\rho\omega^2} e^{i\omega t} \int_0^\infty \begin{bmatrix} -1.5 \sin 2\delta \zeta \beta J_0(sr) \\ -\cos 2\delta \frac{2s^2-k^2}{s} \sin \theta J_1(sr) \\ -0.5 \sin 2\delta \zeta \beta \cos 2\theta J_2(sr) \end{bmatrix} e^{-\beta|z-z_*|} \frac{s}{\beta} ds \\
 \psi &= \frac{M_0}{4\pi\rho\omega^2} e^{i\omega t} \int_0^\infty \begin{bmatrix} +\cos 2\delta \zeta \frac{k^2\beta}{s} \cos \theta J_1(sr) \\ -0.5 \sin 2\delta k^2 \sin 2\theta J_2(sr) \end{bmatrix} e^{-\beta|z-z_*|} \frac{s}{\beta} ds
 \end{aligned}$$

Displacements and stresses

For zeroth order,

$$\begin{aligned}
 w^m &= \frac{e^{i\omega t}}{4\pi\rho\omega^2} M_0 \int_0^\infty \begin{bmatrix} 0.5 \sin 2\delta (2\alpha^2 + s^2) \zeta e^{-\alpha|z-z_*|} \\ -1.5 \sin 2\delta \zeta s^2 e^{-\beta|z-z_*|} \end{bmatrix} J_0(sr) s ds \\
 u^m + v^m &= \frac{e^{i\omega t}}{4\pi\rho\omega^2} M_0 \int_0^\infty \begin{bmatrix} 0.5 \sin 2\delta (2\alpha^2 + s^2) \frac{s}{\alpha} e^{-\alpha|z-z_*|} \\ -1.5 \sin 2\delta \beta s e^{-\beta|z-z_*|} \end{bmatrix} J_1(sr) s ds \\
 u^m - v^m &= \frac{e^{i\omega t}}{4\pi\rho\omega^2} M_0 \int_0^\infty \begin{bmatrix} -0.5 \sin 2\delta (2\alpha^2 + s^2) \frac{s}{\alpha} e^{-\alpha|z-z_*|} \\ +1.5 \sin 2\delta \beta s e^{-\beta|z-z_*|} \end{bmatrix} J_{-1}(sr) s ds \\
 \sigma_{zz}^m &= \frac{e^{i\omega t}}{4\pi\rho\omega^2} M_0 \mu \int_0^\infty \begin{bmatrix} -0.5 \sin 2\delta (2\alpha^2 + s^2) (2s^2 - k^2) \frac{1}{\alpha} e^{-\alpha|z-z_*|} \\ +3 \sin 2\delta s^2 \beta e^{-\beta|z-z_*|} \end{bmatrix} J_0(sr) s ds \\
 \sigma_{rz}^m + \sigma_{\theta z}^m &= \frac{e^{i\omega t}}{4\pi\rho\omega^2} M_0 \mu \int_0^\infty \begin{bmatrix} -\sin 2\delta \zeta s (2\alpha^2 + s^2) e^{-\alpha|z-z_*|} \\ +1.5 \sin 2\delta s (\beta^2 + s^2) e^{-\beta|z-z_*|} \end{bmatrix} J_1(sr) s ds
 \end{aligned}$$

$$\sigma_{rz}^m - \sigma_{\theta z}^m = \frac{e^{i\omega t}}{4\pi\rho\omega^2} M_0 \mu \int_0^\infty \begin{bmatrix} \sin 2\delta s(2\alpha^2 + s^2)e^{-\alpha|z-z_*|} \\ -1.5 \sin 2\delta \zeta s(\beta^2 + s^2)e^{-\beta|z-z_*|} \end{bmatrix} J_{-1}(sr) s ds$$

For $\sin \theta$ order,

$$\begin{aligned} w^m &= \frac{e^{i\omega t}}{4\pi\rho\omega^2} M_0 \int_0^\infty \begin{bmatrix} 2 \cos 2\delta \alpha s e^{-\alpha|z-z_*|} \\ -\cos 2\delta (2s^2 - k^2) \frac{s}{\beta} e^{-\beta|z-z_*|} \end{bmatrix} J_1(sr) s ds \\ u^m + v^m &= \frac{e^{i\omega t}}{4\pi\rho\omega^2} M_0 \int_0^\infty \begin{bmatrix} 2 \cos 2\delta \zeta s^2 e^{-\alpha|z-z_*|} \\ -2 \cos 2\delta \zeta s^2 e^{-\beta|z-z_*|} \end{bmatrix} J_2(sr) s ds \\ u^m - v^m &= \frac{e^{i\omega t}}{4\pi\rho\omega^2} M_0 \int_0^\infty \begin{bmatrix} -2 \cos 2\delta \zeta s^2 e^{-\alpha|z-z_*|} \\ +2 \cos 2\delta \zeta \beta^2 e^{-\beta|z-z_*|} \end{bmatrix} J_0(sr) s ds \\ \sigma_{zz}^m &= \frac{e^{i\omega t}}{4\pi\rho\omega^2} M_0 \mu \int_0^\infty \begin{bmatrix} -2 \cos 2\delta \zeta s(s^2 + \beta^2) e^{-\alpha|z-z_*|} \\ +2 \cos 2\delta \zeta s(s^2 + \beta^2) e^{-\beta|z-z_*|} \end{bmatrix} J_1(sr) s ds \\ \sigma_{rz}^m + \sigma_{\theta z}^m &= \frac{e^{i\omega t}}{4\pi\rho\omega^2} M_0 \mu \int_0^\infty \begin{bmatrix} -4 \cos 2\delta \alpha s^2 e^{-\alpha|z-z_*|} \\ +\cos 2\delta \frac{s^2}{\beta} (3\beta^2 + s^2) e^{-\beta|z-z_*|} \end{bmatrix} J_2(sr) s ds \\ \sigma_{rz}^m - \sigma_{\theta z}^m &= \frac{e^{i\omega t}}{4\pi\rho\omega^2} M_0 \mu \int_0^\infty \begin{bmatrix} 4 \cos 2\delta \alpha s^2 e^{-\alpha|z-z_*|} \\ -\cos 2\delta (2\beta^3 + \frac{s^4}{\beta} + \beta s^2) e^{-\beta|z-z_*|} \end{bmatrix} J_0(sr) s ds \end{aligned}$$

For $\cos 2\theta$ order,

$$\begin{aligned} w^m &= \frac{e^{i\omega t}}{4\pi\rho\omega^2} M_0 \int_0^\infty \begin{bmatrix} 0.5 \sin 2\delta \zeta s^2 e^{-\alpha|z-z_*|} \\ -0.5 \sin 2\delta \zeta s^2 e^{-\beta|z-z_*|} \end{bmatrix} J_2(sr) s ds \\ u^m + v^m &= \frac{e^{i\omega t}}{4\pi\rho\omega^2} M_0 \int_0^\infty \begin{bmatrix} 0.5 \sin 2\delta \frac{s^3}{\alpha} e^{-\alpha|z-z_*|} \\ -0.5 \sin 2\delta \frac{s^3}{\beta} e^{-\beta|z-z_*|} \end{bmatrix} J_3(sr) s ds \\ u^m - v^m &= \frac{e^{i\omega t}}{4\pi\rho\omega^2} M_0 \int_0^\infty \begin{bmatrix} -0.5 \sin 2\delta \frac{s^3}{\alpha} e^{-\alpha|z-z_*|} \\ -0.5 \sin 2\delta (s^2 - 2\beta^2) \frac{s}{\beta} e^{-\beta|z-z_*|} \end{bmatrix} J_1(sr) s ds \\ \sigma_{zz}^m &= \frac{e^{i\omega t}}{4\pi\rho\omega^2} M_0 \mu \int_0^\infty \begin{bmatrix} -0.5 \sin 2\delta (s^2 + \beta^2) \frac{s^2}{\alpha} e^{-\alpha|z-z_*|} \\ +\sin 2\delta s^2 \beta e^{-\beta|z-z_*|} \end{bmatrix} J_2(sr) s ds \end{aligned}$$

$$\begin{aligned}
\sigma_{rz}^m + \sigma_{\theta z}^m &= \frac{e^{i\omega t}}{4\pi\rho\omega^2} M_0\mu \int_0^\infty \begin{bmatrix} -\sin 2\delta \zeta s^3 e^{-\alpha|z-z_*|} \\ +\sin 2\delta \zeta s^3 e^{-\beta|z-z_*|} \end{bmatrix} J_3(sr) s ds \\
\sigma_{rz}^m - \sigma_{\theta z}^m &= \frac{e^{i\omega t}}{4\pi\rho\omega^2} M_0\mu \int_0^\infty \begin{bmatrix} \sin 2\delta \zeta s^3 e^{-\alpha|z-z_*|} \\ -\sin 2\delta \zeta s\beta^2 e^{-\beta|z-z_*|} \end{bmatrix} J_1(sr) s ds
\end{aligned}$$

A.3 Strike-slip

Potentials

The potentials following the definition in Eq A.1 are

$$\begin{aligned}
\phi &= -\frac{M_0}{4\pi\rho\omega^2} e^{i\omega t} \int_0^\infty \begin{bmatrix} \sin \delta \sin 2\theta s^2 J_2(sr) \\ -2 \cos \delta \cos \theta \zeta s \alpha J_1(sr) \end{bmatrix} e^{-\alpha|z-z_*|} \frac{s}{\alpha} ds \\
\psi_r &= -\frac{M_0}{4\pi\rho\omega^2} e^{i\omega t} \int_0^\infty \begin{bmatrix} \sin \delta \sin 2\theta s J_1(sr) \\ -\cos \delta \cos \theta \zeta \beta J_0(sr) \end{bmatrix} e^{-\beta|z-z_*|} \frac{s}{\beta} ds \\
\psi_\theta &= -\frac{M_0}{4\pi\rho\omega^2} e^{i\omega t} \int_0^\infty \begin{bmatrix} \sin \delta \cos 2\theta s J_1(sr) \\ +\cos \delta \sin \theta \zeta \beta J_0(sr) \end{bmatrix} e^{-\beta|z-z_*|} \frac{s}{\beta} ds \\
\psi_z &= \frac{M_0}{4\pi\rho\omega^2} e^{i\omega t} \int_0^\infty \cos \delta \cos \theta s J_1(sr) e^{-\beta|z-z_*|} \frac{s}{\beta} ds
\end{aligned}$$

The potentials following the definition in Eq A.2

$$\begin{aligned}
\phi &= -\frac{M_0}{4\pi\rho\omega^2} e^{i\omega t} \int_0^\infty \begin{bmatrix} \sin \delta \sin 2\theta s^2 J_2(sr) \\ -2 \cos \delta \cos \theta \zeta s \alpha J_1(sr) \end{bmatrix} e^{-\alpha|z-z_*|} \frac{s}{\alpha} ds \\
\Lambda &= \frac{M_0}{4\pi\rho\omega^2} e^{i\omega t} \int_0^\infty \begin{bmatrix} \cos \delta \cos \theta s \frac{2s^2-k^2}{s} J_1(sr) \\ -\sin \delta \cos 2\theta \zeta \beta J_2(sr) \end{bmatrix} e^{-\beta|z-z_*|} \frac{s}{\beta} ds \\
\psi &= \frac{M_0}{4\pi\rho\omega^2} e^{i\omega t} \int_0^\infty \begin{bmatrix} \cos \delta \sin \theta \zeta \beta \frac{k^2}{s} J_1(sr) \\ +\sin \delta \cos 2\theta k^2 J_2(sr) \end{bmatrix} e^{-\beta|z-z_*|} \frac{s}{\beta} ds
\end{aligned}$$

Displacements and stresses

For $\cos \theta$ order,

$$\begin{aligned}
 w^m &= \frac{e^{i\omega t}}{4\pi\rho\omega^2} M_0 \int_0^\infty \left[\begin{aligned} &-2 \cos \delta \alpha s e^{-\alpha|z-z_*|} \\ &+ \cos \delta (2s^2 - k^2) \frac{s}{\beta} e^{-\beta|z-z_*|} \end{aligned} \right] J_1(sr) s ds \\
 u^m + v^m &= \frac{e^{i\omega t}}{4\pi\rho\omega^2} M_0 \int_0^\infty \left[\begin{aligned} &-2 \cos \delta \zeta s^2 e^{-\alpha|z-z_*|} \\ &+ 2 \cos \delta \zeta s^2 e^{-\beta|z-z_*|} \end{aligned} \right] J_2(sr) s ds \\
 u^m - v^m &= \frac{e^{i\omega t}}{4\pi\rho\omega^2} M_0 \int_0^\infty \left[\begin{aligned} &+ 2 \cos \delta \zeta s^2 e^{-\alpha|z-z_*|} \\ &- 2 \cos \delta \zeta \beta^2 e^{-\beta|z-z_*|} \end{aligned} \right] J_0(sr) s ds \\
 \sigma_{zz}^m &= \frac{e^{i\omega t}}{4\pi\rho\omega^2} M_0 \mu \int_0^\infty \left[\begin{aligned} &2 \cos \delta \zeta s (2s^2 - k^2) e^{-\alpha|z-z_*|} \\ &- 2 \cos \delta \zeta s (2s^2 - k^2) e^{-\beta|z-z_*|} \end{aligned} \right] J_1(sr) s ds \\
 \sigma_{rz}^m + \sigma_{\theta z}^m &= \frac{e^{i\omega t}}{4\pi\rho\omega^2} M_0 \mu \int_0^\infty \left[\begin{aligned} &4 \cos \delta \alpha s^2 e^{-\alpha|z-z_*|} \\ &- \cos \delta \left(\frac{s^4}{\beta} + 3\beta s^2 \right) e^{-\beta|z-z_*|} \end{aligned} \right] J_2(sr) s ds \\
 \sigma_{rz}^m - \sigma_{\theta z}^m &= \frac{e^{i\omega t}}{4\pi\rho\omega^2} M_0 \mu \int_0^\infty \left[\begin{aligned} &-4 \cos \delta \alpha s^2 e^{-\alpha|z-z_*|} \\ &+ \cos \delta \left(2\beta^3 + \frac{s^4}{\beta} + \beta s^2 \right) e^{-\beta|z-z_*|} \end{aligned} \right] J_0(sr) s ds
 \end{aligned}$$

For $\sin 2\theta$ order,

$$\begin{aligned}
 w^m &= \frac{e^{i\omega t}}{4\pi\rho\omega^2} M_0 \int_0^\infty \left[\begin{aligned} &\sin \delta \zeta s^2 e^{-\alpha|z-z_*|} \\ &- \sin \delta \zeta s^2 e^{-\beta|z-z_*|} \end{aligned} \right] J_2(sr) s ds \\
 u^m + v^m &= \frac{e^{i\omega t}}{4\pi\rho\omega^2} M_0 \int_0^\infty \left[\begin{aligned} &\sin \delta \frac{s^3}{\alpha} e^{-\alpha|z-z_*|} \\ &- \sin \delta \frac{s^3}{\beta} e^{-\beta|z-z_*|} \end{aligned} \right] J_3(sr) s ds \\
 u^m - v^m &= \frac{e^{i\omega t}}{4\pi\rho\omega^2} M_0 \int_0^\infty \left[\begin{aligned} &- \sin \delta \frac{s^3}{\alpha} e^{-\alpha|z-z_*|} \\ &- \sin \delta (s^2 - 2\beta^2) \frac{s}{\beta} e^{-\beta|z-z_*|} \end{aligned} \right] J_1(sr) s ds \\
 \sigma_{zz}^m &= \frac{e^{i\omega t}}{4\pi\rho\omega^2} M_0 \mu \int_0^\infty \left[\begin{aligned} &- \sin \delta (2s^2 - k^2) \frac{s^2}{\alpha} e^{-\alpha|z-z_*|} \\ &+ 2 \sin \delta \beta s^2 e^{-\beta|z-z_*|} \end{aligned} \right] J_2(sr) s ds \\
 \sigma_{rz}^m + \sigma_{\theta z}^m &= \frac{e^{i\omega t}}{4\pi\rho\omega^2} M_0 \mu \int_0^\infty \left[\begin{aligned} &- 2 \sin \delta \zeta s^3 e^{-\alpha|z-z_*|} \\ &+ 2 \sin \delta \zeta s^3 e^{-\beta|z-z_*|} \end{aligned} \right] J_3(sr) s ds
 \end{aligned}$$

$$\sigma_{rz}^m - \sigma_{\theta z}^m = \frac{e^{i\omega t}}{4\pi\rho\omega^2} M_0 \mu \int_0^\infty \begin{bmatrix} 2 \sin \delta \zeta s^3 e^{-\alpha|z-z_o|} \\ -2 \sin \delta \zeta s \beta^2 e^{-\beta|z-z_o|} \end{bmatrix} J_1(sr) s ds$$

A.4 Tensile Crack

For the purpose of short hand, the following quantities are defined to be used in this section A.4.

$$\begin{aligned} M_1 &= M_0, & \delta_1 &= 90^\circ, \\ M_2 &= M_0, & \delta_2 &= \delta + 90^\circ, \text{ and} \\ M_3 &= \frac{\lambda+2\mu}{\lambda} M_0, & \delta_3 &= \delta, \end{aligned}$$

except that $M_1 = -M_0$ when $m = 2, \cos 2\theta$ order.

Potentials

The formulation of potential for tensile crack is

$$\begin{aligned} \phi &= \sum_{k=1}^3 \phi'_k(r, \theta, z; \delta_k, M_k) \\ \psi_r &= \sum_{k=1}^3 \psi'_{r,k}(r, \theta, z; \delta_k, M_k) \\ \psi_\theta &= \sum_{k=1}^3 \psi'_{\theta,k}(r, \theta, z; \delta_k, M_k) \\ \psi_z &= \sum_{k=1}^3 \psi'_{z,k}(r, \theta, z; \delta_k, M_k), \end{aligned}$$

where the potentials with prime (\prime), which is a single couple without moment, are

$$\phi'_k = -\frac{M_k e^{i\omega t}}{4\pi\rho\omega^2} \int_0^\infty \begin{bmatrix} \{-0.25(s^2 - 2\alpha^2) \\ +0.25 \cos 2\delta_k (s^2 + 2\alpha^2)\} J_0(sr) \\ -\sin 2\delta_k \sin \theta \zeta \alpha s J_1(sr) \\ -0.25(1 - \cos 2\delta_k) \cos 2\theta s^2 J_2(sr) \end{bmatrix} e^{-\alpha|z-z_o|} \frac{s}{\alpha} ds$$

$$\begin{aligned}
\psi'_{r,k} &= -\frac{M_k e^{i\omega t}}{4\pi\rho\omega^2} \int_0^\infty \begin{bmatrix} -0.5 \sin 2\delta_k \sin \theta \zeta \beta J_0(sr) \\ + \{0.25(1 - \cos 2\delta_k)\} \\ -0.25(1 - \cos 2\delta_k) \cos 2\theta s \} J_0(sr) \end{bmatrix} e^{-\beta|z-z_*|} \frac{s}{\beta} ds \\
\psi'_{\theta,k} &= -\frac{M_k e^{i\omega t}}{4\pi\rho\omega^2} \int_0^\infty \begin{bmatrix} -0.5 \sin 2\delta_k \cos \theta \zeta \beta J_0(sr) \\ + 0.25(1 - \cos 2\delta_k) \sin 2\theta s J_1(sr) \end{bmatrix} e^{-\beta|z-z_*|} \frac{s}{\beta} ds \\
\psi'_{z,k} &= \frac{M_k e^{i\omega t}}{4\pi\rho\omega^2} e^{i\omega t} \int_0^\infty \begin{bmatrix} 0.5(1 + \cos 2\delta_k) \zeta \beta J_0(sr) \\ -0.5 \sin 2\delta_k \sin \theta s J_1(sr) \end{bmatrix} e^{-\beta|z-z_*|} \frac{s}{\beta} ds
\end{aligned}$$

Displacements and stresses

The displacements and stresses can be expressed in the form of summation for each orders, for short hand.

$$\begin{aligned}
w^m(r, z) &= \sum_{k=1}^3 w_k^m(r, z) \\
u^m(r, z) + v^m(r, z) &= \sum_{k=1}^3 u_k^m(r, z) + v_k^m(r, z) \\
&\vdots
\end{aligned}$$

For zeroth order,

$$\begin{aligned}
w_k^m &= \frac{e^{i\omega t}}{4\pi\rho\omega^2} M_k \int_0^\infty \begin{bmatrix} \{0.25(s^2 - 2\alpha^2)\zeta \\ -0.25 \cos 2\delta_k(s^2 + 2\alpha^2)\zeta\} e^{-\alpha|z-z_*|} \\ + (0.25 + 0.75 \cos 2\delta_k) \zeta s^2 e^{-\beta|z-z_*|} \end{bmatrix} J_0(sr) s ds \\
u_k^m + v_k^m &= \frac{e^{i\omega t}}{4\pi\rho\omega^2} M_k \int_0^\infty \begin{bmatrix} \{0.25(s^2 - 2\alpha^2) \frac{s}{\alpha} \\ -0.25 \cos 2\delta_k(s^2 + 2\alpha^2) \frac{s}{\alpha}\} e^{-\alpha|z-z_*|} \\ + (0.25 + 0.75 \cos 2\delta_k) \zeta s \beta e^{-\beta|z-z_*|} \end{bmatrix} J_1(sr) s ds \\
u_k^m - v_k^m &= \frac{e^{i\omega t}}{4\pi\rho\omega^2} M_k \int_0^\infty \begin{bmatrix} \{-0.25(s^2 - 2\alpha^2) \frac{s}{\alpha} \\ -0.25 \cos 2\delta_k(s^2 + 2\alpha^2) \frac{s}{\alpha}\} e^{-\alpha|z-z_*|} \\ - (0.25 + 0.75 \cos 2\delta_k) \zeta s \beta e^{-\beta|z-z_*|} \end{bmatrix} J_{-1}(sr) s ds
\end{aligned}$$

$$\begin{aligned}
\sigma_{zz,k}^m &= \frac{e^{i\omega t}}{4\pi\rho\omega^2} M_k \mu \int_0^\infty \begin{bmatrix} -\frac{s^2+\beta^2}{\alpha} \{0.25(s^2 - 2\alpha^2) \\ -0.25 \cos 2\delta_k (s^2 + 2\alpha^2) \zeta\} e^{-\alpha|z-z_*|} \\ -(0.5 + 1.5 \cos 2\delta_k) \beta s^2 e^{-\beta|z-z_*|} \end{bmatrix} J_0(sr) s ds \\
\sigma_{rz,k}^m + \sigma_{\theta z,k}^m &= \frac{e^{i\omega t}}{4\pi\rho\omega^2} M_k \mu \int_0^\infty \begin{bmatrix} \{-0.5(s^2 - 2\alpha^2) \zeta s \\ +0.5 \cos 2\delta_k (s^2 + 2\alpha^2) \zeta s\} e^{-\alpha|z-z_*|} \\ -(0.25 + 0.75 \cos 2\delta_k) \zeta s (s^2 + \beta^2) e^{-\beta|z-z_*|} \end{bmatrix} J_1(sr) s ds \\
\sigma_{rz,k}^m - \sigma_{\theta z,k}^m &= \frac{e^{i\omega t}}{4\pi\rho\omega^2} M_k \mu \int_0^\infty \begin{bmatrix} \{0.5(s^2 - 2\alpha^2) \zeta s \\ -0.5 \cos 2\delta_k (s^2 + 2\alpha^2) \zeta s\} e^{-\alpha|z-z_*|} \\ +(0.25 + 0.75 \cos 2\delta_k) \zeta s (s^2 + \beta^2) e^{-\beta|z-z_*|} \end{bmatrix} J_{-1}(sr) s ds
\end{aligned}$$

For $\sin \theta$ order,

$$\begin{aligned}
w_k^m &= \frac{e^{i\omega t}}{4\pi\rho\omega^2} M_k \int_0^\infty \begin{bmatrix} \alpha s \sin 2\delta_k e^{-\alpha|z-z_*|} \\ -0.5 \frac{s}{\beta} (\beta^2 + s^2) e^{-\beta|z-z_*|} \end{bmatrix} J_1(sr) s ds \\
u_k^m + v_k^m &= \frac{e^{i\omega t}}{4\pi\rho\omega^2} M_k \int_0^\infty \begin{bmatrix} \zeta s^2 \sin 2\delta_k e^{-\alpha|z-z_*|} \\ -\zeta s^2 \sin 2\delta_k e^{-\beta|z-z_*|} \end{bmatrix} J_2(sr) s ds \\
u_k^m - v_k^m &= \frac{e^{i\omega t}}{4\pi\rho\omega^2} M_k \int_0^\infty \begin{bmatrix} -2 \sin 2\delta_k \zeta s^2 e^{-\alpha|z-z_*|} \\ +2 \sin 2\delta_k \zeta \beta^2 e^{-\beta|z-z_*|} \end{bmatrix} J_0(sr) s ds \\
\sigma_{zz,k}^m &= \frac{e^{i\omega t}}{4\pi\rho\omega^2} M_k \mu \int_0^\infty \begin{bmatrix} -2 \sin 2\delta_k \zeta s (s^2 + \beta^2) e^{-\alpha|z-z_*|} \\ +2 \sin 2\delta_k \zeta s (s^2 + \beta^2) e^{-\beta|z-z_*|} \end{bmatrix} J_1(sr) s ds \\
\sigma_{rz,k}^m + \sigma_{\theta z,k}^m &= \frac{e^{i\omega t}}{4\pi\rho\omega^2} M_k \mu \int_0^\infty \begin{bmatrix} -2 \sin 2\delta_k \alpha s^2 e^{-\alpha|z-z_*|} \\ +0.5 \sin 2\delta_k \frac{s^2}{\beta} (3\beta^2 + s^2) e^{-\beta|z-z_*|} \end{bmatrix} J_2(sr) s ds \\
\sigma_{rz,k}^m - \sigma_{\theta z,k}^m &= \frac{e^{i\omega t}}{4\pi\rho\omega^2} M_k \mu \int_0^\infty \begin{bmatrix} 2 \sin 2\delta_k \alpha s^2 e^{-\alpha|z-z_*|} \\ -\sin 2\delta_k (\beta^3 + 0.5 \frac{s^4}{\beta} + 0.5 \beta s^2) e^{-\beta|z-z_*|} \end{bmatrix} J_0(sr) s ds
\end{aligned}$$

For $\cos 2\theta$ order,

$$w_k^m = \frac{e^{i\omega t}}{4\pi\rho\omega^2} M_k \int_0^\infty \begin{bmatrix} 0.25 \zeta s^2 e^{-\alpha|z-z_*|} \\ -0.25 \zeta s^2 e^{-\beta|z-z_*|} \end{bmatrix} (1 - \cos 2\delta_k) J_2(sr) s ds$$

$$\begin{aligned}
u_k^m + v_k^m &= \frac{e^{i\omega t}}{4\pi\rho\omega^2} M_k \int_0^\infty \begin{bmatrix} 0.25 \frac{s^3}{\alpha} e^{-\alpha|z-z_*|} \\ -0.25 \frac{s^3}{\beta} e^{-\beta|z-z_*|} \end{bmatrix} (1 - \cos 2\delta_k) J_3(sr) s ds \\
u_k^m - v_k^m &= \frac{e^{i\omega t}}{4\pi\rho\omega^2} M_k \int_0^\infty \begin{bmatrix} -0.25 \frac{s^3}{\alpha} e^{-\alpha|z-z_*|} \\ -0.25 (s^2 - 2\beta^2) \frac{s}{\beta} e^{-\beta|z-z_*|} \end{bmatrix} (1 - \cos 2\delta_k) J_1(sr) s ds \\
\sigma_{zz,k}^m &= \frac{e^{i\omega t}}{4\pi\rho\omega^2} M_k \mu \int_0^\infty \begin{bmatrix} -0.25 (s^2 + \beta^2) \frac{s^2}{\alpha} e^{-\alpha|z-z_*|} \\ +0.5 s^2 \beta e^{-\beta|z-z_*|} \end{bmatrix} (1 - \cos 2\delta_k) J_2(sr) s ds \\
\sigma_{rz,k}^m + \sigma_{\theta z,k}^m &= \frac{e^{i\omega t}}{4\pi\rho\omega^2} M_k \mu \int_0^\infty \begin{bmatrix} -0.5 \zeta s^3 e^{-\alpha|z-z_*|} \\ +0.5 \zeta s^3 e^{-\beta|z-z_*|} \end{bmatrix} (1 - \cos 2\delta_k) J_3(sr) s ds \\
\sigma_{rz,k}^m - \sigma_{\theta z,k}^m &= \frac{e^{i\omega t}}{4\pi\rho\omega^2} M_k \mu \int_0^\infty \begin{bmatrix} 0.5 \zeta s^3 e^{-\alpha|z-z_*|} \\ -0.5 \zeta s \beta^2 e^{-\beta|z-z_*|} \end{bmatrix} J_1(sr) s ds
\end{aligned}$$

A.5 Explosive Source

Potentials

$$\begin{aligned}
\phi &= \frac{M_0 e^{i\omega t}}{4\pi\rho\omega^2} \int_0^\infty \alpha h^2 e^{-\alpha|z-z_*|} \frac{s}{\alpha} ds \\
\Lambda &= 0 \\
\psi &= 0
\end{aligned}$$

Displacements and stresses

Since the explosive source is omnidirectional, there exists only zeroth Fourier order.

$$\begin{aligned}
w^m &= \frac{M_0 e^{i\omega t}}{4\pi\rho\omega^2} \int_0^\infty \zeta h^2 J_0(sr) s ds \\
u^m + v^m &= \frac{M_0 e^{i\omega t}}{4\pi\rho\omega^2} \int_0^\infty h^2 \frac{s}{\alpha} J_1(s) s ds
\end{aligned}$$

$$\begin{aligned}
u^m - v^m &= -\frac{M_0 e^{i\omega t}}{4\pi\rho\omega^2} \int_0^\infty h^2 \frac{s}{\alpha} J_{-1}(sr) s ds \\
\sigma_{zz}^m &= \frac{M_0 e^{i\omega t}}{4\pi\rho\omega^2} \mu \int_0^\infty h^2 (2s^2 - k^2) J_0(sr) s ds \\
\sigma_{rz}^m + \sigma_{\theta z}^m &= \frac{M_0 e^{i\omega t}}{4\pi\rho\omega^2} \mu \int_0^\infty 2sh^2 \zeta J_1(sr) s ds \\
\sigma_{rz}^m - \sigma_{\theta z}^m &= -\frac{M_0 e^{i\omega t}}{4\pi\rho\omega^2} \mu \int_0^\infty 2sh^2 \zeta J_{-1}(sr) s ds
\end{aligned}$$

It is noted that the seismic moment M_0 has been used for source strength of explosive source in a solid medium. However, the quantity, $\frac{M_0 h^2}{\rho\omega^2}$, can be readily converted into the volume displacement using the relation $h^2 = \frac{\rho\omega^2}{\lambda+2\mu}$, which is widely used in the acoustics community.

Bibliography

- [1] K. Aki and P. Richards. *Quantitative Seismology*. W. H. Freeman and Co., San Francisco, 1980.
- [2] W.L. Anderson. Computation of green's tensor integrals for three-dimensional electromagnetic problems using fast hankel transforms. *Geophysics*, 49:1754 – 1759, 1984.
- [3] George E. Backus. Long-wave elastic anisotropy produced by horizontal layering. *Journal of Geophysical Research*, 67, No.11:4427–4440, 1962.
- [4] Ari Ben-Menahem and Sarva Jit Singh Singh. *Seismic Waves and Sources*. Springer-Verlag New York Inc., 1981.
- [5] R. Burridge and L. Knopoff. Body force equivalents for seismic dislocations. *Bull. Seism. Soc. Amer.*, 54:1901 – 1914, 1964.
- [6] C. H. Chapman. A new method for computing synthetic seismograms. *Geophys. J. R. astr. Soc.*, 54:481 – 518, 1978.
- [7] C. H. Chapman and R. Drummond. Body-wave seismograms in inhomogeneous media using maslov asymptotic theory. *Bull. Seism. Soc. Amer.*, 72 No. 6:S277 – S317, Dec 1982.
- [8] S. D. Cooksley. *Yield and Fracture Surfaces of Brittle Solids Under Multi-axial Loading*. PhD thesis, University of Cambridge, November 1984.
- [9] Ira Dyer. Speculations on the origin of low frequency arctic ocean noise. In *Proc. Natural Mechanisms of Surface Generated Noise in the Ocean*, NATO Advanced Research Workshop, Lerici, Italy, June 1987. To be published by Plenum Press.
- [10] David M. Farmer and Yunbo Xie. The sound generated by propagation cracks in sea ice. 1988. (submitted to) *J. Acoust. Soc. Am.*

- [11] L.N. Frazer and J.F. Gettrust. On the generalization of filon's method and the computation of oscillatory integrals of seismology. *Geophys. J. R. Astr. Soc.*, 76:461–481.
- [12] F.R.DiNapoli and R.L. Deavenport. Theoretical and numerical green's function solution in a plane layered medium. *Jour. Acoust. Soc. Am.*, 67:92 – 105, 1980.
- [13] G. J. Fryer and L. N. Frazer. Seismic waves in stratified media. *Geophys. J. R. astr. Soc.*, 78:691–710, 1987.
- [14] G. J. Fryer and L. N. Frazer. Seismic waves in stratified media - ii. *Geophys. J. R. astr. Soc.*, 1987.
- [15] K. Helbig. Systematic classification of layer-induced transverse isotropy. *Geophysical Propecting*, 29:550–557, 1981.
- [16] K. Hunkins. Seismic studies of sea ice. *J. Geophys. Res.*, 65:3459–3472, 1960.
- [17] K. Kasahara. *Earthquake Mechanics*. Cambridge University Press, 1981.
- [18] R.E. Keenan and L.A. Gainey. *FRAM IV Ambient Noise : (100 Hz - 500 Hz) Data Analysis*. Technical Report SAIC-85/1901, Science Applications Inc, Nov 1985.
- [19] L. Tsang R. Brown J.A. Kong and G. Simmons. Numerical evaluation of electromagnetic fields due to dipole antennas. *Journal of Acoustical Society of America*, 78 (6):2105 – 2114, December 1985.
- [20] Th. Krey and K. Helbig. A theorem concerning anisotropy of stratified media and its significance for reflection seismics. *Geophysical Prospecting*, 4:294–302, 1956.
- [21] W. A. Kuperman and H. Schmidt. Rough surface elastic wave scattering in a horizontally stratified ocean. *Journal of Acoustical Society of America*, 79 (6):1767 – 1777, 1986.
- [22] A. J. Langley. Acoustic emission from the arctic ice sheet. *J. Acoust. Soc. Am.*, 85:692–701, 1989.
- [23] A. J. Langley. Exact and approximate theories for fluid-loaded, infinite, elastic plates. *J. Acoust. Soc. Am.*, 83:1366–1375, 1988.

- [24] A. J. Langley. The sound fields of an infinite, fluid-loaded plate excited by a point force. *J. Acoust. Soc. Am.*, 83:1360–1365, 1988.
- [25] A. E. H. Love. *A Treatise on the Mathematical Theory of Elasticity*. reprinted by Dover Publications, New York, 4th ed. edition, 1944.
- [26] B. Mandal. Computation of the complete wavefield in anisotropic media. 1988. ERL.
- [27] B. Mandal. Synthetic vertical seismic profiles in vertical transversely isotropic media. 1987. ERL, MIT, Annual Report.
- [28] B. Mandal. Teleseismic body waves in transversely isotropic media. *Geophysical Journal*, 94:427–442, 1988.
- [29] B. Mandal and B. J. Mitchell. Complete synthesis for transversely isotropic media. *J. Geophys.*, 59:149–156, 1986.
- [30] L. Mansinha. The velocity of shear fracture. *Bull. Seis. Soc. Am.*, 54:369–376, 1964.
- [31] A. R. Milne. Sound propagation and ambient noise under sea ice. In V.M. Albers, editor, *Underwater Acoustics*, Plenum Press, 1967.
- [32] John L. Nabelek. *Determination of earthquake source parameters from inversion of body waves*. PhD thesis, Massachusetts Institute of Technology, January 1984.
- [33] N.C.Makris and I. Dyer. Environmental correlates of pack ice noise. *J. Acoust. Soc. Am.*, 79:1434–1440, 1986.
- [34] R. S. Pritchard. Arctic ocean background noise caused by ridging of sea ice. *J. Acoust. Soc. Am.*, 75:419–427, 1984.
- [35] J.W.S. Rayleigh. *The theory of sound*. Dover Publications, NEW YORK, 1957.
- [36] Ryosuke Sato. Formulation of solutaions for earthquake source models and some related problems. *Journal of Physics of The Earth*, 17, No. 2:101 – 110, 1969.
- [37] J. C. Savage and L. Mansinha. Radiation from a tensile fracture. *Journal of Geophysical Research*, 68, No. 23:6345 – 6358, 1963.

- [38] H. Schmidt and J. Glattetre. A fast field model for three-dimensional wave propagation in stratified environments based on the global matrix method. *Journal of Acoustical Society of America*, 78 (6):2105 – 2114, December 1985.
- [39] H. Schmidt and F. B. Jensen. A full wave solution for propagation in multilayered viscoelastic media with application to gaussian beam reflection at fluid-solid interfaces. *Journal of Acoustical Society of America*, 77 (3):813 – 825, 1985.
- [40] Henrik Schmidt. *SAFARI – User's Guide*. SACLANT ASW Research Centre, I-19100 La Spezia, Italy, May 1987.
- [41] M. Schoenberg. Reflection of elastic waves from periodically stratified media with interfacial slip. *Geophysical Prospecting*, 31:265–292, 1983.
- [42] P. J. Stein. *Acoustic monopole in a floating ice plate*. PhD thesis, Massachusetts Institute of Technology, Feb. 1986.
- [43] H. Takeuchi and M. Saito. Seismic surface waves. In Bruce A. Bolt, editor, *Methods in computational physics*, Academy Press, New York, 1972. Vol. 11.
- [44] M. Townsend-Manning. *Analysis of Central Arctic Noise Events*. Dept. of Ocean Eng. Engineer Thesis, M.I.T., June 1987.
- [45] W. S. Jardetzky W. M. Ewing and F. Press. *Elastic Waves in Layered Media*. McGraw-Hill, New York, 1957.